Optical properties of carbon based materials in high magnetic fields

Ubrig Nicolas

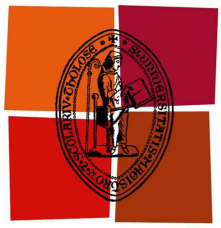

Université
de Toulouse

THÈSE

en vue de l'obtention du

DOCTORAT DE L'UNIVERSITÉ DE TOULOUSE

Délivré par l'Université Toulouse III - Paul Sabatier
Discipline : Physique

Présentée et soutenue par

Nicolas UBRIG

Le *18 Mars 2011*

Optical properties of carbon based materials in high magnetic fields

Jury

Wolfgang **Bacsa**	Professeur	CEMES-Toulouse	(*Président*)
Peter **Christianen**	Professeur	HFML-Nijmegen	(*Rapporteur*)
Vojislav **Krstić**	Chargé de recherche	CRANN-Dublin	(*Examinateur*)
Robin **Nicholas**	Professeur	Clarendon Lab.-Oxford	(*Rapporteur*)
Geert **Rikken**	Directeur de recherche	LNCMI-Toulouse	(*Directeur*)
Oliver **Portugall**	Ingénieur de recherche	LNCMI-Toulouse	(*Directeur*)

Ecole doctorale : Science de la Matière
Unité de recherche : Laboratoire National des Champs Magnétiques Intenses
Directeur(s) de Thèse : Geert RIKKEN et Oliver PORTUGALL

Remerciement

Cette thèse n'aurais jamais pu être réalisée sans ceux que j'appelle *les mains invisibles de la physique*. Elles représentent toutes les personnes qui touchent de près ou de loin à une manip. Ces personnes m'ont soutenu au long de toutes ces années. L'instant est venu de les remercier.

Je commencerais par mes directeurs de thèse Oliver Portugall et Geert Rikken qui m'ont permis d'effectuer cette thèse et de leurs conseils pendant toute la durée du travail.
Je remercie les professeurs Robin Nicholas, Peter Christianen, Wolfgang Bacsa et Vojislav Krstić d'avoir accepté de participer au jury de cette thèse.

Je remercie tout le personnel du LNCMI-Toulouse et les personnes qui ont contribué à la réalisation de ce travail. Plus particulièrement je citerais Aziz Zitouni et Julien Billette avec qui j'ai eu l'honneur de partager le bureau pendant plus de deux ans. Une aide précieuse ont été les conseils et les discussions avec Jérôme Béard, Jean-Pierre Nicollin et William Knafo. J'ai aussi eu l'opportunité de profiter du talent de l'équipe de l'atelier mécanique. Je tiens également à remercier nos secrétaires Françoise Moes et Séverine Bories pour leur aide concernant toutes les tâches administratives. Un grand travail de développement a été fourni grâce à l'aide de Sylvie George et sans elle nous n'aurions pas obtenu tous ces résultats.
Je salue également mes collègues doctorants Sébastion Nanot, Marius Millot, Jean-Marie Poumirol, Pierre-Yves Solane (également pour la lecture attentive du manuscrit) et tous les autres pour le soutien, les discussions et les réponses aux diverses questions auxquels nous aurons été confronté.

Je remercie l'équipe de Marek Potemski à Grenoble pour l'accueil pendant mon séjour et le temps d'expérience, ainsi que nos collaborateurs de la Rice University à Houston prof. Junichiro Kono, prof. Mateo Pasquali, Nick Parra-Vasquez et Jonah Shaver pour leur aide et les échantillons de nanotubes de carbone. En particulier j'exprime ma gratitude envers Paulina Plochocka, pour tout ce que tu as fait pour moi.

Je souhaite remercier ma famille, mes parents en particulier qui m'ont toujours soutenu de proche et de loin.

Laetitia, j'admire ta patience et ton soutien que tu m'as apporté. Au cours de tout ce temps et pour les années qui vont venir.

Contents

Chapter 1

Introduction

The different structures and chemical bonds assumed by carbon are due to the possibility of hybridisation of its orbitals. The oldest known carbon based materials are graphite (sp^2-hybridised) and diamond (sp^3-hybridised). Their properties are quite different. Diamond is an insulator and transparent. Graphite on the other hand conducts electricity very well along its planes, and is black and opaque.
During the past decades scientists have discovered new allotropes of carbon, which are predicted to have great technological application potential [Avouris 2007]. The discovery of fullerenes or buckyballs, awarded with the Nobel Prize in chemistry in 1996 for *H.W. Kroto*, *R.F. Curl* and *R.E. Smalley*, can be considered as an important milestone of a new discipline in physics and condensed matter physics, also known as *nanotechnology*. The synthesising of the first carbon nanotubes contributed mainly to the gold rush of *nanotechnologies*.
Surprising results were brought to daylight in the past few years, like the discovery of graphene, a mono-layer of graphite. Although graphene was theoretically known since 1947 with the pioneering work of P.R. *Wallace* [Wallace 1947], the first experimental report was only brought in 2004 [Novoselov 2004a]. The predicted great application potential and the fast and cheap way to produce graphene by exfoliating it from bulk graphite let the domain explode within a few years. A few days ago this discovery was awarded with the Nobel price in physics for *André Geim* and *Konstantin Novoselov*.

The aim of the present work is to investigate the properties of these systems in high magnetic fields. In experimental physics several methods and effects can be used to characterise the properties of electrons in solids in a magnetic field, for example like Shubnikov-De Haas and De-Haas-Van-Alphen oscillations, calorimetry or Raman-spectroscopy. A broad spectrum of experiments can be combined with high magnetic fields [Motokawa 2004].
In this thesis we use absorption spectroscopy and photoluminescence. In absorption we probe the occupation and the transition between energy bands by lifting an electron from the valence into the conduction band. The same principle applies to photoluminescence experiments with the difference that we measure the relaxation of electrons from the conduction into the valence band.

We probe the optical properties of carbon based materials like nanotubes, graphene and graphite in high magnetic fields. Therefore we will first remind the basic concepts of these materials ans describe the experimental setup. The results in the present manuscript are organised as follows:

- The fourth chapter describes the properties of single walled carbon nanotube (SWNT) in magnetic fields. The first part investigates the optical properties of carbon nanotubes. The bandgap of a 1 nm radius SWNT is predicted to oscillate with period of 5325 Tesla in a magnetic field due to the Aharonov-Bohm effect [Ajiki 1993, Ajiki 1994]. Theoretical works [Ando 1997, Pedersen 2003] predicted the formation of strongly bound electron-hole pairs, so-called *excitons*. This is attributed to the enhanced Coulomb interaction due to the one dimensional character of carbon nanotubes which lowers the screening between the carriers. The first experimental evidence of the existence of excitons in carbon nanotubes is published in 2005 [Wang 2005]. However the photoluminescence quantum yield is found to be very low [O'Connell 2002, Wang 2004] and attributed to the existence of non radiative decaying exciton states (dark excitons) [Perebeinos 2004]. One of the aims of this thesis is to probe the dark and bright exciton states using high magnetic fields.

- In the second part of the chapter we investigate the dynamic alignment of carbon nanotubes in an external magnetic field. Due to an intrinsic magnetic anisotropy the tubes align parallel to an applied magnetic field when they are suspended in an aqueous solution. Reports on the magnetic alignment of biomolecules or polymers are often found in literature [Meeten 1974,Maret 1985]. Comprehensive studies of dynamic alignment of such molecules are much rarer. We investigate the dynamics of aligning nanotubes through optical methods and apply a model based on rotational diffusion to model the process.

- The next chapter is dedicated to the optical properties of graphene and graphite in high magnetic fields. In the first part we treat the case of multi-layer graphene. As the absorption in a mono-layer graphene is very weak ($\approx$ 2%) [Nair 2008], it is not possible yet to measure such a system in a pulsed magnetic field where integration times have to be very short and the size of the samples is too small. At high energy with respect to the Fermi energy, i.e. in the near-infrared spectral range, epitaxially grown multi-layer graphene is investigated which presents the advantage to have a larger absorption signal than a mono-layer graphene. The polarisation and temperature dependence has been extracted to get more information about these systems and probe the high energy limit of massless Dirac fermions.

- The second part of the chapter describes the optical properties of graphite. The recent discovery of graphene renewed the interest on graphite, which is definitively easier to handle than a mono-atomic layer. Although extensively studied using the Shubnikov-de Haas effect, de Haas-Van Alphen effect, thermopower or far-infrared optics [Soule 1964, Williamson 1965, Zhu 2010, Galt 1956], even in high magnetic fields [Yaguchi 2009], there is no report on transmission experiments up to 60 Tesla. In the last part of this work we will study graphite at these field strengths and probe temperature and polarisation dependence.

Let us close the introduction with the following consideration. In the SI system the unit for the magnetic field strength is described by H in $[Am^{-1}]$. The magnetic flux density is referred by B in the unit $[T]$ (Tesla). The materials studied in this work are only weakly para- or diamagnetic. Thus both quantities are linked in very good approximation through

$$\underline{\mathbf{H}} = \frac{1}{\mu_0}\underline{\mathbf{B}} \tag{1.1}$$

where μ_0 is the vacuum permeability. We refer in the following to the magnetic field strength with B.

Chapter 2

The electronic properties of carbon allotropes

Contents

Carbon allotropes are known since several hundred years. However new objects joined the family in the past decades. The basic structural properties of these

materials are well established nowadays. The aim of this chapter is to remind the reader these essential properties and to introduce the electronic properties we will need in this work.
We will begin with graphene which can be considered as the base. We then look what is happening when we role the graphene sheet up (nanotubes) or when we stack the layers (graphite).

2.1 The electronic properties of graphene

2.1.1 The 2-D honeycomb lattice

The first theoretical description of the band structure of graphite is found in 1947 by *Wallace* [Wallace 1947]. He started to consider a mono-layer of graphite, i.e. graphene, which is at the moment the material we are interested in. The real space lattice of graphene with the well-known two dimensional honeycomb structure is presented in figure 2.1a. As presented in this figure the red atoms have one neighbour atom in the north and two neighbour atoms in the south. On the contrary blue atoms have one neighbour in the south and two neighbours in the north. This simple phenomenological point of view illustrates the requirement to introduce different sublattices in a honeycomb structure.
The unit vectors $\underline{\mathbf{a}}_1$ and $\underline{\mathbf{a}}_2$ are spanning the honeycomb lattice. The coordinates of the lattice vectors are given by

$$\underline{\mathbf{a}}_1 = \frac{a}{2}\left(3, \sqrt{3}\right) \qquad \underline{\mathbf{a}}_2 = \frac{a}{2}\left(3, -\sqrt{3}\right) \tag{2.1}$$

where $a = 0.142$ nm is the distance between two carbon atoms (see also equation 2.8).
Moreover if, for example, we start from a red atom, we will only come to another red atom with integer steps of the unit vectors presented in figure 2.1a. As briefly introduced above, we need two sublattices to correctly describe the motion of carriers in the honeycomb structure. The blue and red atoms in figure 2.1a are illustrating the different sublattices.
Once we have the unit vectors in real space we can construct the reciprocal lattice and its unit vectors. Furthermore the two non-equivalent Bravais sublattices result in two nonequivalent points in the reciprocal lattice and momentum space, i.e. **K**- and **K**'-points. The first Brillouin zone of graphene is drawn in figure 2.1b and the coordinates of the reciprocal lattice vectors are

$$\underline{\mathbf{b}}_1 = \frac{2\pi}{3a}\left(1, \sqrt{3}\right) \qquad \underline{\mathbf{b}}_2 = \frac{2\pi}{3a}\left(1, -\sqrt{3}\right) \tag{2.2}$$

The **K**- and **K**'-points play a fundamental role in the physics of graphene. They are often called *Dirac points*.

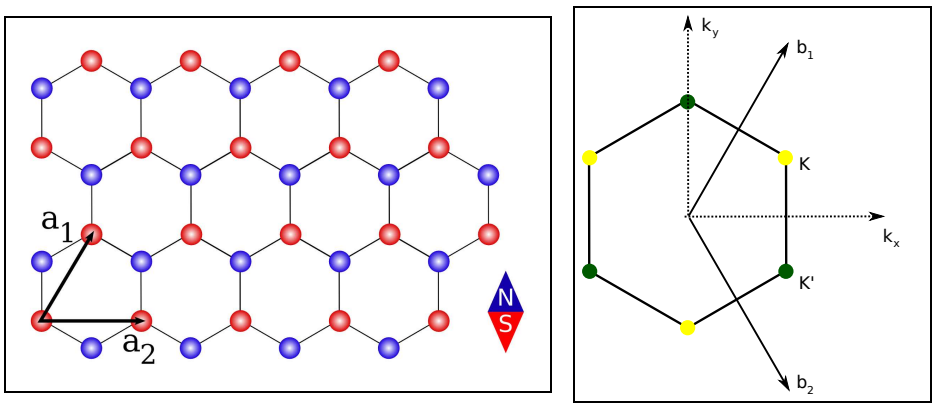

Figure 2.1 *– (a) The real space lattice of graphene and the unit vectors* $\underline{\boldsymbol{a}}_1$ *and* $\underline{\boldsymbol{a}}_2$*. The whole lattice can only be correctly described by introducing two sublattices, i.e. the red and blue atoms. (b) First Brillouin zone of graphene with the unit vectors* $\underline{\boldsymbol{b}}_1$ *and* $\underline{\boldsymbol{b}}_2$ *in momentum space. The two different honeycomb sublattices result in two nonequivalent points in momentum space* ***K****and* ***K****′.*

2.1.2 Band structure of graphene

In the *tight-binding* model which describes electronic properties of graphene one can distinguish two contributions:

- Nearest neighbour hopping (or overlap integral) γ_0, i.e. an electron hops between different sublattices and
- next-nearest neighbour hopping, t'. The electrons are moving in the same sublattice in the latter case.

Electrons in graphene do not obey the Schrödinger but the Dirac-Weyl equation which handles massless relativistic particles. For convenience we skip here the full description of Hamiltonians and the explicit solution of Schrödinger's equation. The right way would be to develop the Hamiltonians for the motion in both sublattices and solve Schrödinger's equation. One would however see that the Hamiltonian of the Schrödinger equation is in this description equivalent to the Hamiltonian of the Dirac-Weyl equation, which describes the case of massless relativistic particles [Castro Neto 2009].
The solution of the equation yields an energy dispersion written as follows

$$\begin{aligned} E_{\pm} = \pm\,\gamma_0 \sqrt{1 + 4\cos\left(\frac{\sqrt{3}k_x a}{2}\right)\,\cos\left(\frac{k_y a}{2}\right) + 4\cos^2\left(\frac{k_y a}{2}\right)} \\ - t' \cdot \left(4\cos\left(\frac{\sqrt{3}k_x a}{2}\right)\,\cos\left(\frac{k_y a}{2}\right) + 4\cos^2\left(\frac{k_y a}{2}\right)\right) \end{aligned} \tag{2.3}$$

where $+$ denotes the conduction and $-$ the valence band.

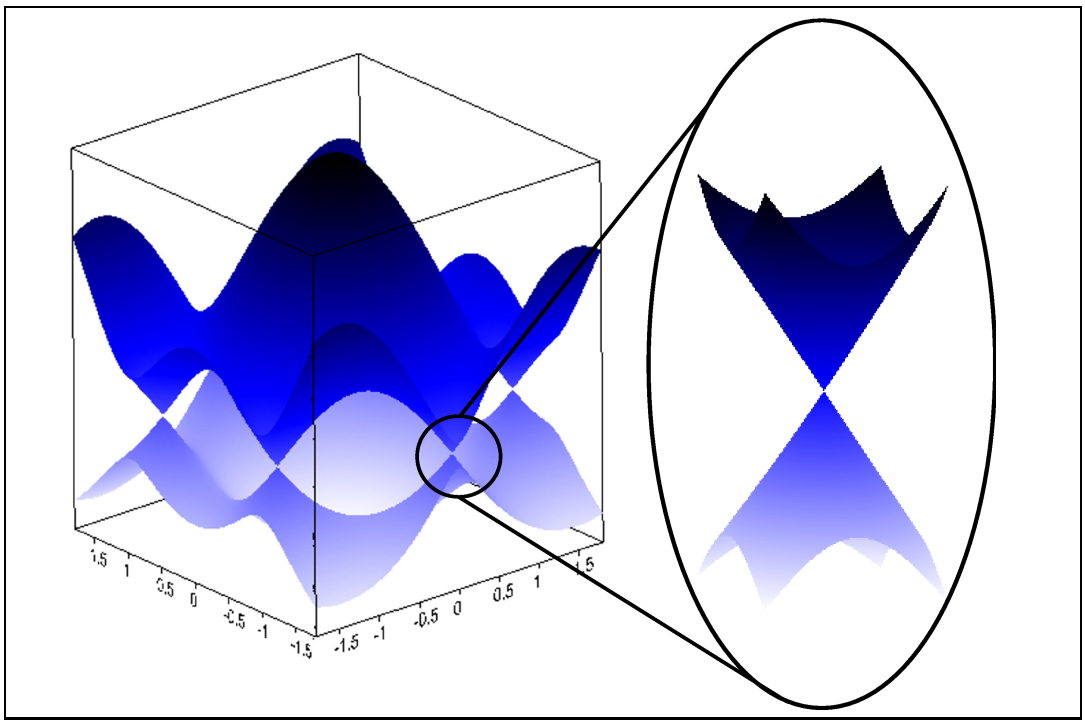

Figure 2.2 *– The three dimensional band structure of a two dimensional carbon sheet. The next-nearest neighbour term is included in this description. The zoom around the* ***K****-point shows the linear relationship between momentum and energy. The linearisation of the dispersion relation is responsible for the remarkable features observed in graphene.*

The second term in equation 2.3 is obtained by including next-nearest neighbour contributions to the Hamiltonian. However the value of t' is an actual subject of debate but is predicted to have a value distinctly smaller than γ_0 such that $t' \approx 0.1\gamma_0$.
Figure 2.2 shows the full band structure of graphene obtained from equation 2.3. We observe an asymmetry in the band structure due to contributions of next-nearest neighbour terms. It becomes evident from equation 2.3 and figure 2.2 that conduction and valence band are touching at six distinct points of the k_x, k_y-plane which exactly correspond to the **K**-points. However the most important point for the description of graphene, which leads to its particularity, is that the band structure around the **K**- and **K**'-points can be approximated by:

$$E_z = \pm\hbar v_F \left|\underline{\mathbf{k}}\right| \tag{2.4}$$

where $\underline{\mathbf{k}}$ is the momentum relatively to **K**. This relation holds for $\underline{\mathbf{k}} = \mathbf{K} + \underline{\mathbf{q}}$ with $\underline{\mathbf{q}} \ll \mathbf{K}$. v_F has the dimension of a velocity. It is the so called Fermi-velocity and can be expressed as a function of γ_0 and a such that

$$v_F = \frac{3\gamma_0 a}{2\hbar} \approx 1 \cdot 10^6 m/s \tag{2.5}$$

Such a linear dispersion relation as equation 2.4 resembles the dispersion relation for photons, i.e. massless relativistic particles. As a matter of fact, in graphene, electrons behave exactly like such particles, with a modified "light-velocity", being here the Fermi-velocity defined in equation 2.5.
Although the electronic properties of graphene were already developed in 1947 by *P.R. Wallace* [Wallace 1947], the first experimental observations have been made recently in 2004 by *K. Novoselov* and *A.K. Geim*, see e.g. [Geim 2007a] and references therein.
From the description presented above, we find that graphene exhibits spectacular and new phenomena in condensed matter physics. Using for example samples, which in general are of microscopic size, we have access to relativistic physics. A recent overview of the broad spectrum of effects in graphene is published in [Castro Neto 2009].

2.2 The electronic properties of SWNT

If we role a graphene sheet up we get a single walled carbon nanotube. The properties of these objects will be discussed in this section.

2.2.1 Basic parameters of SWNT

The basic parameters of carbon nanotubes are nowadays well described in several articles and books. If deeper information about structure or properties of carbon nanotubes beyond the scope of this work is required, we refer to reference [Saito 1998].

2.2.1.1 Classification of nanotubes

The properties of carbon nanotubes strongly depend on their shape in circumferential direction. The tubes are labelled by the integer parameters n and m which defines the circumferential vector of the nanotube. This vector is called *chiral* vector and is defined through

$$\underline{\mathbf{C}}_h = n \cdot \underline{\mathbf{a}}_1 + m \cdot \underline{\mathbf{a}}_2 \equiv (n, m) \tag{2.6}$$

where $\underline{\mathbf{a}}_1$ and $\underline{\mathbf{a}}_2$ are the unit vectors of the real space lattice of the graphene sheet, defined in equation 2.1. Together with the translational vector $\underline{\mathbf{T}}$, parallel to the tube long axis, it defines the unit cell of a SWNT as we can see in figure 2.3a. A nanotube is identified through its chiral vector and labelled (n, m). Two limiting cases exist where the symmetry of the tube is achiral. These nanotubes are called *zigzag* and *armchair* . The name arises from the shape of the cross-sectional ring of the tube. Both are illustrated in figure 2.3b. For tubes with *zigzag* symmetry, m is always equal to zero and yield a chiral vector of the form $(n, 0)$. For *armchair* symmetry, we have $n = m$ and thus the vector is written (n, n).

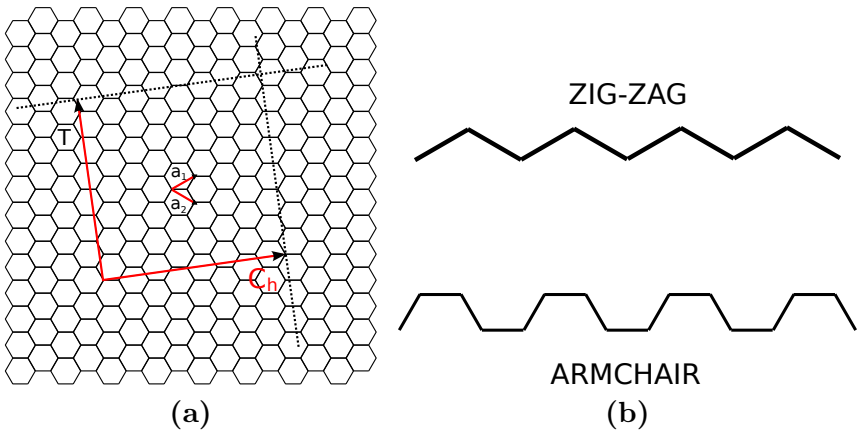

Figure 2.3 *– Nanotube unit cell and special geometries. (a) Unrolled carbon nanotube which is equivalent to a sheet of graphene. The vectors* $\underline{\mathbf{C}}_h$ *and* $\underline{\mathbf{T}}$ *define the unit cell in real space. (b) Two particular cases of circumferential geometry, zigzag and armchair .*

In this work, exclusively single walled carbon nanotubes (SWNT) are studied. But nanotubes can also exist under the form of multi-wall carbon nanotube (MWNT), which are two or more concentric SWNT.
The basic parameters which characterise a SWNT can be calculated starting from the n and m integers (see [Saito 1998] for more details). For example the diameter of a tube is written

$$d_t = \frac{a\sqrt{n^2 + m^2 + nm}}{\pi}, \tag{2.7}$$

with a being the length of the unit vector, i.e.

$$a = \sqrt{3}a_{C-C} = 2.49\mathring{A}. \tag{2.8}$$

Here $a_{C-C} = 1.44\mathring{A}$ is the bond length between two carbon atoms. Another useful example is to calculate the number of hexagons present in a unit cell

$$N = \frac{2(n^2 + m^2 + nm)}{d_R}, \tag{2.9}$$

where d_R the greatest common divisor of

$$d_R = gcd(2n + m, 2m + n). \tag{2.10}$$

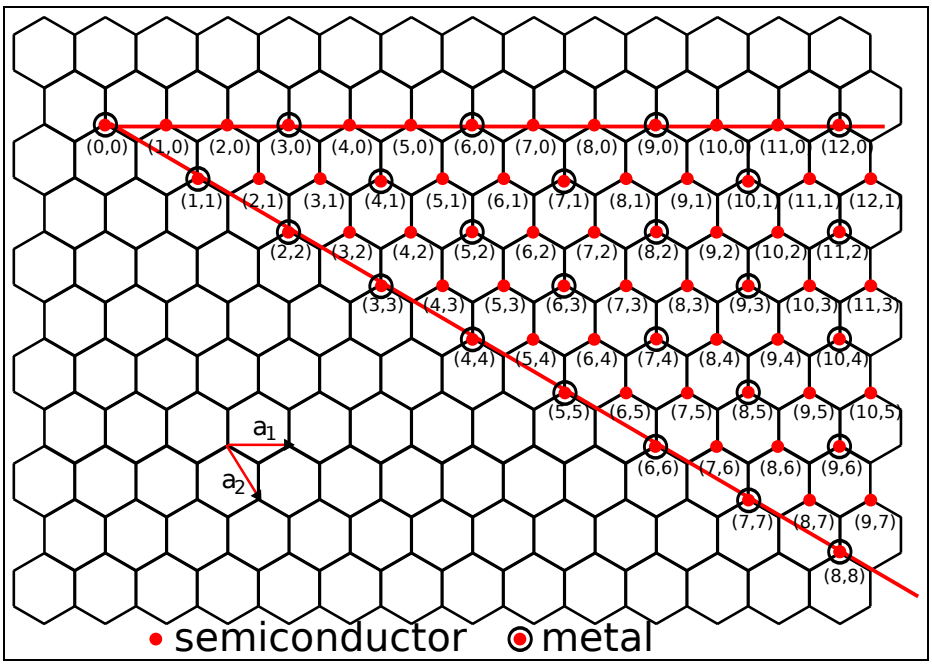

Figure 2.4 *– Map of the electronic state of SWNT as a function of the chiral vector. Armchair SWNT are always metallic. The ratio of semiconducting to metallic tubes can be visualised with help of this picture.* $\underline{\boldsymbol{a}}_1$ *and* $\underline{\boldsymbol{a}}_2$ *are the real space lattice vectors of the honeycomb structure.*

2.2.1.2 Brillouin Zone

The electronic properties of SWNT are based on those of graphene. We will start from the two dimensional honeycomb lattice and progress towards the properties of nanotubes. The unit cell of nanotubes on a sheet of graphene is presented in figure 2.3a. The unit vectors of this cell are the chiral vector $\underline{\mathbf{C}}_h$ and the translational vector $\underline{\mathbf{T}}$.
The reciprocal lattice vectors are obtained from the usual relation

$$\underline{\mathbf{R}}_i \cdot \underline{\mathbf{K}}_j = 2\pi\delta_{ij} \,, \tag{2.11}$$

where $\underline{\mathbf{R}}$ and $\underline{\mathbf{K}}$ are the real space and reciprocal lattice vectors respectively. From relation 2.11 we find

$$\underline{\mathbf{K}}_1 = \frac{1}{N}(-t_2\underline{\mathbf{b}}_1 + t_1\underline{\mathbf{b}}_2) \text{ and } \underline{\mathbf{K}}_2 = \frac{1}{N}(m\underline{\mathbf{b}}_1 - n\underline{\mathbf{b}}_2) \,, \tag{2.12}$$

with $t_1 = \frac{2m+n}{d_R}$ and $t_2 = \frac{2n+m}{d_R}$. The integers t_1 and t_2 define the translational vector $\underline{\mathbf{T}}$, i.e. $\underline{\mathbf{T}} = (t_1, t_2)$. The winding of the graphene sheet introduces a circumferential boundary condition on the electron wave function and confines the quasi-free motion to one dimension. Hence we can interpret the vector $\underline{\mathbf{K}}_1$ as a vector which plays the role of a quantisation axis and gives N discrete values in the direction of $\underline{\mathbf{C}}_h$. Thus $\underline{\mathbf{K}}_1$ is not a real reciprocal lattice vector in the strict sense of the term.

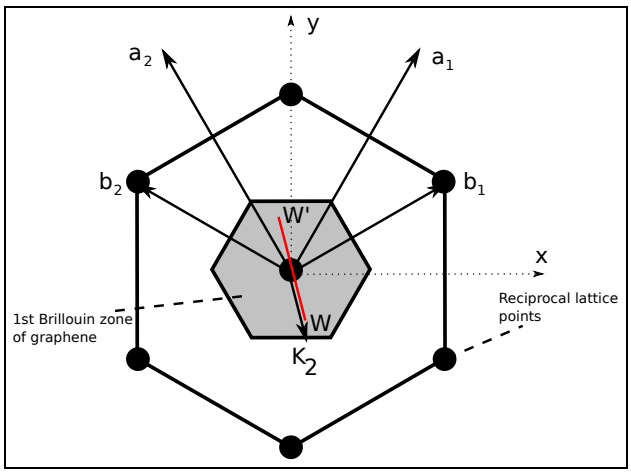

Figure 2.5 *– Important vectors of 2-D graphite and SWNT.* $\underline{\boldsymbol{a}}_1$ *and* $\underline{\boldsymbol{a}}_2$ *are the unit vectors of real space.* $\underline{\boldsymbol{b}}_1$ *and* $\underline{\boldsymbol{b}}_2$ *are the reciprocal lattice vectors of the graphene sheet. The grey area represent the Brillouin zone of 2-D graphite. The red line the* 1^{st} *Brillouin zone of SWNT delimited by* ***W*** *and* ***W'****. It is parallel to the vector* $\underline{\boldsymbol{K}}_2$*.*

In figure 2.5 we represent the Brillouin zone of graphene and nanotubes schematically. The Brillouin zone of SWNTs is one dimensional and defined by a line segment (WW' in the figure) in the $\underline{\mathbf{K}}_2$ direction. For nanotubes of infinite length the line segment is of infinite length, otherwise its length is $2\pi/\underline{\mathbf{T}}$.

2.2.2 Band structure

We differentiate two types of electronic states in carbon nanotubes, depending on chirality, i.e.

- metallic state and
- semiconducting state.

The ratio of metallic to semiconducting tubes is 1:2. This can be seen for example in figure 2.4 where the different electronic states are attributed to their specific chirality. The electronic state is obtained from the following relations

$$(n - m) \bmod 3 = 0 \tag{2.13}$$

for metallic tubes and

$$(n - m) \bmod 3 = 1 \cap 2 \tag{2.14}$$

for semiconductors.
The description of the band structure of SWNT starts with considering the two dimensional dispersion relation obtained from graphene. The electronic band structure of the two dimensional honeycomb lattice and the associate calculations have

been discussed in the previous section. Let us just remind here the result of the two dimensional dispersion relation of graphene we obtain using the tight-binding method

$$E_{2D} = \pm\gamma_0\sqrt{1 + 4\cos\left(\frac{\sqrt{3}k_x a}{2}\right)\cos\left(\frac{k_y a}{2}\right) + 4\cos^2\left(\frac{k_y a}{2}\right)}, \tag{2.15}$$

with γ_0 being the overlap integral of the bonding (π) and anti-bonding ($\pi^\star$) energy bands with

$$\gamma_0 \approx 3\,\text{eV}. \tag{2.16}$$

Note that we neglected here next-nearest-neighbour interactions for simplicity. The band structure of graphene derived from equation 2.15 is drawn in figure 2.6a. We add the first Brillouin zone of SWNT obtained from equation 2.12.
The band structure of SWNT is obtained by introducing a periodic boundary condition due to the winding of the graphene sheet. The requirement is that the wave function has to be continuous in circumferential direction, i.e.

$$\psi(\underline{\mathbf{r}}) = \psi(\underline{\mathbf{r}} + \underline{\mathbf{C}}_h). \tag{2.17}$$

Thus the 1-D dispersion relation is obtained:

$$E_\mu = E_{2D}\left(k\frac{\underline{\mathbf{K}}_2}{|\underline{\mathbf{K}}_2|} + \mu\underline{\mathbf{K}}_1\right) \text{ with } \mu = 0, \ldots, N-1 \text{ and } -\frac{\pi}{T} < k < \frac{\pi}{T}. \tag{2.18}$$

It corresponds to N pairs of dispersion relation representing each a cross-section of the Brillouin zone of SWNT, a line segment WW', with the 2-D dispersion of graphene. This case is illustrated in the figures 2.6a and 2.6b. The result are summarised by two different examples which are illustrated in figures 2.6c and 2.6d. We consider the case of a semiconducting and a metallic tube, respectively. For the *armchair* $(7,7)$ nanotube conduction and valence bands are touching at the **K**-points. The Fermi level is exactly at zero on the energy axis and thus, due to the absence of a band gap, the tube is metallic. In contrast we show in 2.6c the case of *zigzag* $(7,0)$ SWNT. The Fermi energy is between the valence and conduction band and a gap between the bands in present. Hence this tube is a semiconductor. We can additionally understand the difference between metallic and semiconducting tubes phenomenologically using figures 2.6a and 2.6b. Each time a line segment WW' (red lines) is crossing a **K**- or **K**'-point of the reciprocal honeycomb lattice the bandgap vanishes and the tube is becoming metallic, otherwise the gap is present and the tube is semiconducting.
For optical investigations in this work semiconducting tubes are of principal interest, even if reports exist on remarkable optical phenomena in metallic SWNT [Wang 2007]. Of course the band gap in semiconducting tubes is of fundamental importance for experiments and technological applications. It has been shown by

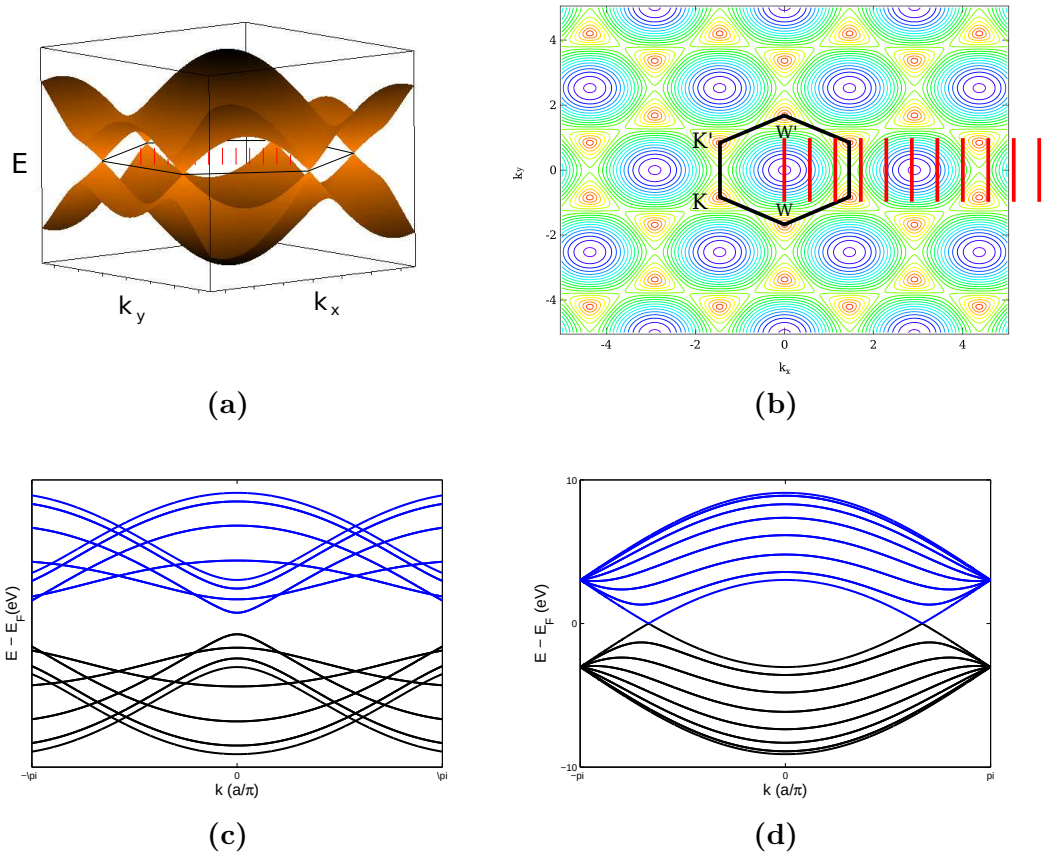

Figure 2.6 *– Example of band structures of SWNT. The band structure of graphene and the overlap of the 1-D BZ of SWNT in a schematic representation in (a) three dimensions and (b) view from the top. The result yields the figures (c) and (d). (c) Band structure of a zigzag (7,0) SWNT. This tube is supposed to be semiconducting. Indeed a gap between valence (solid black) and conduction (solid blue) band can be observed. (d) Band structure of an armchair SWNT (7,7). We expect the tube to be metallic from figure 2.4. Indeed the valence and conduction bands are touching each other, i.e. no bandgap is present.*

different experiments, such as scanning tunnelling microscopy (STM), and calculations that a simple relationship between the band gap and the tube diameter exists [Dresselhaus 1994, Wilder 1998]

$$E_g = \frac{\gamma_0 a_{C-C}}{d_t}. \tag{2.19}$$

For tubes of diameter below 14 nm the thermal energy at room temperature is smaller than the band gap E_g.

2.2.3 Density of States

In order to progress towards the optical properties of carbon nanotubes we will now consider the density of states (DoS). It has been verified theoretically and experimentally through STM experiments [Mintmire 1998, Wilder 1998].
From the electronic dispersion relation, deduced from equation 2.18, we can calculate the density of states in carbon nanotubes [Mintmire 1998]. For metallic tubes we can find a constant contribution to the DoS around the Fermi energy

$$D(E_F) = \frac{8}{\sqrt{3}\pi a \left|\gamma_0\right|} \tag{2.20}$$

with the consequence that the DoS is never zero, even in the vicinity of the Fermi energy. This is in fact the definition of a metal and presented in figure 2.7a. In contrast, as we can see in figure 2.7b, the bandgap is present in the DoS of semiconducting nanotubes. The value of the DoS around the Fermi-energy is zero.
Building the derivative, with respect to E, from the electronic dispersion relation leads to the general relation for the density of states in SWNT [Mintmire 1998]

$$D(E) \propto \frac{E}{\sqrt{E^2 - E_p^2}}. \tag{2.21}$$

E_p represents extremal values of each band of the band structure, i.e. of each band plotted in figure 2.6c and figure 2.6d. In figure 2.7 the equation above is plotted and compares the case of metallic and semiconducting tubes. We additionally observe singularities at distinct values of E_p. This behaviour is typical for a 1-D material and the singularities are called *Van-Hove singularities*. In the same time, it brings the proof of the one dimensional character of nanotubes.
Note that the shape of the DoS in carbon nanotubes strongly resembles the case when a magnetic field is applied to a three dimensional electron-gas. Due to the Landau quantisation only discrete energy states are allowed in the plane perpendicular to the axis of the magnetic field while the states parallel to this axis remain continuous. We can build an analogy here by considering the motion of an electron on the tube surface and the semi-classical trajectory of an electron in a three dimensional electron-gas in a magnetic field. In SWNT we have the condition that the wave function of carriers has to be continuous along the tube circumference. This condition acts the same way as the magnetic field on the electron gas, because electrons can take preferential orbits along the nanotube circumference. The important difference arises however, from the fact that the magnetic field forces a sense of revolution whereas for a SWNT it does not make a difference if electrons are circulating to the left or to the right. The energy levels in SWNT are therefore two-fold degenerate.

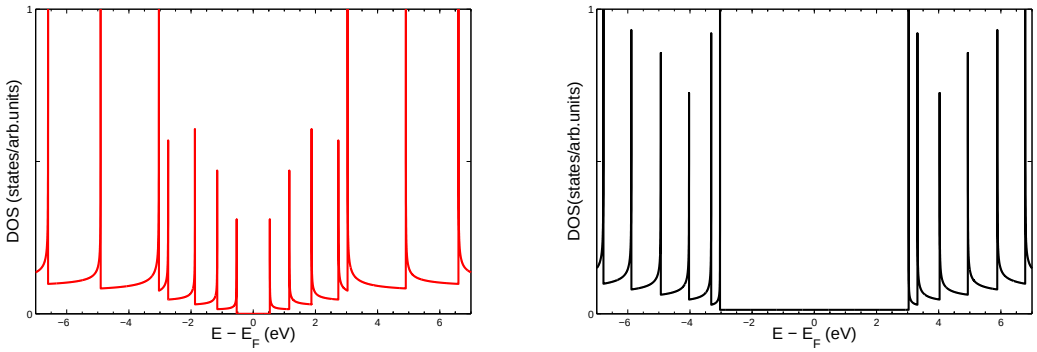

(a) **(b)**

Figure 2.7 *– The density of states for a semiconducting (a) and armchair (b) nanotube. We distinguish so-called Van-Hove Singularities which are typically observed in one dimensional materials. For semiconductors a gap is present yielding $D(E_F) = 0$ around the Fermi energy while the DoS of metals is never zero. Note the analogy between the DoS of two dimensional electron gases under magnetic field and the present DoS of SWNT.*

2.2.4 Optical selection rules

We will now focus on the optical properties of SWNT and in particular on the selection rules of light absorption and emission. A particular feature of SWNT is that they only absorb light which is polarised with an electric vector parallel to the tube long axis [Ajiki 1994]. The experimental evidence of this effect was demonstrated among others by Zaric *et al.* [Zaric 2004b]. We will make use of this fact when we study the orientation and the alignment of carbon nanotubes.
Optical interband transition are investigated theoretically [Grüneis 2003, Jiang 2004] and experimentally [Maultzsch 2005, Kataura 1999] by many groups. Dipole allowed transitions are represented in figure 2.8. Optical transitions are only possible between two Van-Hove singularities with the same sub-band number. Thus the transition between the lowest Van-Hove singularity in the conduction band and the highest singularity in the valence band is called E_{11} and so forth. We conclude from this, that the absorption is dependent on the length of the chiral vector because the DoS is different for each type of nanotube. Optical spectroscopy can thus be used to characterise nanotube samples. With the use of so-called cross polarised absorption spectroscopy, one can also observe transitions between bands with their quantum number differing by one [Miyauchi 2006].
Many optical properties are well described by these simple band-to-band transitions, in a single particle picture. However some questions, like the low photoluminescence quantum yield [Wang 2004, Lefebvre 2006] and the *ratio problem* [Bachilo 2002], can not be explained with this model. Since the screening between charge carriers decreases significantly at lower dimensionality, it was suggested that absorption of light produces strongly correlated electron and hole pairs, so-called excitons [Ando 1997].

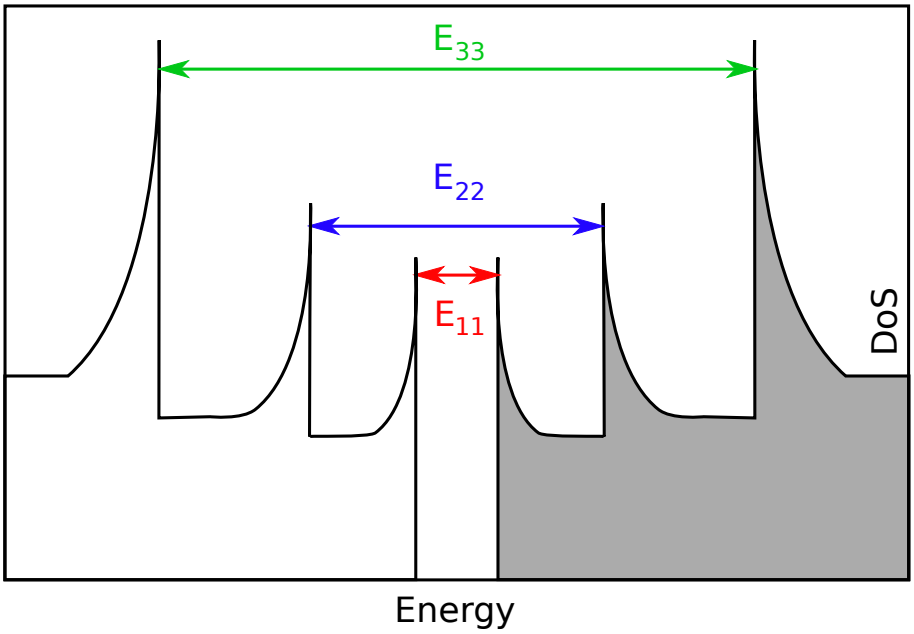

Figure 2.8 *– Dipole transitions are only allowed between sub-bands of the same number. Hence the weakest transition is denominated E_{11} and the following so forth. Dipole forbidden (e.g. E_{12}) transition can be observed by cross polarised absorption spectroscopy.*

The experimental proof of the existence of excitons in carbon nanotubes was finally obtained using of two-photon photoluminescence [Wang 2005, Maultzsch 2005]. It was shown that for a tube of ≈ 1 nm diameter the exciton binding energy is of the order of ≈ 300 meV.
In SWNT sixteen possible exciton states exist, due to electron spin and the two non equivalent **K**- and **K**'-points of the Brillouin-zone. These can be separated into four singlet states and twelve triplet states. Only one of the four singlet state remains optically active, see [Ando 1997, Spataru 2005] and references therein. We will call it a *bright* exciton. The remaining states are all optically inactive. Therefore we will call them *dark*.
These dark states can trap a considerable amount of the exciton population. Thus the low photoluminescence quantum yield of carbon nanotubes is a consequence of the non-radiative decay of these excitons [Perebeinos 2005].

2.3 The electronic properties of graphite

Graphite consists of several layers of graphene but its electronic structure is more complex than graphene. It is a semi-metal. Its layered structure is responsible for strong anisotropic behaviour, e.g. graphite is metallic along his graphene planes and insulating perpendicular to them. Slonczewski, Weiss and McClure developed a theoretical model which describes the electronic properties of graphite [McClure 1956, Slonczewski 1958]. This model is often called the Slonczewski-

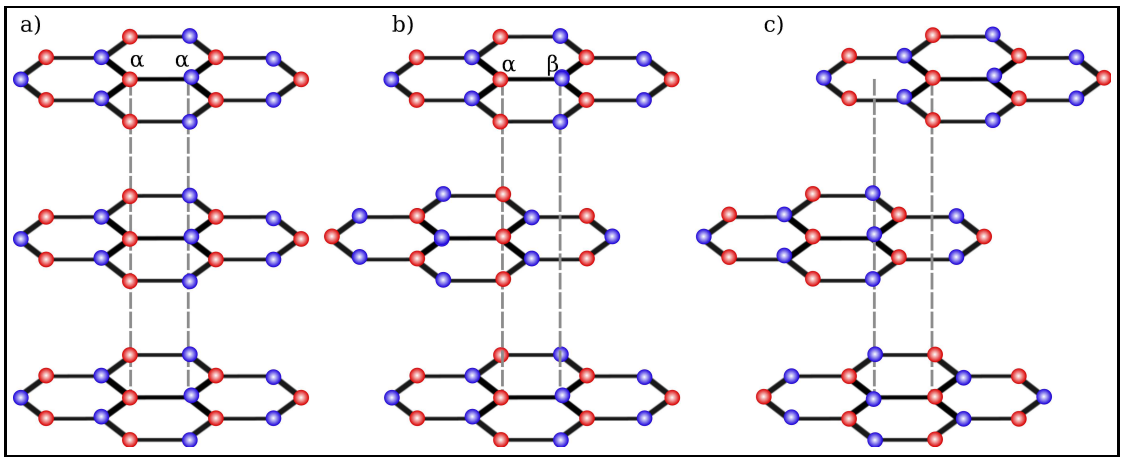

Figure 2.9 *– The different stacking forms for graphite. a) AAA- stacking; b) ABA-stacking or Bernal stacking; c) ABC-stacking. The most common form in nature is Bernal stacking on which is based the SWM model too.*

Weiss-McClure-model (SWM-model). It is based on the two dimensional description of graphite of *Wallace* [Wallace 1947] and extends its result to an infinite number of layers. The model needs several coupling parameters which describe the hopping between the π-orbitals in different layers.

2.3.1 Graphite stacking

Graphene can be stacked in different ways thus giving rise to different stacking orders which dominate the strength of the inter-layer coupling and the electronic description. Intuitively it will be clear that the form of orientation of the layers with respect to each other determines the degree of overlap of the p_z-orbitals which contain the remaining free electron of the carbon atom.
We show the different stacking forms existing in graphite in figure 2.9. The most common form encountered in nature is the ABA- or Bernal stacking ($\approx$ 85%) [Bernal 1924]. In this case the middle plane is shifted with respect to the layers above and below, such that a B-atom is between two A-atoms. Note that the SWM-model is dedicated to this stacking form. In this work we will treat graphite in Bernal stacking.
The ABC-stacking form is less frequently observed (15%). Here two successive layers are shifted such that the B-atom is on top of an A-atom.
The AAA-stacking form, is only observed in graphite intercalation compounds and does not exist in nature [Palser 1999].

2.3.2 The SWM-model

In figure 2.10a the first Brillouin zone of graphite is drawn. This is the starting point for the electronic description. It is a three dimensional hexagon. Particularly

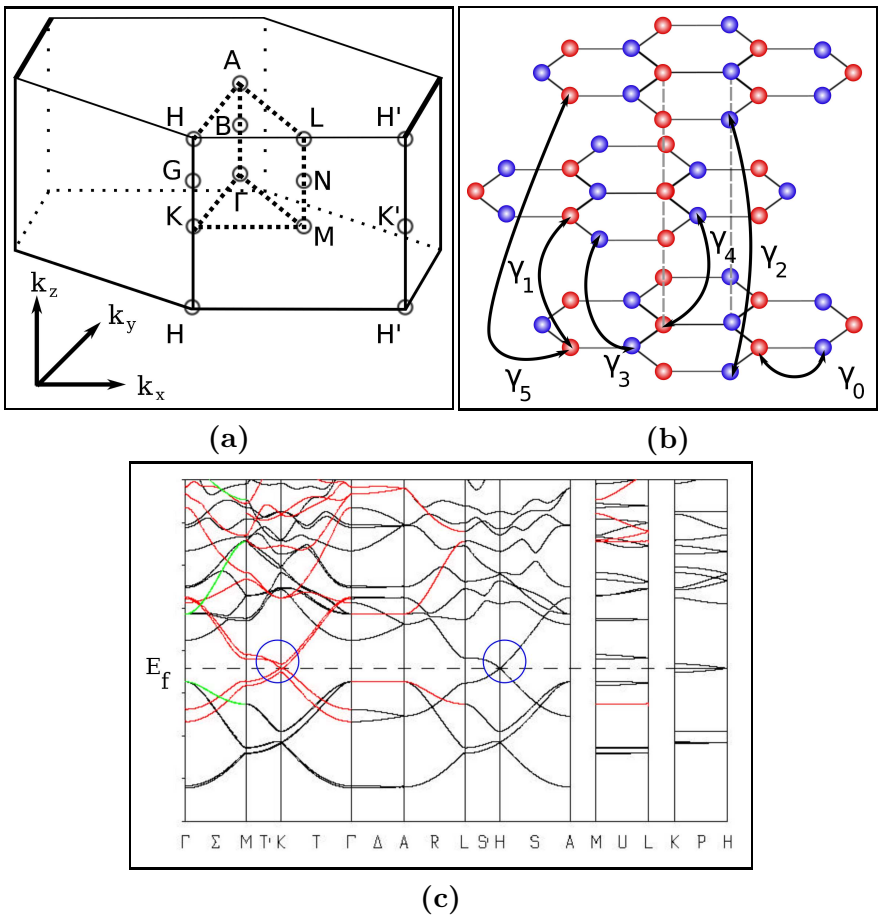

Figure 2.10 *– (a) Drawing of the three dimensional first Brillouin zone of graphite and the high symmetry points. With help of the **H–K–H**-axis we can describe the main optical and electronic properties of graphite. (b) Illustration of the hopping parameter which are used to describe the band structure of graphite. γ_0 and γ_1 are the dominant parameters of this description. However γ_3 and γ_4 can be interesting to consider because they induce trigonal warping and electron-hole asymmetry, respectively, in the band structure.(c) Complete electronic band structure of graphite obtained with DFT calculation (after Bross and Alsheimer). At the **K**-point and the **H**-point, valence and conduction band are touching at the Fermi energy. Thus graphite is a semi-metal.*

interesting are the **H**–**K**–**H**- and the **H**'–**K**'–**H**'-lines, parallel to the k_z axis and the edges of the hexagon. The dispersions along this axis is responsible for most of the electrical and optical properties of graphite.

The full SWM-model needs 6 hopping integrals $\gamma_0, \ldots, \gamma_5$ whose meanings are sketched in figure 2.10b. Additionally there is a need to introduce an on-site energy term, Δ, which describes the difference between the two different honeycomb sublattices. The parameter γ_0 was already discussed. It describes the hopping between nearest neighbours in the graphene plane, i.e. we can call it an intra-layer coupling. γ_1 stands for the coupling between nearest neighbour in different layers and can be

Table 2.1 – *Band-structure parameters of graphite after [Dresselhaus 2002].*

parameter	Effect	Strength
γ_0	Nearest-neighbour hopping	3.16 eV
γ_1	Next-nearest neighbour hopping	0.39 eV
γ_2	Next-nearest layer hopping	-0.02 eV
γ_3	Trigonal warping	0.315 eV
γ_4	electron-hole asymmetry	0.044 eV
γ_5	Next-nearest layer hopping	0.038 eV
Δ	sublattice splitting	-0.008 eV

considered as the inter-layer coupling. Together they are the dominant parameters for the description of graphite.

The parameter γ_3 couples next-nearest neighbours between two layers and is responsible for the apparition of trigonal warping. γ_4 has a similar role and connects next-nearest neighbour atoms between two layers but from different sublattices. Finally γ_2 and γ_5 describe the hopping between next-nearest layers. The values of these parameters was extensively studied and reviewed. See e.g. [Castro Neto 2009] or [Orlita 2010] and references therein. A representative set of values for the parameters of the tight-binding model is obtained by [Dresselhaus 2002] and is summarised in table 2.1.

The unit cell in Bernal stacking includes two layers and two atoms in each of them. As a matter of fact the base for the description of graphite is not graphene but bi-layer graphene. Therefore the tight-binding Hamiltonian can be written as a 4×4 matrix [Nakao 1976]

$$H = \begin{pmatrix} E_1 + \frac{\hbar^2 k^2}{2m} & 0 & -\frac{\sqrt{3}a}{2\sqrt{2}}\gamma_- k_+ & -\frac{\sqrt{3}a}{2\sqrt{2}}\gamma_- k_- \\ 0 & E_2 + \frac{\hbar^2 k^2}{2m} & \frac{\sqrt{3}a}{2\sqrt{2}}\gamma_+ k_+ & -\frac{\sqrt{3}a}{2\sqrt{2}}\gamma_+ k_- \\ -\frac{\sqrt{3}a}{2\sqrt{2}}\gamma_- k_- & \frac{\sqrt{3}a}{2\sqrt{2}}\gamma_+ k_- & E_3 + \frac{\hbar^2 k^2}{2m} & \sqrt{3}a\gamma_3 \cos\left(\frac{ck_z}{2}\right) k_+ \\ -\frac{\sqrt{3}a}{2\sqrt{2}}\gamma_- k_+ & -\frac{\sqrt{3}a}{2\sqrt{2}}\gamma_+ k_+ & \sqrt{3}a\gamma_3 \cos\left(\frac{ck_z}{2}\right) k_- & E_3 + \frac{\hbar^2 k^2}{2m} \end{pmatrix} \tag{2.22}$$

with

$$\begin{aligned} E_1 &= \Delta + 2\gamma_1 \cos\left(\frac{ck_z}{2}\right) + 2\gamma_5 \cos^2\left(\frac{ck_z}{2}\right) \\ E_2 &= \Delta - 2\gamma_1 \cos\left(\frac{ck_z}{2}\right) + 2\gamma_5 \cos^2\left(\frac{ck_z}{2}\right) \\ E_3 &= 2\gamma_2 \cos^2\left(\frac{ck_z}{2}\right) \end{aligned} \tag{2.23}$$

where

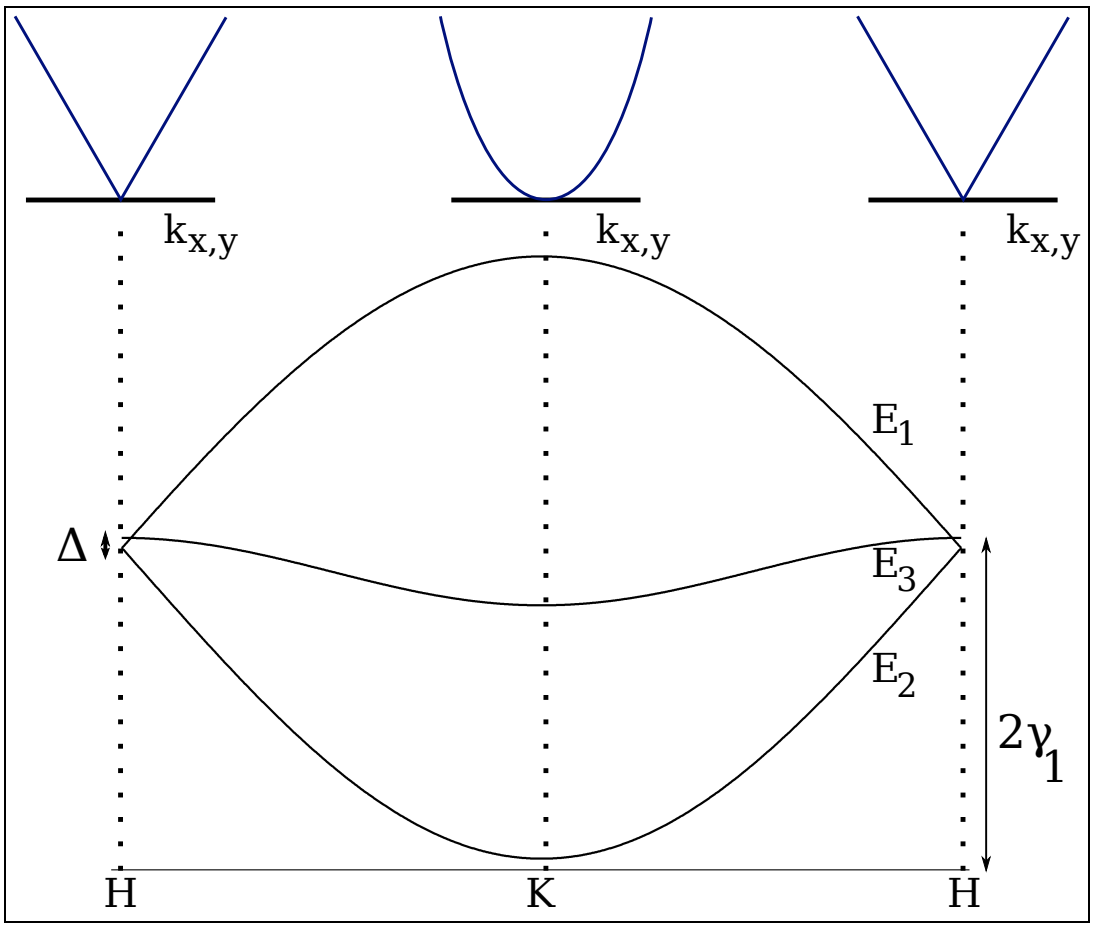

Figure 2.11 *– The band structure along the **H–K–H**-line. The dispersion of the E_1 and E_2 bands is $2\gamma_1$ at the **K**-point. Δ shifts the E_3 band with respect to E_1 and E_2 at the **H**-point. The in plane dispersions at the **K**- and **H**-points are added. Around the **H**-point we find similar dispersion as for mono-layer graphene and thus the features of massless relativistic particles. Around the **K**-point we find parabolic dispersion and similarity to bi-layer graphene. In bi-layer graphene the carriers behave like massive relativistic particles.*

$$\begin{aligned} \gamma_{\pm} &= \gamma_0 \pm 2\gamma_4 \cos\left(\frac{ck_z}{2}\right) \\ k_{\pm} &= k_x \pm ik_y \end{aligned} \tag{2.24}$$

a and c are the lattice constant in the plane and between the layers respectively. Due to the presence of several layers the electronic structure is complicated. Figure 2.10c presents the whole band structure of graphite along the high symmetry points of the Brillouin zone which illustrates the complexity of the issue.
The k_z-dependence around the **H**–**K**–**H**-line determines the optical properties of graphite. It corresponds to the orientation perpendicular to the layers. The solution of the eigenvalue problem yields the energy dispersion presented in figure 2.11. Note that the E_3 band is doubly degenerate. Without the on-site parameter Δ, the bands

would be degenerate at the **H**-point. The presence of Δ shifts the $E_{1,2}$ band as much as $\Delta = 8$ meV. In literature Δ is sometimes referred to as a pseudogap.
Let us now analyse the in plane dispersion and focus on the situation around the **K**- and **H**-point. At the **H**-point, i.e. $ck_z/2 = \frac{1}{2}$, the energy dispersion is linear. We can trace an analogy to graphene here, where we also have linear dispersion. Note the difference is that in graphene the linearisation was obtained around the **K**-point. In graphite the dispersion around the **K**-point, i.e. $k_z = 0$, is parabolic. This is the same dispersion relation we encounter when we treat bi-layer graphene. Thus the carriers around the **K**-point are expect to show bi-layer like behaviour. In contrast to graphene, where we observe massless relativistic particles, in bi-layer graphene carriers have finite mass but still different features than found in conventional systems [Geim 2007a,Castro Neto 2009], e.g. the eightfold degeneracy of the zeroth Landau level [McCann 2006a]. In graphite we thus find massless particles around the **H**-point and massive particles around the **K**-point. With these findings we expect to observe both features, mono-layer and bi-layer like transitions, while studying bulk graphite [Orlita 2009b].

2.4 Graphene in a magnetic field

Let us now apply a magnetic field and see its effects on these materials.

2.4.1 Landau levels in 2 DEG

Let us consider a two dimensional electron gas (2 DEG) in an external magnetic field. Examples of such 2 DEG are quantum wells of GaAs or CdTe. The magnetic field introduces a new fundamental length scale, the so called *magnetic length*, which represents the cyclotron orbit radius of the ground state in conventional two dimensional electron systems, and is defined through

$$l_B = \sqrt{\frac{\hbar}{eB}}\,. \tag{2.25}$$

The electronic levels are quantised by the magnetic field, the so-called *Landau quantisation*. In a system with parabolic energy dispersion the energy of the n-th orbit is given by

$$E_{2DEG}(n) = \hbar\omega_c\left(n + \frac{1}{2}\right) \tag{2.26}$$

with

$$\omega_c = \frac{e \cdot B}{m^*} = \frac{\hbar}{m^* l_B^2} \tag{2.27}$$

where n is the quantum number of the nth Landau level and ω_c the cyclotron frequency defined through e, the electronic charge, B, the magnetic field and m^*,

the effective mass of the charge carriers. The electrons are thus moving on circular orbits with the radius [Miura 2008]

$$r_c = \sqrt{2n+1} l_B \tag{2.28}$$

Note, that the system is degenerate due to the spin degree of freedom. The magnetic field lifts the spin degeneracy. The Zeeman energy is thus given by:

$$E_{Zeeman} = \mu_B g B \tag{2.29}$$

where μ_B stands for the Bohr magneton and g is the g-factor. For free electrons we have $g = 2$ and the splitting in a magnetic field is proportional to 0.116 meV per Tesla. However the g-factor in solids is generally different from two.

2.4.2 Landau levels in graphene

Let us come now to the case of graphene. Actually we would naively expect graphene to be an example case for two dimensional electron gases due to its perfect two dimensional crystal structure. But the linear relation around the **K**-points will also affect the Landau levels and the cyclotron orbits. One can express the cyclotron frequency in graphene as a function of magnetic length

$$\omega_c^g = \sqrt{2}\frac{v_F}{l_B} = v_F\sqrt{\frac{2Be}{\hbar}} \tag{2.30}$$

and hence the expression for the energy of the Landau levels [Sadowski 2007]

$$E(B,n) = \pm v_F\sqrt{2\hbar e B\,|n|} \tag{2.31}$$

These equations are obtained by introducing the magnetic field into the equation of movement by performing a *Peierl*'s substitution[1]. In graphene the Landau levels are four fold degenerate due to the two nonequivalent valleys and the two possible spin directions.
We are now able to make some remarks and pick out some differences in comparison to the conventional case of two dimensional electron gases. The first obvious and most important difference is the $\sqrt{Bn}$-dependence of the Landau levels in graphene. It is the signature of relativistic and massless particles. Another point which differs from the usual case is the fundamental Landau level ($n = 0$). In graphene the energy of this level is:

$$E(B,0) = 0. \tag{2.32}$$

which is in contrast to our findings for two dimensional electron systems with parabolic dispersion where we obtain for the fundamental Landau level ($n = 0$):

[1] The momentum $\underline{\mathbf{p}} = \hbar\underline{\mathbf{k}}$ is replaced by $\underline{\mathbf{p}} + e\underline{\mathbf{A}}$. Where $\underline{\mathbf{A}} = B/2(-y, x)$ is the vector potential of the magnetic field.

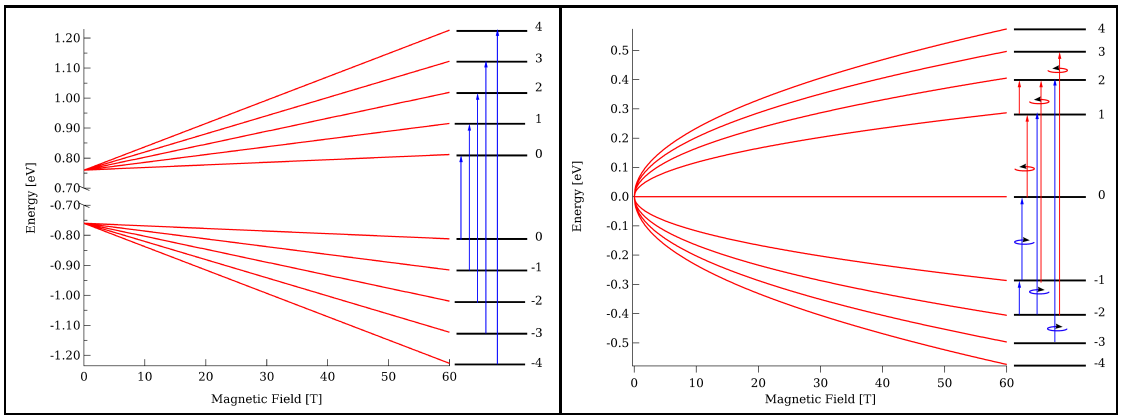

(a) **(b)**

Figure 2.12 – *(a) Linear Landau level bands for GaAs quantum well with an effective mass of $m^* = 0.067 \cdot m_e$. Note the electron ($E > 0$) and hole ($E < 0$) bands are separated by an energy gap of approximately 1.5 eV. We include optical inter-band transitions. (b) Landau levels in graphene are following the $\sqrt{B}$-dependence. On the right hand side of the figures the selection rules for Landau level transitions are sketched. The blue and red arrows should have the same strength. We can distinguish both transitions using circularly polarised light.*

$$E(B,0) = \frac{\hbar\omega_c}{2} \tag{2.33}$$

The $E = 0$ state remains an intriguing case. It is a level shared by electrons and holes simultaneously in the absence of doping [Geim 2007b].
The $n = 0$ Landau level is subject to intense debate and remains an open issue, considering for example the degeneracy breaking in high magnetic fields [Zhang 2006, Henriksen 2010]. For technological application, the presence of a bandgap would be important. In bi-layer graphene a gap opening has been observed by applying a transverse electric field to the planes [McCann 2006b]. However even under influence of a magnetic field the opening of a gap has not been observed in graphene.
In figure 2.12 we compare the Landau quantisation of a simplified band model of a GaAs quantum well and graphene. In the conventional case of a two dimensional electron gas the Landau levels scale linear in B while for graphene we find the $\sqrt{B}$-dependence, as we expect from equation 2.31. Moreover the hole and electron bands in GaAs are separated by an energy gap (approximately 1.5 eV depending on the width of the quantum well).

2.4.3 Landau level spectroscopy

In magneto-optics we do not probe Landau levels directly. But, by absorbing a photon, we can excite an electron from a filled Landau level to an empty one. We thus observe the transition energy between an initial and final Landau level state. We distinguish between two sorts of transitions:

- inter-band transitions and
- intra-band transitions

The latter case is normally observed at lower energies because the transition takes place between levels of the same band. The selection rule in Faraday configuration (see section 3.2.1) and for right/left handed circular polarisation of these transitions is

$$\Delta n = \pm 1. \tag{2.34}$$

The energy of this transition, in an ideal two dimensional electron gas, is called the cyclotron resonance and is written

$$\Delta E = \hbar\omega_c \tag{2.35}$$

These transitions are also known as the cyclotron resonance active (CRA, $\Delta n = +1$) and inactive (CRI, $\Delta n = -1$) modes.
Inter-band transitions on the other hand are lifting an electron from levels of the valence to levels of the conduction band. We consider here again the Faraday geometry. For conventional two dimensional electron gases the associated matrix element is only non-zero, i.e. the transition probability is finite, when

$$\Delta n = 0 \tag{2.36}$$

An example is presented on the right hand side of figure 2.12a for the inter-band transitions of a conventional two dimensional electron system, like GaAs quantum wells. The Landau levels, obeying equation 2.35, are equally spaced and depend linearly on the magnetic field. The spin degeneracy is neglected in this picture for simplicity.
The case is different for graphene. In figure 2.12b the Landau level structure according to equation 2.31 is plotted. In addition to this the selection rules for optically allowed transitions are sketched. Absorption from the initial state n to the final state m in Faraday geometry is only allowed when the condition [Sadowski 2006]

$$|m| = |n| \pm 1 \tag{2.37}$$

is fulfilled for light polarised circularly to the right/left handed side. We will call intra-band transition, transitions between states with the same sign, e.g. $L_{-1} \rightarrow L_{-2}$. Inter-band transition are transitions between levels with opposite sign, e.g. $L_{-1} \rightarrow L_2$. Again we can treat the zeroth Landau level as a special case, where the fundamental transitions $L_{-1} \rightarrow L_0$ and $L_0 \rightarrow L_1$ are at the same time inter-band and intra-band. Note due to the valley degeneracy the transitions from $L_{-n} \rightarrow L_{n+1}$ and $L_{-n-1} \rightarrow L_n$ are degenerate. However we can distinguish between both transitions by exciting the sample with opposite circularly polarised light as sketched in figure 2.12b.

Let us add a last remark on the Landau level transitions in graphene. The energy separation between an initial state n and final state m can be written

$$E = v_F\sqrt{2e\hbar B}\cdot\left(sgn(m)\sqrt{|m|} - sgn(n)\sqrt{|n|}\right) \tag{2.38}$$

The term $v_F\sqrt{2e\hbar B}$ corresponds exactly to the energy of the first Landau level. As we can see from equation 2.38 all optical transitions are depending on only one parameter which is the Fermi velocity v_F.

2.5 SWNT in magnetic fields

Due to the one dimensional character of SWNT the orientation of a carbon nanotube with respect to the magnetic field plays a fundamental role. When we describe the interaction between magnetic field and nanotubes we will reason in terms of magnetic flux through a section of the nanotube, Φ. The quantum of flux is given by

$$\Phi_0 = \frac{h}{e} = 4.1356\cdot 10^{-15}\ [T/m^2] \tag{2.39}$$

2.5.1 Field parallel to the tube axis

In this work we will investigate the effect of a magnetic field parallel to the tube axis. Consider first the following phenomenological argument. Due to the circumferential boundary condition, in the absence of a magnetic field, there is no difference for an electron to move right or left around the tube surface. These states are therefore degenerate. A magnetic field breaks the time reversal symmetry and the direction of the movement becomes important. However it affects only the phase of the wave function and in turn shifts the cutting lines on the graphene Brillouin zone.
A tube, with cross sectional area S, threaded by a magnetic flux, Φ, parallel to its axis will show an Aharonov-Bohm effect which strongly influences the band structure [Ajiki 1994]. The flux is defined by

$$\Phi = \int_S B\,\mathrm{d}S \tag{2.40}$$

The electrons moving on the surface of the tube experience a force due to the magnetic field parallel to the tube long axis. This does not affect the overlap integral but induces a phase shift to the wave function such that

$$\psi(\underline{\mathbf{r}} + \underline{\mathbf{C}}_h) = \psi(\underline{\mathbf{r}})e^{2\pi i(\Phi/\Phi_0)} \tag{2.41}$$

Thus the momentum in the $\underline{\mathbf{K}}_1$ direction is shifted by

$$k \to k + \frac{2\pi\Phi}{\Phi_0 L} \tag{2.42}$$

Consequently this means that the line segment **WW'** is shifted proportional to the strength of magnetic flux, i.e. $\frac{2\pi\Phi}{L\Phi_0}$. We schematically represent this effect in figure 2.13a. We saw in section 2.2.2 that a SWNT is metallic when a line segment **WW'** is crossing the **K**- or **K**'-points. Due to the Aharonov-Bohm induced shift, one of the line segments will finish by crossing (or by leaving) a **K**- or **K**'-point. Thus carbon nanotube can exhibit a semiconductor-metal transition under influence of a parallel magnetic field.
The corresponding energy gap is predicted to oscillate with a period of Φ_0. An example for a semiconducting tube is shown in figure 2.13b. This effect strongly depends on the tube diameter. To achieve a full oscillation, a tube with diameter 1 nm, 10 nm and 20 nm will need a magnetic field of 5325 T, 53 T and 13 T respectively.

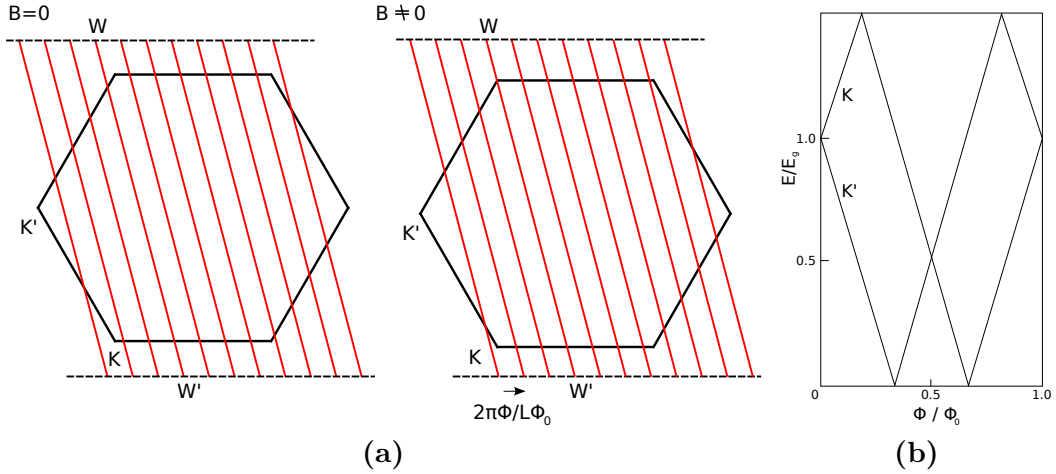

Figure 2.13 *– The Aharonov Bohm effect on the electronic band structure of SWNT. (a) When applying a magnetic field, the quantised line segments are shifted proportional to* $\frac{2\pi\Phi}{L\Phi_0}$*. When the segment is leaving or crossing a* ***K****-point the tube is undergoing a metal-semiconductor transition. (b) The oscillations of the bandgap of a semiconducting tube with the period* Φ_0*.*

2.5.2 Magnetic Susceptibility of SWNT

The susceptibility of a material can be computed from the second derivative of the free energy to the order parameter. For the magnetic susceptibility the order parameter is the magnetic field. From [Ajiki 1995] we have:

$$\chi = k_B T \frac{\partial^2}{\partial B^2} \sum_{nk} ln\left(1 + exp\left(-\frac{\varepsilon_n(k,\Phi) - \mu}{k_B T}\right)\right) \tag{2.43}$$

μ is the chemical potential and $\varepsilon(k,\Phi)$ is the electron energy depending of the magnetic field. It was found that the susceptibility ($\chi_\perp$) of semiconducting and metallic nanotubes is diamagnetic for a magnetic field perpendicular to their long axis. In

contrast the susceptibility parallel ($\chi_{\parallel}$) to the long axis is different for metallic or semiconducting tubes. Metallic tubes are paramagnetic and semiconducting tubes are diamagnetic along this axis. However, semiconducting tubes still satisfy the relation $\chi_{\parallel} > \chi_{\perp}$ [Ajiki 1995, Lu 1995] which therefore holds for SWNTs in general. The difference between the susceptibility parallel and perpendicular to the tube's long axis is written

$$\Delta\chi = \chi_{\parallel} - \chi_{\perp} > 0 \tag{2.44}$$

When suspended, e.g. in a liquid, the presence of the $\Delta\chi > 0$ induces an alignment of SWNT parallel to an external applied magnetic field irrespectively of whether they are metallic or semiconducting. However the anisotropy is predicted to be weak i.e. $\Delta\chi = 1.9 \cdot 10^{-5}$ emu/mol [Ajiki 1995]. First experimental estimations showed good agreement with the prediction [Zaric 2004b].

2.6 Graphite in a magnetic field

2.6.1 The model of *Nakao*

An extensive study and complete computation of the Landau-level structure in graphite was performed by *Nakao* [Nakao 1976]. The Landau level structure is rather complicated. The exact determination of the Landau level structure within the full SWM-model is only possible by direct numerical diagonalisation of a truncated infinite matrix [Nakao 1976]. However some simplifications can be applied. For example the effect of some SWM-parameter disappears around the **H**-point [Dresselhaus 1974, Nakao 1976, Koshino 2009]. This is the case for trigonal warping term γ_3 and due to the fact that it scales with k_z [Koshino 2009].
We saw in section 2.3.2 that the in-plane dispersion around the **K**- and **H**-point is different and equivalent to bi-layer and mono-layer graphene respectively. The Landau levels at the **H**-point are easily obtained as

$$\begin{aligned} E_1^{\pm}(n) &= \frac{1}{2}\Delta \pm \frac{1}{2}\sqrt{\frac{\Delta^2 + 3n\gamma_0^2 a_0^2 2eB}{c\hbar}} \\ E_2^{\pm}(n) &= \frac{1}{2}\Delta \pm \frac{1}{2}\sqrt{\frac{\Delta^2 + 3(n+1)\gamma_0^2 a_0^2 2eB}{c\hbar}} \end{aligned} \tag{2.45}$$

For simplicity the spin Zeeman term is neglected. We see that the Landau levels are degenerated as $E_1^{\pm}(n+1) = E_2^{\pm}(n)$, except the $n = -1$ and $n = 0$ levels [Nakao 1976]. The whole calculation shows that Landau level transitions are scaling with $\sqrt{B}$ when occurring from the **H**-point, as we can see in equation 2.45. We already saw such a dependence in mono-layer graphene.
The transitions are scaling with B when arising from the **K**-point and resemble the transitions in bi-layer graphene. The equation is not obtained as easily as in the

case of the **H**-point due to non-vanishing SWM-terms. However the cyclotron resonance and the phenomena around the **K**-point of graphite are extensively studied and show a linear B dependence [Galt 1956, Suematsu 1972, Li 2006]. Reports of observation of massless Dirac particles in graphite are much rarer. However they were also found in a work of Toy *et al.* and can be considered as the very first observation of massless Dirac fermions in solid state physics [Toy 1977].
In his paper *Nakao* found peculiar effects in the Landau level structure of graphite. While trigonal warping, described by the tight-binding parameter γ_3, plays no role at the **H**-point, in its vicinity it can however lead to magnetic breakdown producing a splitting in the Landau level structure. This effect takes place at any field strength. In contrast there is magnetic breakdown also predicted at the **K**-point but it only occurs at low magnetic fields. The magnetic energy overcomes the localisation of electron orbits in the magnetic breakdown regime and forces the electrons back to the cyclotron orbits dictated by the Landau quantisation.
At very high fields, i.e. $B > 70$ T, graphite is predicted to undergo a magnetic field induced phase transition from the semi-metallic state to a zero gap semiconductor. The $n = 0$ band of the **K**-point rises with increasing field and crosses the energy of the $n = -1$ level from the **H**-point at 70 T.

2.6.2 The effective bi-layer model

Recent infrared magneto-transmission experiments confirmed the coexistence of both, massive and massless, particles in graphite [Orlita 2008a, Orlita 2009b]. It results from these works that graphite can be treated as an assembly of weakly coupled bi-layers.
In order to assign the transitions observed in our experimental data we calculate the energy of the dipole allowed transitions ($\Delta n = \pm 1$) at the **H**- and **K**-points using a greatly simplified SWM-model with only two parameters γ_0 and $\lambda\gamma_1$ to describe the intra- and inter-layer coupling. This model is subject of actual debate and already reproduced experimental data at lower magnetic fields [Chuang 2009, Koshino 2008, Orlita 2009a, Henriksen 2008]. It is based on the model of *Nakao* but suggests many simplifications like neglecting the sublattice splitting (parameter Δ). This corresponds to treating graphite as a series of graphene bi-layers whose effective coupling depends on k_z. Here

$$\lambda = 2\cos(\pi k_z) \tag{2.46}$$

refers to the position along the k_z axis, i.e. $\lambda = 0$ is the **H**-point and $\lambda = 2$ the **K**-point. The magneto-optical response is dominated by the singularities in the joint density of initial and final states which occur at the **K**-point and **H**-point. The energy spectrum of the Landau levels using the effective bi-layer model is then given by

$$E^n_{3\pm}(k_z, B) = \pm\frac{1}{\sqrt{2}}\cdot \sqrt{(\lambda\gamma_1)^2 + (2n+1)\,\varepsilon^2 - \sqrt{(\lambda\gamma_1)^4 + 2\,(2n+1)\cdot\varepsilon^2\cdot(\lambda\gamma_1)^2 + \varepsilon^4}} \tag{2.47}$$

where we have defined

$$\varepsilon = v_F\sqrt{2e\hbar B} \tag{2.48}$$

as the characteristic magnetic energy and we find the Fermi-velocity again which we defined in equation 2.5. The sign, + and −, denotes electron and hole levels respectively. Note that at the **H**-point equation 2.47 reduces to

$$E^{n,\mathbf{H}}_{3\pm} = \pm v_F\sqrt{2e\hbar Bn} \tag{2.49}$$

and we find the expected $\sqrt{Bn}$-dependence, we already know from the Landau levels in graphene. The bi-layer model is expected to be quite accurate at the **H**-point since effects, such as trigonal warping (γ_3), vanish and analytic expressions for the Landau levels can be easily obtained within the SWM-model by diagonalising the Hamiltonian. Things are however getting a little more complicated due to the presence of the $E_{1,2}$ bands. Within the bi-layer approximation, the expression of the $E_{1,2}$-bands is very similar to equation 2.47:

$$E^n_{1,2}(k_z, B) = \pm\frac{1}{\sqrt{2}}\cdot \sqrt{(\lambda\gamma_1)^2 + (2n+1)\,\varepsilon^2 + \sqrt{(\lambda\gamma_1)^4 + 2\,(2n+1)\cdot\varepsilon^2\cdot(\lambda\gamma_1)^2 + \varepsilon^4}} \tag{2.50}$$

Around the H-point the E_1 and E_2 bands are almost degenerate with the E_3 band and only separated by the sublattice difference term Δ in the SWM-model of a few meV. But we already mentioned we are neglecting this term here. The $E_{1,2}$ bands give rise to a second Landau level spectrum with

$$E^n_{1,2} = E^{n+1}_{3\pm} \tag{2.51}$$

In figure 2.14 we show all these features where we compute the Landau level spectra between the **K**- and **H**-points using equations 2.47 and 2.50. We add the zero field dispersion of along the k_z axis of the $E_{1,2,3}$-bands for comparison. We clearly see that the $E_{1,2}$-bands are degenerated with the $E_{3\pm}$-band. However the quantum number of $E_{3\pm}$ is one higher than $E_{1,2}$ because $E_{3\pm}$-bands have a zero level which is double degenerated. These levels are often labelled $n = 0, -1$. At the **K**-point we expect from our equations to have a linear magnetic field dependence. Chuang *et al.* compared the Landau level at the **K**-point with the calculation of *Nakao* [Chuang 2009]. The levels are indeed linear with magnetic field. The main difference is seen at low fields and for the hole levels. However the bi-layer model fits the experimental data of Chuang *et al.* better than the calculation of *Nakao*.

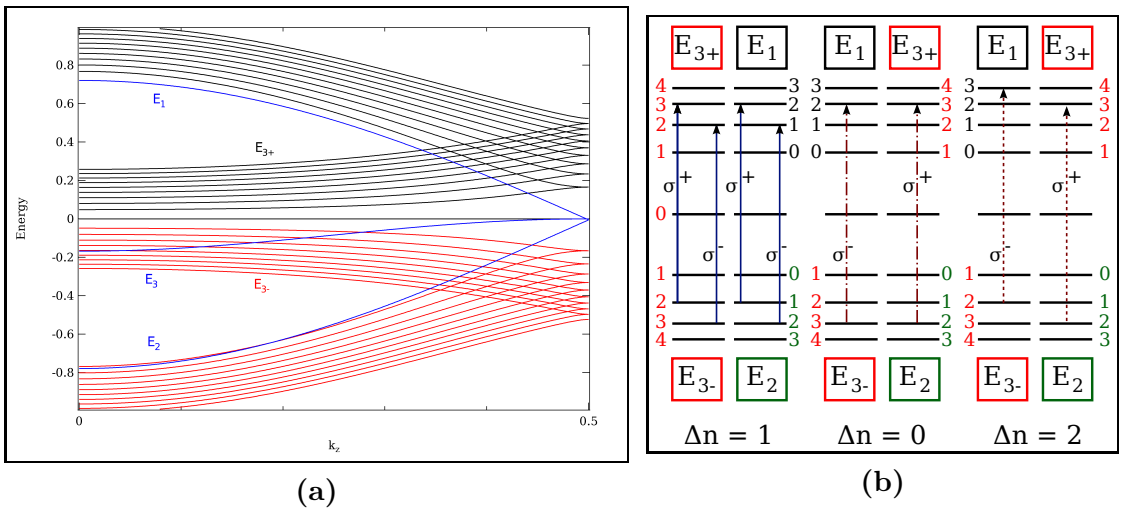

Figure 2.14 *– (a) Landau level structure graphite using the simplified SWM-model with the coupling parameter γ_0 and γ_1. The magnetic field strength is 20 Tesla. Even with a simplified model the structure is complicated. In blue the zero field E_1, E_2 and E_3 are drawn. Note that only one half of the k_z axis is displayed as the spectrum is symmetric around **K**. (b) Dipole allowed Landau level transitions at the **H**-point. Due to the complicated band structure, we find additional sets of selection rules at the **H**-point, namely $|\Delta n| = 0, 1, 2$. Circular polarised transition are also indicated where the convention $\Delta n = +1$ for σ^+ was adopted.*

Despite the use of the simplified bi-layer model, the Landau level spectrum remains complicated and so do the selection rules for transitions between Landau levels in graphite. Figure 2.14b sketches the Landau level spectrum at the **H**-point. We add all dipole allowed transitions to complete the picture. At the **H**-point we have three sorts of transitions between levels differing by their indices with apparent selection rules $|\Delta n| = 0, 1, 2$. They all correspond to dipole allowed transitions in graphite with the selection rule $\Delta n = \pm 1$. The transitions with $|\Delta n| = 1$ show great similarities with transitions we expect in graphene and can directly be compute from equation 2.49. In the figure we show an example transition between the levels $E^{2(3)} \rightarrow E^{3(2)}$. We adopt the convention for circularly polarised light by labelling $\Delta n = +1$ transition with σ^+. The two additional selection rules are illustrated too. Note that due to effects of trigonal warping an additional selection rule exists for transition between Landau levels differing by $3n \pm 1$ in their indices. But this rule applies around the **K**-point and is only observed in low fields [Suematsu 1972]. However the transitions from the **K**-point are linear with magnetic field and obey the selection rule $|\Delta n| = 1$.

Chapter 3

Experiment and setup

Contents

The aim of this chapter is to introduce the experimental techniques and setups used to obtain the results presented in the thesis. We will describe how high magnetic fields are obtained and combined with optical measurements. We will close this part with the presentation of specially designed sample holders to perform the experiments that will be described in the next chapters.

3.1 The LNCMI user-facility

The Laboratoire National des Champs Magnétiques Intenses is the French high magnetic field user facility. The most part of this work is performed at the pulsed field site in Toulouse (LNCMI-T). Some measurements were also performed at the static field facility in Grenoble (LNCMI-G).
The highest magnetic fields obtained from materials are generally not exceeding 1 Tesla, even in complex ferromagnetic compounds. To get magnetic fields higher than 2 Tesla in the laboratory, it is necessary to use electromagnets.

One technique is based on using superconducting wires which present the advantage to transport current without losses, i.e. without heating. However, superconductors have a critical current density and critical magnetic fields. This limits the fields obtained with this method to approximately 20 Tesla. Fields up to 36 Tesla can be obtained with resistive materials. The most common design is the so-called *Bitter*-coil. The maximum field of these magnets is limited by the possibility to evacuate the dissipated heat by active water-cooling. The combination of superconducting and resistive wires produces the highest static magnetic fields, e.g. about 45 Tesla at the NHMFL in Tallahassee.
Pulsed magnetic fields can overcome the limit of heating. We use the specific heat of the coil to store the heat in the coil. The aim is to stop the discharge before the magnet overheats. We call this technique pulsed magnetic field. The maximum field is limited mostly by the mechanical strength of the structure that allows it to withstand the Lorentz force. The highest field obtained with this technique is 89 Tesla on a time scale of several milliseconds.
The problem of mechanical strength can again be overcome, simply by letting the coil destroy itself. Here the discharge must be fast enough to attain the field maximum before the coil is substantially expanded. The coil explodes outwards and fields above 100 Tesla are obtainable without destroying the samples inside (semi-destructive method). Destructive methods, like flux compression and explosive flux compression, provide fields above 1000 Tesla. The price to pay is the complete destruction of the sample and parts of the setup. The limit of these techniques is the speed of discharge of the capacitors and the inductance of the generator circuit.

3.1.1 Generator

The main instrument of the LNCMI-T is the 14 MJ capacitor bank. The generator is build of ten modules with sixty capacitors each. The capacitance is 48 mF. The generator can be charged up to 24 kV. With the basic relation $E = \frac{1}{2}CU^2$ it yields a maximum energy of 14 MJ. The full circuit to produce pulsed magnetic fields corresponds essentially to a RLC-circuit and the principle is sketched in figure 3.1. The current source charges the capacitors. Once the desired charge is attained, the current is discharged in the coil. The time dependence of the current and the voltage is presented in figure 3.1b. While the energy stored in the capacitors is transferred to the coil, the current increases. The rise time of the current in a RLC-circuit with negligible R , and hence the magnetic field, is $\tau_{rise} = \frac{1}{2}\pi\sqrt{LC}$, where L is the inductance of the coil and C the capacitance of the generator.
At maximum field, the energy is completely transferred into the coil and the voltage reverses its sign. Thus the circuit is short-circuited by the crowbar diode (D_{cb} in figure 3.1b). The current decays exponentially with a time constant $\tau_{down} = L/R$, where R the resistance of the circuit. The oscillation of the RLC-circuit is thus prevented.
Different generators and pulse shapes in strength and in length are available at the LNCMI-T. They can also be combined on multiple coil systems, designed to obtain

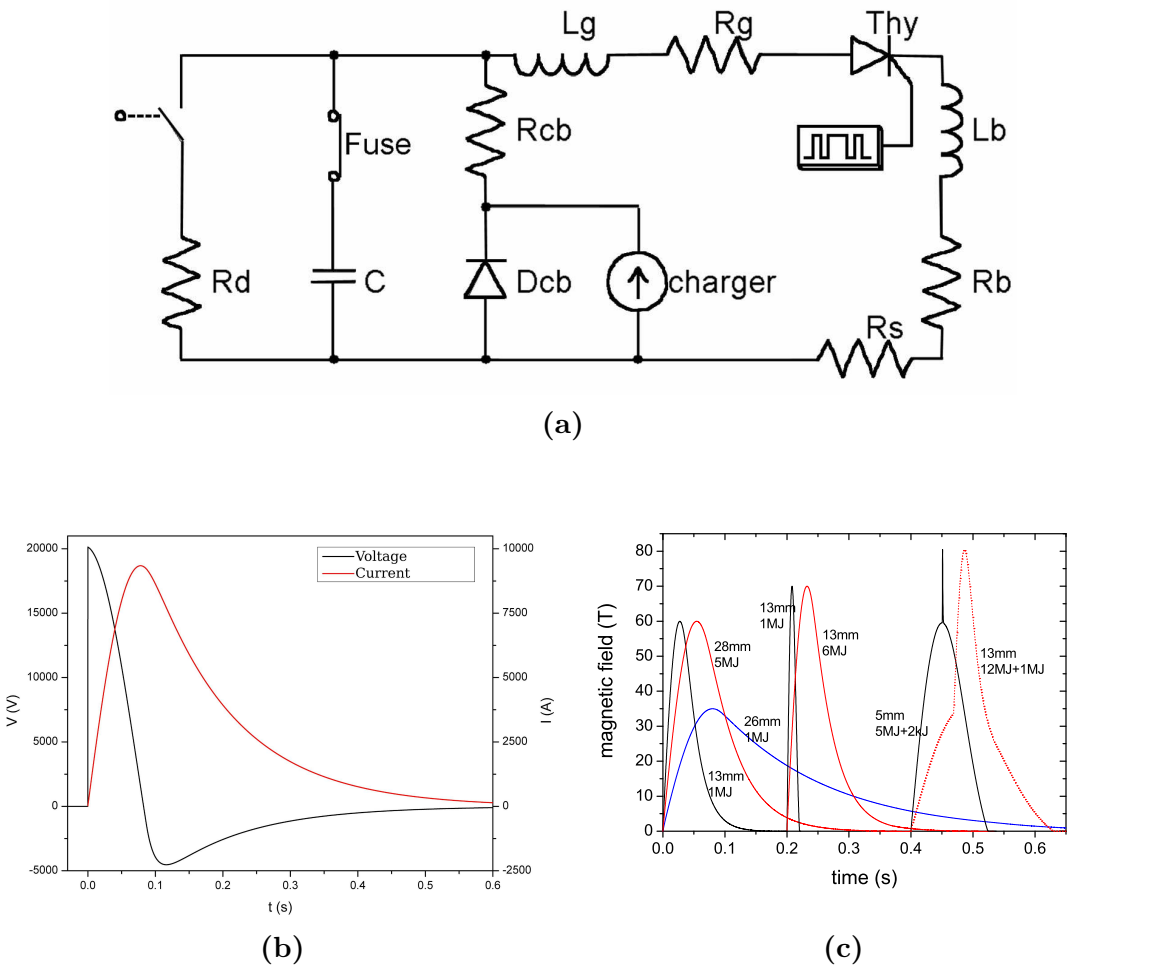

Figure 3.1 – *(a) Principle circuit of the 14MJ generator of the LNCMI-Toulouse. The magnet is represented by the inductance L_b and the resistance R_b. (b) Time dependence of the current and the voltage during a magnetic field pulse. (c) Standard pulse forms available at the LNCMI-T*

very high fields. Some actual pulse forms available at the LNCMI-T are presented in figure 3.1c. The typical time scale of the pulses is between 20 ms and 500 ms.
The polarity of the generator can be easily changed before a pulse. This enables the user to switch rapidly between two possible field directions (up and down). This is helpful for experiments with circular polarised light.
Another convenient feature of the generator is the adjustable choice of the crowbar diodes (D_{cb} and R_{cb}) which gives the possibility to vary the down sweep pulse shape.

3.1.2 Coil

The magnet, generally a home-made solenoid, is connected to the generator. The wires used to build the magnet are based on copper. To optimise pulsed magnets one has to find the equilibrium between high mechanical resistivity, to contain the

forces induced by the magnetic field, and good electrical conductivity, to avoid losses. Between the layers a *Zylon* reinforcement can be added to enhance the resistance to mechanical strain. With this configuration fields up to 60 Tesla in large bores (28 mm and 20 mm with He^4 cryostat inside) are very well controlled this way. New generations of coils are based on the wire called *Glidcop*. Fields up to 70 Tesla are achieved nowadays. The only possible way to generate higher fields, is to use a system based on the coil-in coil-ex principle [Frings 2008].
To avoid problems due to the heating of the magnet, the coils are cooled with liquid nitrogen. It presents at the same time the advantage that the resistivity is decreased, using the increased conductivity of copper, and the coil can store more heat. The use of composite materials imposes that the temperature must not exceed 350 K - 400 K. In the centre of the coil the field is sufficiently homogeneous over 1 - 1.5 cm along his long axis for our purposes.

3.1.3 Field recording

The field is measured with the help of a pick-up coil placed on the sample holder in proximity to the sample. The time dependent magnetic field induces a voltage which is proportional to

$$U_{pick-up} = N \cdot S \cdot \frac{\mathrm{d}B}{\mathrm{d}t} \tag{3.1}$$

where S is the area of one winding and N the number of windings. The induced voltage is recorded using an oscilloscope, i.e. Hioki 8855 for all experiments performed in this work. The factor $N \cdot S$ is the effective area of the pick-up coil and is calibrated independently.
The recorded signal can be integrated over the time to yield the magnetic field. In figure 3.2 an example record of the raw $\frac{\mathrm{d}B}{\mathrm{d}t}$ and the integrated signal is shown.

3.1.4 Spectrometer and acquisition

The main part of this work focuses on the optical properties of carbon based materials in the near-infrared (NIR) spectral range. The spectrometer used is equipped with an 512 pixel InGaAs array coupled to an 0.3m focal length spectrometer. The InGaAs array is cooled with liquid nitrogen. Some measurements were also performed in the visible part of the electromagnetic spectrum. In this case the setup was connected to an 1340 × 100 pixel silicon CCD array coupled to a 0.5m focal length spectrometer.
We use two experimental techniques to investigate the optical properties of our samples. The first one is absorption spectroscopy, where light is transmitted through the sample. The second technique is photoluminescence, where the light emitted by the sample is collected.
In both cases we use a function generator which creates a pulse train to trigger the spectrometer. It is thus possible to acquire with a single shot several spectra

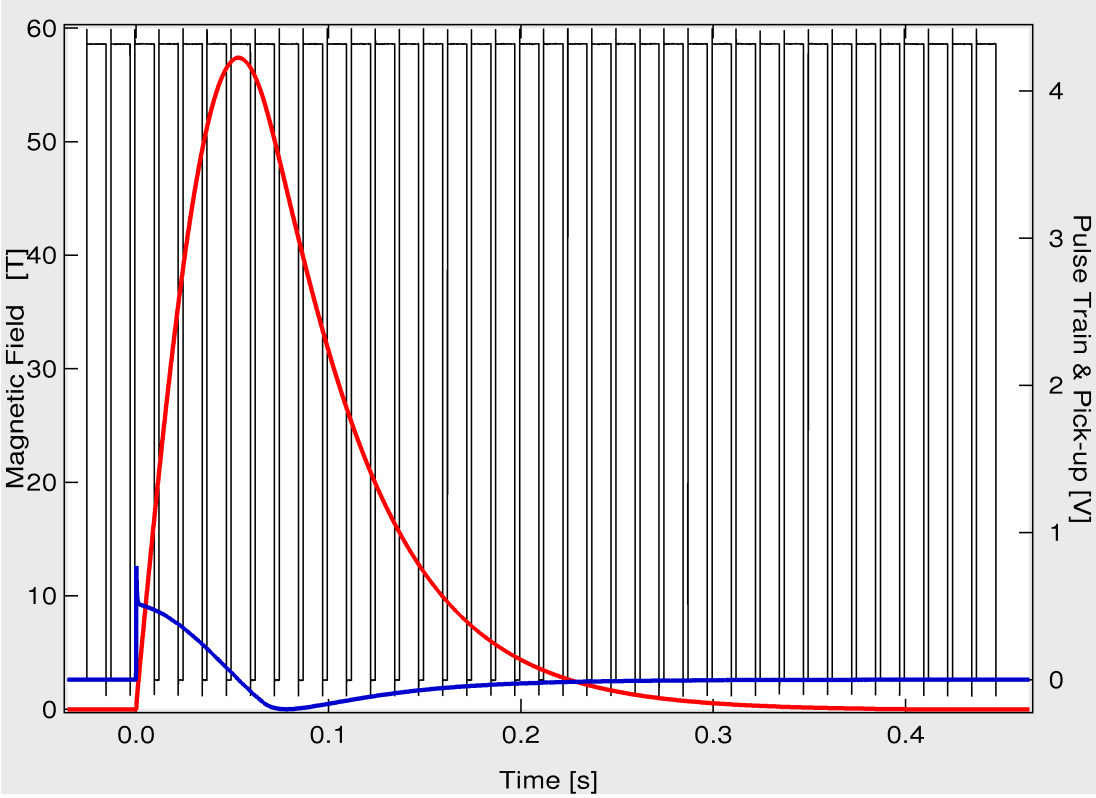

Figure 3.2 *– The field variation ($\frac{dB}{dt}$, solid blue line) as a function of time is recorded at the same time as the pulse train (thin black line) from the spectrometer. The induced pick-up voltage is integrated and displayed as the red solid line. With the acquisition of the pulse train of the spectrometer every spectra can easily be associated to its corresponding magnetic field.*

and hence the complete field dependence of the desired sample. A reference signal indicating the exposure time for each acquisition is created by the spectrometer itself and sent to the same oscilloscope with which the field is recorded. An example case was plotted in figure 3.2. Thus we are able to assign each spectrum to its corresponding magnetic field. A complete trigger-diagram and schematic view of the setup is drawn in figure 3.3. The trigger signal, coming from the thyristor switch, precedes the discharge onset by 50 ms but can also be adjusted for individual needs. We thus are able to record some reference spectra before the magnetic field pulse. A delay unit is retarding the trigger in order to place a spectrum exactly in coincidence with the maximum of the field pulse. The precision obtained with this setup is better than 0.1 ms.

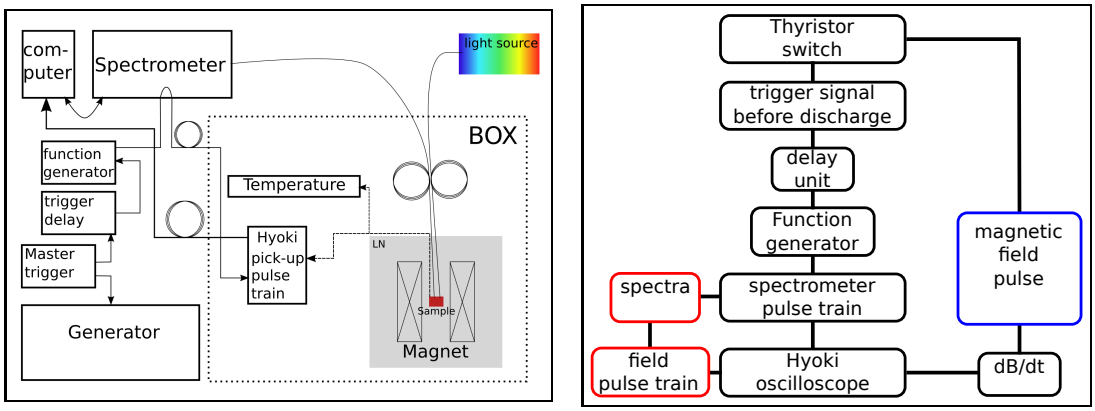

Figure 3.3 *– (a) Schematic representation of the experimental setup for magneto-spectroscopy. The optical trigger signal is given by the master trigger which closes the thyristor switches and enable the discharge. The data acquisition can be pre-triggered. Communication between the inside and the outside of the box is made with the help of optical fiber. Most experiments are working with optical fibers, i.e. spectrometer and light sources can be placed outside of the experimental box. (b) Trigger diagram of the setup. With help of the delay unit the start of the acquisition can be controlled with an accuracy better than 1 ms.*

3.2 Optical setups in magneto-optical configurations

3.2.1 Faraday configuration

In magneto-optical spectroscopy we differentiate between two geometries of orientation of the magnetic field and light. Selection rules but also the nature of the optical transition (e.g. inter-band or intra-band) can be affected by these orientations. The first one is called *Faraday* geometry. In this case the wave propagation vector of light, $\underline{\mathbf{k}}$, is parallel to the magnetic field, $\underline{\mathbf{B}}$, i.e. $\underline{\mathbf{k}} \parallel \underline{\mathbf{B}}$. The measurement principle is sketched in figure 3.4b. The main difficulty in this setups is to return the light in a bore of approximately 20 mm. The light beam has to make a U-turn at the bottom of the sample holder. At the same time there should be enough space for different kinds of samples and polarisers.
Light in the visible and near-infrared spectral range enables the use of optical fibers as a cheap and convenient method to transport light to and from the sample. The weak point of such sample holders is the ageing of fibers, in particular when they are subjected to large and abrupt temperature changes.
The design of the sample holder has to take into account the inconvenience of pulsed magnetic fields like eddy currents. The optical path has to be lossless as possible and thus distortion due to thermal expansion has to be limited in order to maintain the room temperature alignment.
The technical designs were made by Sylvie George. The parts are made by the LNCMI-T machine shop. The mounted construction is presented in figures 3.4a

and 3.4c.

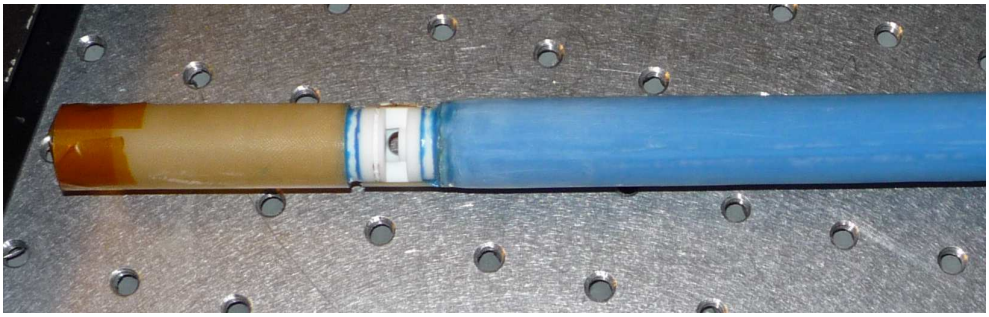

(a)

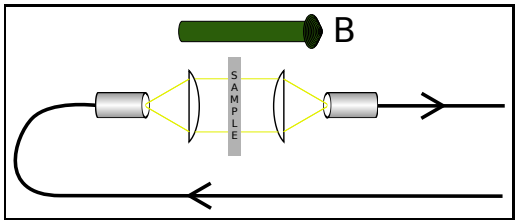

(b)

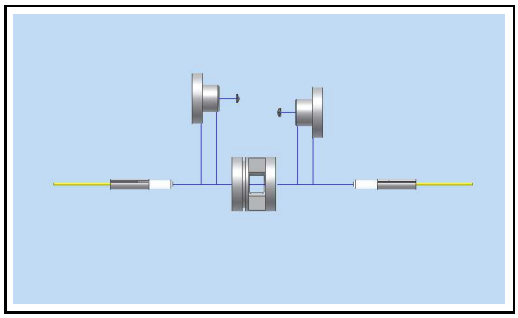

(c)

Figure 3.4 *– Faraday configuration; (a) Picture of the Faraday sample holder. (b) Schematic illustration of the sample holder. The light is brought to the sample with fibers and collimated. A second fiber collects the transmitted light. The light direction is parallel to the magnetic field. (c) Technical drawing of the sample holder, by S.George.*

The centre part of the sample holder was implemented with machinable ceramics in order to minimise the effect of thermal expansion on the optical path. The use of an insulating material also helps to suppress eddy currents that could give rise to vibrations and local heating.
The assembled setup is presented in figure 3.4a. The fibers are protected from liquid and evaporating helium in order to avoid vibrations in the optical path.
In order to enhance the signal in photoluminescence experiments we use six fibers to collect the response of the sample. The fibers are placed in a bundle as it is presented in figure 3.5. The fiber in the centre transports the incident light. The surrounding fibers are collecting the photoluminescence response. On the detector side the fibers are aligned in order to adapt the optical beam to the pixel geometry of the detector array as presented in figure 3.5b. A mirror can be placed behind the sample to increase the photoluminescence signal.

3.2.2 Voigt configuration

The second geometry in magneto-optical experiments is called *Voigt* geometry. Here the wave propagation vector is perpendicular to the magnetic field, i.e. $\underline{\mathbf{k}} \perp \underline{\mathbf{B}}$.

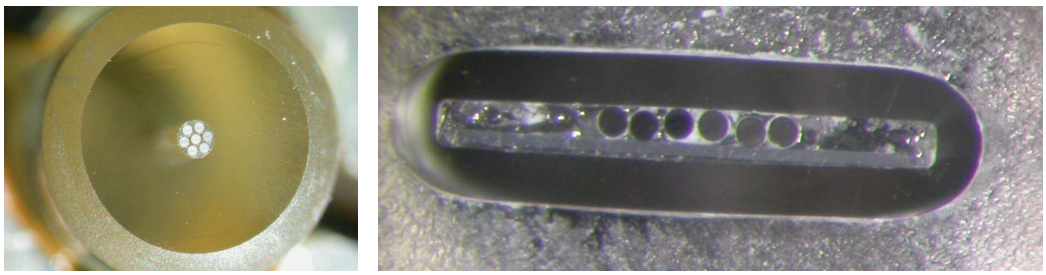

(a) **(b)**

Figure 3.5 *– Fiber setup for PL-experiments.(a) Fibers on sample side. The fiber in the centre is guiding the incident light.(b) The light is collected with the surrounding fibers and arranged in the same configuration as the detector array.*

The realisations of different sample holders are shown in figure 3.6. The beam is first reflected by a mirror placed at an angle of 45°, to put the light beam perpendicular to the magnetic field. Another 45° mirror sends the light to a second fiber which is connected to the detector. The sample is placed between the mirrors. In this configuration circumstances are slightly different since it is possible to work a sample holder monolithic. On the other hand there are more optical elements to fix. The sample holder for the 20 mm bore magnets are fabricated from a machinable ceramic.
Since there are commercially available prisms with an edge length which is small enough (≈ 1-2 mm), this setup could be reproduced for coils with a small bore, i.e. in 7 mm.
To complete the setup each sample holder has to be equipped with a pick-up coil as field sensor and a thermometer to control the temperature.
For photoluminescence experiments, we use exactly the same technique as in the previous section, i.e. the fiber bundle. A mirror is placed in 45° with respect to the bundle. It reflects the light to the sample and back to the collecting fibers.

(a)

(b)

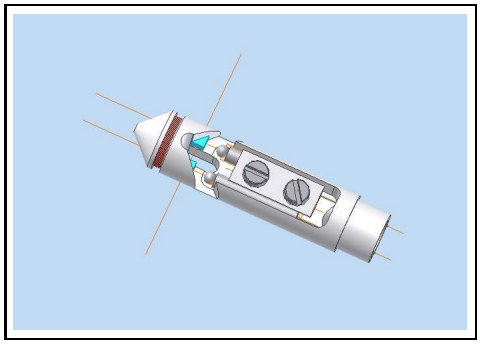

(c)

Figure 3.6 *– Voigt configuration; (a) Technical drawing of the sample holder for 7 mm cryostats; (b) Picture of the sample holder for bores of 20mm; (c) Picture of the sample holder for bores of 7mm.*

3.3 Magneto-optical spectroscopy

This last section of the chapter describes the methods used in this work. As mentioned we are working either with absorption spectroscopy, which is the major part of the present work, or with photoluminescence. The acquisition tools were also already presented in section 3.1.4.

3.3.1 Photoluminescence

The photoluminescence setups in Voigt and Faraday configuration are glass fiber based as already discussed in previous sections. We focus here more on available light sources. The main and most powerful light source for our photoluminescence experiments is a titanium:sapphire laser which provides tunable monochromatic light in the range between 700 and 1100 nm.
Other laser sources for photoluminescence experiments were conventional laser-diodes with various output powers.

3.3.2 Absorption spectroscopy

In our absorption spectroscopy measurements we used for all experiments a tungsten-halogen lamp providing a flat and broad spectrum from the visible to the near-infrared spectral range. This lamp is usually easy to connect to optical fibers and we can integrate it perfectly in our experimental setups.
For some measurements we also used a super-continuum laser as light source. It provides white light over a broad spectral range with an flat spectrum and very high power but with large fluctuations.

3.3.3 Polarisation

In order to get further information on a system, like its spin state, it is useful to polarise the light. Linear polarisation is rather simple to obtain. We use linear polarising laminated films close to the samples.
To create circular polarisation one has to add a $\lambda/4$-plate with its optical axis rotated over 45° with respect to the incident linear polarisation. For polarisation resolved experiments we used an achromatic $\lambda/4$-plate made from quartz providing circular polarisation better than 90% other the whole spectral range. An alternative method is to use mica plates as $\lambda/4$-plate.

Chapter 4

Carbon nanotubes in high magnetic fields

Contents

The discovery of carbon nanotubes is attributed to Sumio Iijima [Iijima 1991] in 1991 although this remains a contentious issue [Monthioux 2006]. The induced rush on this new material can be explained by its spectacular properties which even created some science fiction dreams [Edwards 2000].
Carbon nanotubes are the carbon allotrope which presents the case of a one dimensional confinement of their charge carriers due to their cylinder shape.
In this chapter we will first investigate the optical properties of SWNT under high magnetic fields and discuss the dark/bright exciton issue. In the second part of this chapter we will study the alignment of carbon nanotubes due to the application of a magnetic field.

4.1 Optical properties in high magnetic fields

The dipole allowed transitions which govern the optical properties of SWNT are illustrated in figure 2.8. Thus we can only observe absorption of photons within the bands E_{11}, E_{22} and sometimes E_{33} over a broad spectral range from ultra-violet

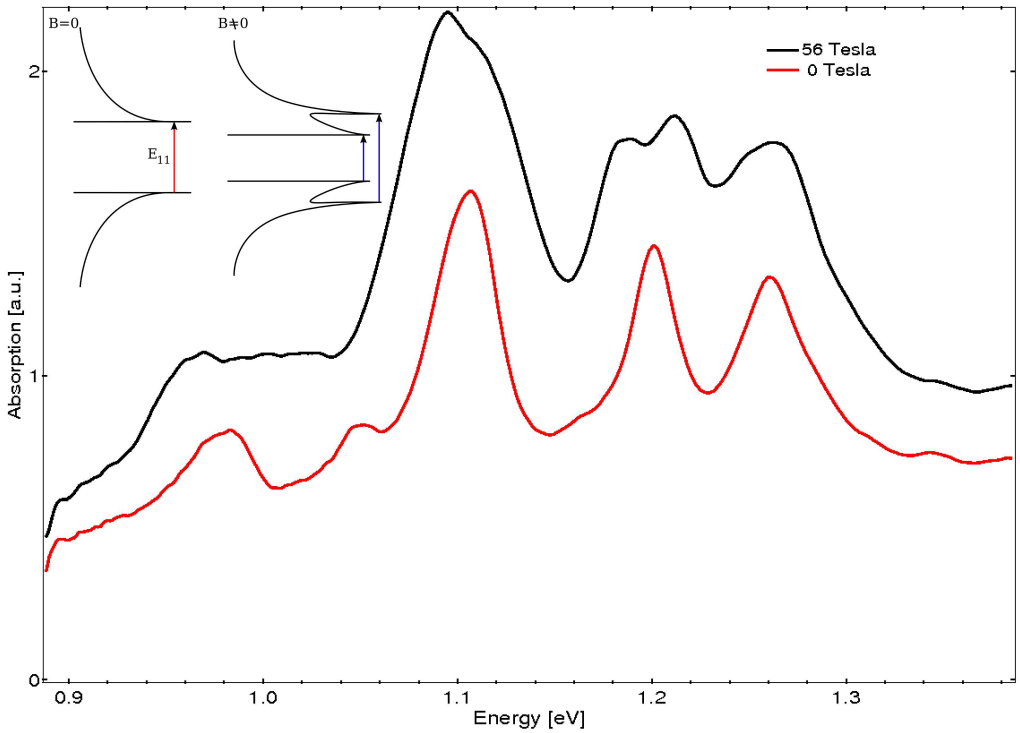

Figure 4.1 *– Absorption spectra of dispersed SWNT in presence and absence of a magnetic field in Voigt configuration. The absorption strength increases with increasing magnetic field and the peaks split. This splitting is referred to as Ajiki-Ando (AA) splitting and its principle is sketched in the inset. The traces are not offset and the increase in absorption is due to the tube alignment.*

(UV) to near-infrared (NIR), depending of the exact carbon nanotube type under study. Since the energies of these bands are unique for every type of tube, various optical experiments can be used to determine the tube chirality. The values for the transition energies from different SWNT types have been tabulated [Bachilo 2002]. Using this table we assign an absorption peak to the corresponding tube chirality. The table used as a reference in this work is displayed in appendix A.
The optical properties under magnetic fields are investigated in absorption and photoluminescence spectroscopy. The focus is on semiconducting nanotubes. We begin this section by describing absorption spectra of carbon nanotubes and connect our findings to the results of previous work.

4.1.1 Absorption spectra in magnetic fields

We have discussed the effects of a magnetic field applied parallel to the tube axis on the band structure of SWNT in section 2.5.1 and we will see how it explains the absorption spectra of SWNT obtained under influence of magnetic fields. Figure 4.1 shows two spectra of dispersed SWNT taken in absence and in presence of a magnetic field. Note that the traces are not offset, i.e. the absorption increases with

magnetic field. The main effect responsible for this observation is the alignment of SWNT which will be discussed extensively in section 4.2. In the measurements shown in figure 4.1 the tubes are suspended in an aqueous solution and thus can move freely. In addition to this we polarise the light parallel to the magnetic field in this measurement. At high field the nanotubes are aligned parallel to the magnetic field and the number of tubes obeying the selection rule developed in section 2.2.4, i.e. tubes only absorb light with an electric vector parallel to their long axis, is strongly increased. The absorption at maximum field can thus be understood on the basis of this effect.
More importantly, we can observe a splitting of the peaks or at least a strong broadening, in general a precursor to a splitting. This picture can easily be understood from the alignment described above and the modulation of the band structure induced by the Aharonov-Bohm effect (see figure 2.13b and the inset of figure 4.1). The bandgap is predicted to oscillate with a period of the quantum flux through the tube cross-section and it corresponds to the splitting we observe. The first observation of this effect was reported by Zaric *et al.* [Zaric 2004a].

4.1.2 Photoluminescence of carbon nanotubes

Photoluminescence experiments are a powerful tool in semiconductor physics to probe energy gaps and many-body physics. The mechanism consists of exciting an electron from the valence band to the conduction band and to measure the photon released when the electron relaxes back to the valence band.
SWNT will absorb a photon with an energy corresponding to the E_{22} bands. The relaxation of the electrons into the valence band releases a photon with an energy equal to the E_{11} separation. The emission energy is logically smaller or equal than the absorption energy, i.e. for excitation a laser in the visible spectral range is used while the collection is done with a NIR spectrometer. It is hence possible to "map" a SWNT sample by exciting the sample with different wavelengths and collect the response [Bachilo 2002].
Such maps are called Photoluminescence excitation (PLE) maps. An example case is displayed in figure 4.2. We measured a *HIPCO*-sample (High-Pressure CO Conversion) with different tube species inside. Every high intensity point can be attributed to a chirality with more precision than from only an absorption spectrum because the E_{11} and E_{22} bands are known simultaneously.

4.1.3 Excitons in carbon nanotubes

It was shown that SWNT have a very low quantum efficiency and that the temperature dependence of this efficiency is not consistent with a single particle picture [O'Connell 2002, Spataru 2005]. In section 2.2.4 we began to discuss that the optical response of carbon nanotubes is driven by excitons.
Electrons and holes pair through the Coulomb interaction and give rise to a new

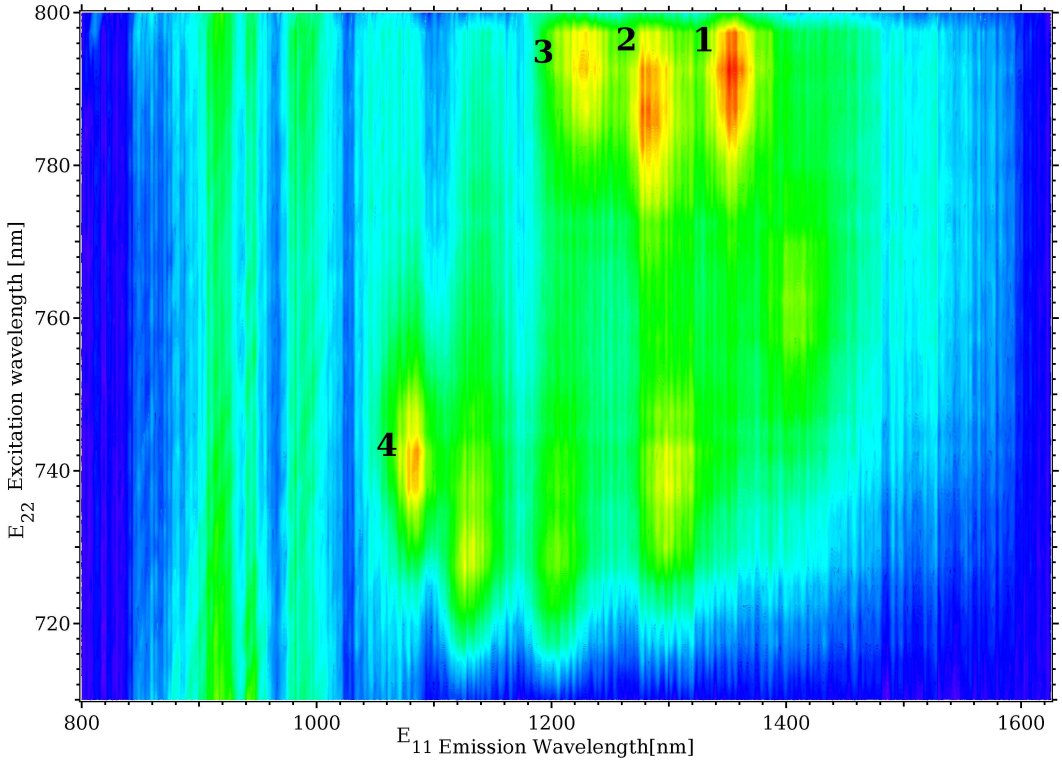

Figure 4.2 *– Example case of a PLE map measured on a HiPCO-SWNT sample. The y-axis is the wavelength of incident light. Red colour stands for the highest intensity and blue for the lowest. With help of PL and the assignment table a sample can completely be characterised. The advantage of this method in comparison with absorption is the simultaneous access to E_{11} and E_{22} which removes a lot of ambiguity. Thus the numbered peaks can be assigned: Peak 1:* $(9,7)$*;Peak 2:* $(10,5)$*;Peak 3:* $(12,1)$*;Peak 4:* $(11,0)$*.*

quasi-particle called exciton. Of particular interest are the four singlet states in SWNT since the triplet states are all optically inactive. The exciton dispersion relation of the four singlet states is presented in figure 4.3 for a $(9,4)$-tube [Shaver 2007a]. The optical bright bonding exciton, which has odd parity and zero angular momentum, follows a $k^2 \log|k|$ dispersion relation which is steeper than that for the dark states [Perebeinos 2005]. We can approximate the energy dispersion with a simple hyperbolic relation as a function of the centre of mass momentum k [Mintmire 1998]

$$E_i(k) = \sqrt{E_i(0)^2 + E_i(0)\frac{\hbar k^2}{m_i}} \tag{4.1}$$

where $i = \beta$ denotes the bright and $i = \delta, \alpha$ the dark states, $E_i(0)$ is the energy at $k = 0$ and m_i stands for the effective exciton mass. The lowest lying exciton state (δ), the anti-bonding state, has even parity and zero angular momentum.
This complex exciton manifold is supposed to be responsible for the weak quantum yield of carbon nanotubes, where the optically inactive states can trap much of the exciton population at low temperature [Perebeinos 2004]. The observed tempera-

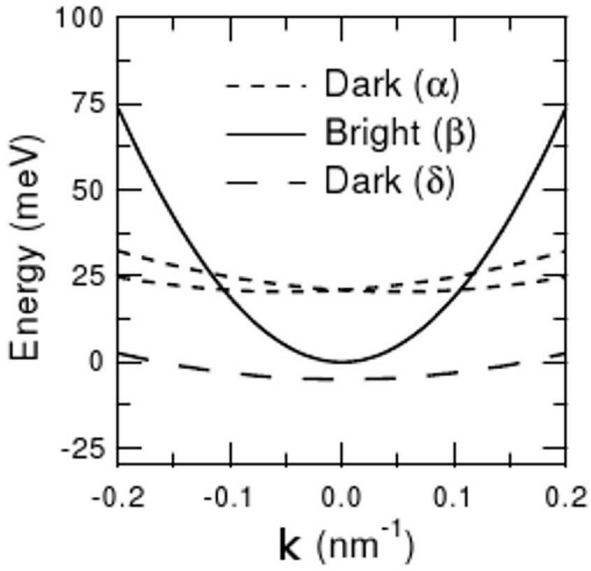

Figure 4.3 *– Singlet exciton dispersion relation for a (9,4) nanotube from [Shaver 2007a]. Away from the bottom of the band ($k = 0$) the dispersion is described by equation 4.1. The dark exciton with its energy below the bright state at the bottom band is predicted to brighten in a magnetic field.*

ture dependence can also be understood with the help of the picture of bright and dark excitons [Spataru 2005].

4.1.4 Magnetic brightening of dark excitons

A magnetic field has a strong influence on the exciton dispersions. In figure 4.4 we sketch the scenario for the exciton states of interest, i.e. the two singlet states with lowest energy at the bottom of the band. On the left hand sides of figures 4.4a and 4.4b, we have the single-particle representation and on the right hand sides the excitonic picture. In the absence of a magnetic field figure 4.4a is valid, where an electron can either be in the conduction band of the **K**-valley and a hole in the valence band of the **K**-valley or an electron can be in the conduction band of the **K**'-valley and a hole in the valence band of the **K**'-valley. The Coulomb interaction mixes these states and yields a bonding state which corresponds to the bright state of the excitonic representation and an anti-bonding state which corresponds to the excitonic dark state [Ando 2008]. In absence of a magnetic field the bottoms of the two exciton bands are separated by Δ_x, the dark-bright exciton splitting energy.
Ando has investigated the effect of a magnetic field on the lowest lying exciton state from theoretical point of view [Ando 2006]. In figure 4.4b we apply a magnetic field parallel to the SWNT long axis. The **K**-**K**'degeneracy is lifted which results in the oscillation of the bandgap that we have already discussed (compare figure 2.13b). The right hand side picture of figure 4.4b illustrates the effect of the magnetic field on the exciton dispersion relations. With increasing field the energy separation at

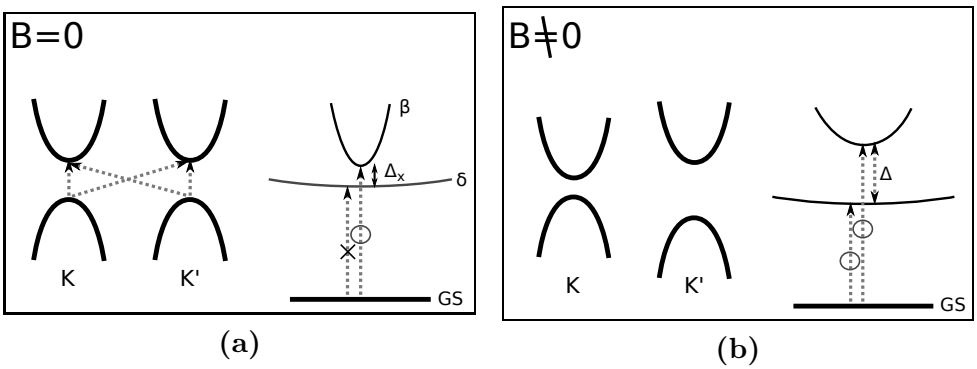

Figure 4.4 *– Single particle and excitonic representation of* ***K****-****K****'inter-valley mixing, adapted from [Zaric 2006]. (a) The single-particle picture sketches the four possible electron-hole pairs. The lowest lying states are the linear combination of the* ***KK****- and the* ***K****'****K****'-electron-hole-pairs. The two bands are separated at zero field by* Δ_x *in energy. (b) The field lifts the valley degeneracy. The initial dark state is brightened and the two excitons states shift away from each other with* $\Delta = \sqrt{\Delta_x^2 + \Delta_{AB}^2}$.

the bottoms of the bands is growing proportional to $\Delta = \sqrt{\Delta_x^2 + \Delta_{AB}^2}$. At the same time the magnetic field breaks the time reversal symmetry. The consequence is the lowering of the short range Coulomb-interaction, which mixes the even and odd parity states of zero angular momentum [Shaver 2007a]. Thus a spectral weight and effective mass redistribution is expected and the lowest initially dark exciton state is predict to brighten.
We can describe the whole picture by a phenomenological approach based on a two-level model [Shaver 2007b]. We use the following Hamiltonian to describe this two-band one dimensional magneto-exciton system:

$$\hat{H}(K) = \frac{E_\beta + E_\delta}{2}\hat{I} + \frac{E_\beta - E_\delta}{2}\hat{\sigma}_z + \frac{\Delta_{AB}(B)}{2}\hat{\sigma}_x \tag{4.2}$$

where $\hat{I}$ is a unit matrix and $\hat{\sigma}_x$,$\hat{\sigma}_z$ are Pauli matrices [Shaver 2008a]. $E_{\beta,\delta}$ are defined in equation 4.1. The relative oscillator strength is given by

$$I_\beta = \frac{1}{2} + \frac{1}{2}\frac{\Delta_x}{\sqrt{\Delta_x^2 + \Delta_{AB}^2}} \tag{4.3}$$

for the bright state and by

$$I_\delta = \frac{1}{2} - \frac{1}{2}\frac{\Delta_x}{\sqrt{\Delta_x^2 + \Delta_{AB}^2}} \tag{4.4}$$

for the dark state. Equations 4.3 and 4.4 are plotted in figure 4.5 as function of the Aharonov-Bohm splitting. In absence of a magnetic field only the bright state is observable, i.e. it has a relative oscillator strength of 1. Turning the magnetic field on yield the brightening of the dark state and redistribution of the relative

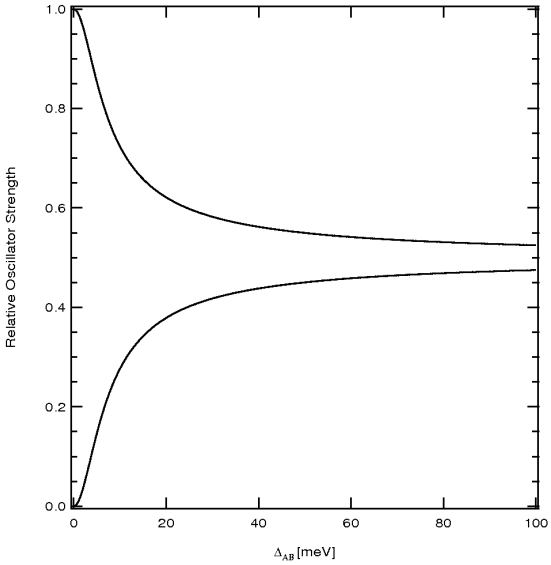

Figure 4.5 *– Relative oscillator strength from equations 4.3. At zero field we distinguish one bright state ($I_\beta = 1$) and one dark state ($I_\delta = 0$). For the latter case the oscillator strength is zero. At high fields the oscillator strengths are converging to the same value.*

oscillator strengths of the initial dark and bright states. For high magnetic fields, i.e. $\Delta_{AB} >> \Delta_x$, the two oscillator strengths are expected to converge to the same value.
The eigenvalues of the Hamiltonian in equation 4.2 are

$$\varepsilon_\beta = \frac{E_\beta(k) + E_\delta(k) + \sqrt{\left(E_\beta(k) - E_\delta(k)\right)^2 + \Delta_{AB}^2}}{2} \tag{4.5}$$

for the bright state and

$$\varepsilon_\delta = \frac{E_\beta(k) + E_\delta(k) - \sqrt{\left(E_\beta(k) - E_\delta(k)\right)^2 + \Delta_{AB}^2}}{2} \tag{4.6}$$

for the dark state. The contribution of the magnetic field manifests itself through the Aharonov-Bohm phase, Δ_{AB}, and mixes the wave functions of the dark and bright exciton sate. This mixing redistribute the effective masses and as discussed before the oscillator strength and leads to the brightening of the dark exciton. The higher energy exciton, denoted previously with α, are predicted to have similar effective masses to the dark band and negligible magnetic field dependence [Ando 2006, Perebeinos 2005].
The dispersions are plotted for the case of presence and absence of a magnetic field in figure 4.6. Without the magnetic field we find the same picture as in figure 4.3 for the two lowest lying states. In the presence of the magnetic field ($\Delta_{AB} \neq 0$) the splitting of the bottom of the bands Δ_x is increasing with increasing magnetic field. The bottom of the band is of particular interest because optical absorption and emission takes place for $k \approx 0$, where the exciton population is the highest.

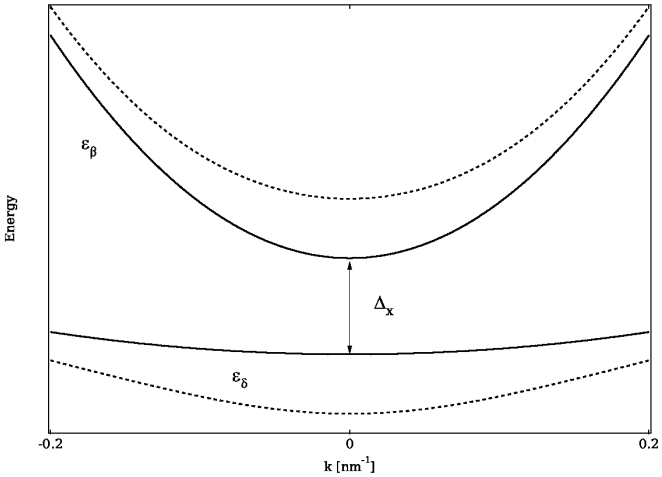

Figure 4.6 *– Exciton dispersion for the two lowest lying singlet states plotted with help of equations 4.5 and 4.6. Solid lines represents the dispersion in absence of a magnetic field, i.e.* $\Delta_{AB} = 0$ *and the dashed lines the case with* $\Delta_{AB} \neq 0$.

4.1.5 Experimental Results

The aim of this section is to show that only a magnetic field parallel to the tube axis affects the properties of SWNT discussed before. The samples used in this experiment are DNA-wrapped CoMoCAT SWNTs dispersed in a polyacrylic acid (PAA) matrix. These samples have a strong PL signal, sharp absorption features, are temperature stable and can be stretch aligned [Fagan 2007]. This latter feature is important because it makes it possible to clearly identify the role of the magnetic flux threading the SWNT.
The degree of alignment of these samples is characterised by the effective angle θ_{eff} of the sample with respect to the stretch axis $\hat{n}$, as defined by the nematic order parameter S

$$S = \frac{3\cos^2(\theta_{eff}) - 1}{2}. \tag{4.7}$$

We use θ_{eff} =21° for this samples, determined from polarised Raman spectroscopy [Fagan 2007].
The configurations of the measurements presented in this section are sketched in figures 4.7a and 4.7b. Absorption and photoluminescence experiments were performed on these samples in collaboration with the group of *J.Kono* at the Rice university and the NHMFL in Los Alamos [Shaver 2008b, Shaver 2008a]. Figure 4.7c shows absorption spectra in zero field and at 55 T in the different geometries at 4 K. The dominant absorption peak is that of the $(6, 5)$ tube on which we will focus on in this section. The solid blue line is the absorption of the sample in Faraday geometry. We can only notice an almost vanishing change in comparison to the zero-field absorption. However, strong PL intensity enhancement in this configuration was reported by Mortimer *et al.* [Mortimer 2007a]. This behaviour is

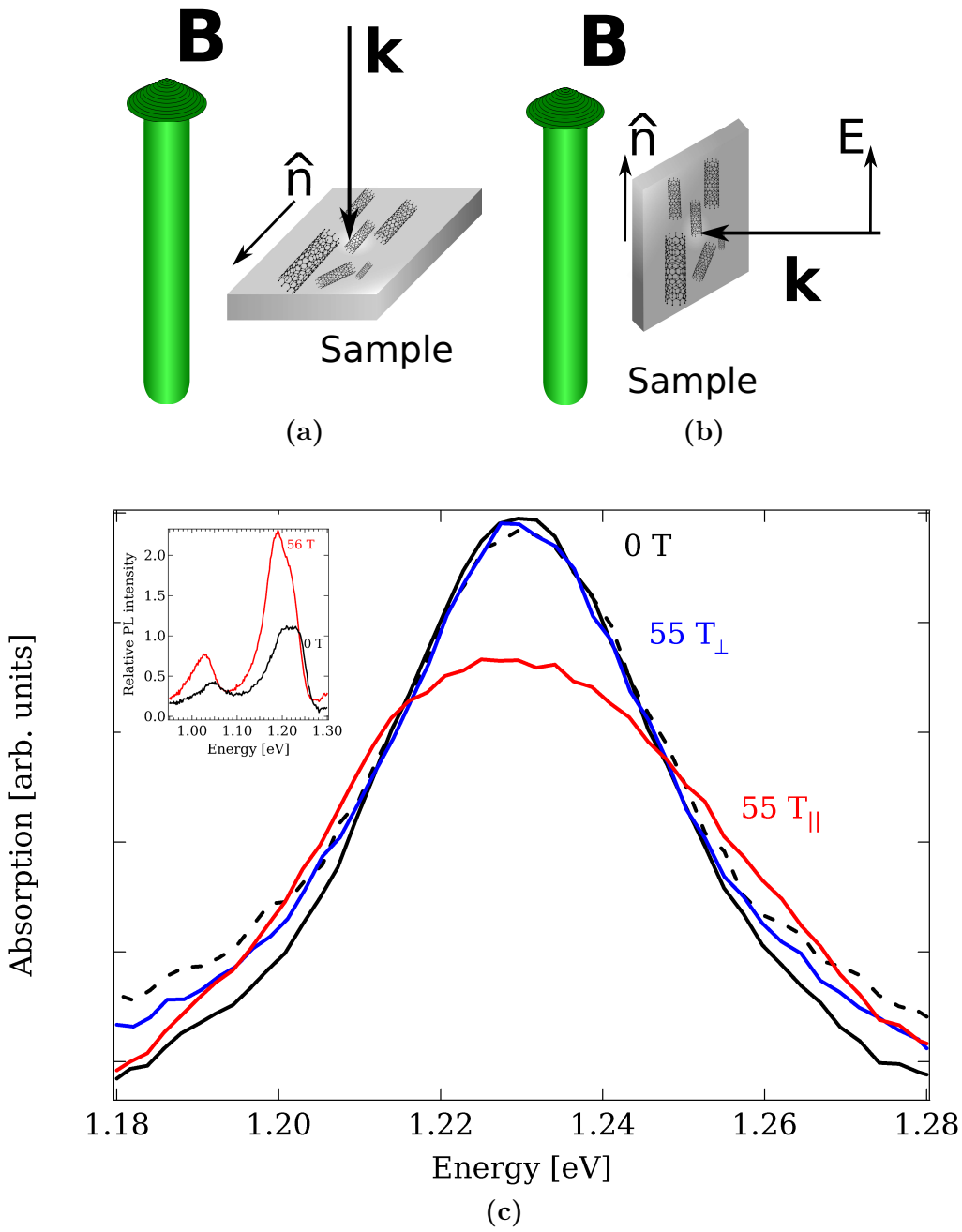

Figure 4.7 – *Measurement configuration in Faraday (a) and Voigt configuration (b). (c) Absorption spectra of stretch aligned SWNT film in Faraday (blue) and Voigt (red) geometry with parallel polarisation with respect to the stretch axis. Solid black and dashed black lines are the zero field spectra for Voigt and Faraday configuration respectively. Spectral changes are observed when the threading magnetic flux and the light polarisation are parallel to the tube axis. The inset presents the PL response of the sample at 0 T and 55 T in Voigt configuration and parallel polarisation. The intensity is normalised with respect to the dominant* $(6,5)$ *peak at zero-field.*

unexpected because, as it also follows from our absorption measurements, we are not supposed to observe a modification of the bandgap energy when the magnetic field is not parallel to the tube axis. In addition to this observation, Mortimer *et al.* identify an unexpected tube diameter dependence of this effect, i.e. the dark and bright exciton splitting decreases with increasing tube diameter although the inverse is expected. The authors attribute this behaviour to the role of the spin and to the closeness of the lowest lying singlet and highest triplet state [Mortimer 2007b]. Changes in the spectrum of our experiment become only significant in the Voigt configuration with light polarised parallel to the magnetic field and to the tube axis (solid red line in figure 4.7c). We clearly observe a decrease in absorption and a broadening of the peak. To double check our findings in absorption spectroscopy we have added an inset in figure 4.7c with the photoluminescence response of the sample in absence and at high magnetic field (55 T) in Voigt configuration and parallel polarisation. The traces are normalised by the zero-field intensity of the dominant $(6,5)$ peak. We note strong intensity increase and a clear red shift with respect to the initial position, observed in many experiments before [Shaver 2007b, Mortimer 2007a].
This result is also obtained with photoluminescence experiments in a long pulse magnet at the NHMFL in Los Alamos presented in figure 4.8a. It is clearly seen that $\hat{n} \parallel B$ demonstrates stronger brightening and larger redshifts at a given $\mathbf{B}$ than $\hat{n} \perp B$. Note that the non-linear shift of the emission energy is a direct consequence of the excitonic nature of the optical response.
To demonstrate that only the magnetic field component parallel to the tube axis, $B_{\parallel}$, is important in determining the PL peak energy, we plotted the peak energy data for both configurations in figure 4.8b as a function of $B_{\parallel}$. $B_{\parallel}$ is defined by

$$B_{\parallel} = B \cdot \cos\left(\theta_{eff}\right) . \tag{4.8}$$

Using an effective angle of Θ_{eff} =13° results in a nearly perfect overlap in functional form of peak shift versus $B_{\parallel}$ between the two configurations. The corresponding alignment is slightly higher than previously determined from polarised Raman data, possibly due to the contribution of non-luminescent species, to the Raman experiment. However this result shows that the observed magnetic field dependence of our photoluminescence experiments is mostly due to the field component parallel to the tube $B_{\parallel}$. Large PL enhancements recently reported for randomly aligned samples in the Faraday geometry are therefore most likely due to a population of SWNTs with significant threading flux.
Optical absorption is predicted to take place at $k \approx 0$. We set $E_{\beta}(0) = 0$ and simplify equations 4.5 and 4.6 to

$$E_{\beta,\delta} = \frac{-\Delta_x \mp \sqrt{\Delta_x^2 + \Delta_{AB}(B)^2}}{2} \tag{4.9}$$

with $\Delta_x = E_{\beta}(0) - E_{\delta}(0)$. The Aharonov-Bohm term is defined through

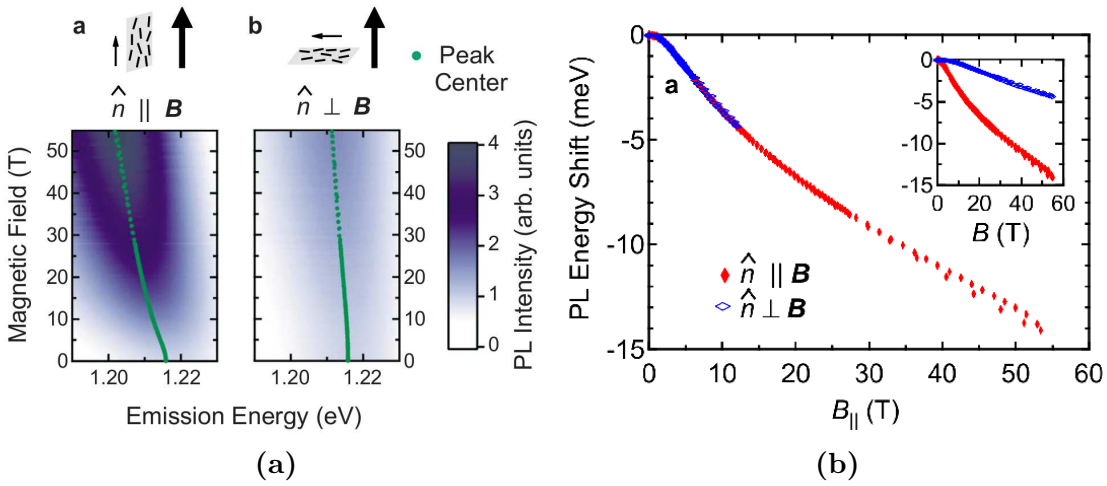

Figure 4.8 *– (a) Contour plots of PL intensity as a function of magnetic field with nanotubes aligned (a) parallel ($\hat{n} \parallel B$) to and perpendicular ($\hat{n} \perp B$) to the magnetic field. As the magnetic field increases, the PL peak shifts and increases in intensity. (b) PL peak shift as a function of the SWNT-parallel component of* ***B*** *($B_{\parallel}$) for $\hat{n} \parallel B$ (red vertical diamonds) and $\hat{n} \perp B$ (blue horizontal diamonds). The peak energy matches exactly for both geometries [Shaver 2008b]. The inset shows the raw experimental data.*

$$\Delta_{AB} = \mu\Phi = \mu\frac{\pi d^2 B_{\parallel}}{4} \tag{4.10}$$

where μ is a proportionality constant and d the tube diameter.
We now fit the experimental data to determine the dark-bright exciton splitting at zero field (Δ_x). The advantages of absorption spectroscopy are the direct measurement of the band-energy and oscillator strengths and the lack of convolution with the thermal distribution of excitons. In contrast to photoluminescence experiments at low temperature where only the dark exciton is visible because the exciton population is restricted to this formally dark state, i.e. the lower energy state, we observe in absorption spectroscopy both, the bright and dark exciton absorption peaks. The lack of clear splitting in the absorption spectra does not allow an accurate fit of this experiment, however. We will thus use the photoluminescence data to determine the value of Δ_x.
In figure 4.9 we fit the experimentally obtained peak positions of the dark excitons with the help of equation 4.9. Due to the low temperature and the increase of the magnetic field such that $\Delta_{AB} \gg k_B T$, the photoluminescence response is restricted to the formally dark state. Only the points in the high field region were used to fit the data. Despite the few experimental points which were used to fit the data in figure 4.9a, the model reproduces all data quite well. We obtain values for the dark-bright exciton splitting of $\Delta_x = 4.0$ meV and for the proportionality constant $\mu = 1.05$ meV/T nm^2. The value of Δ_x and μ are in very good agreement with the results obtained on the same sample family in photoluminescence studies in a long-

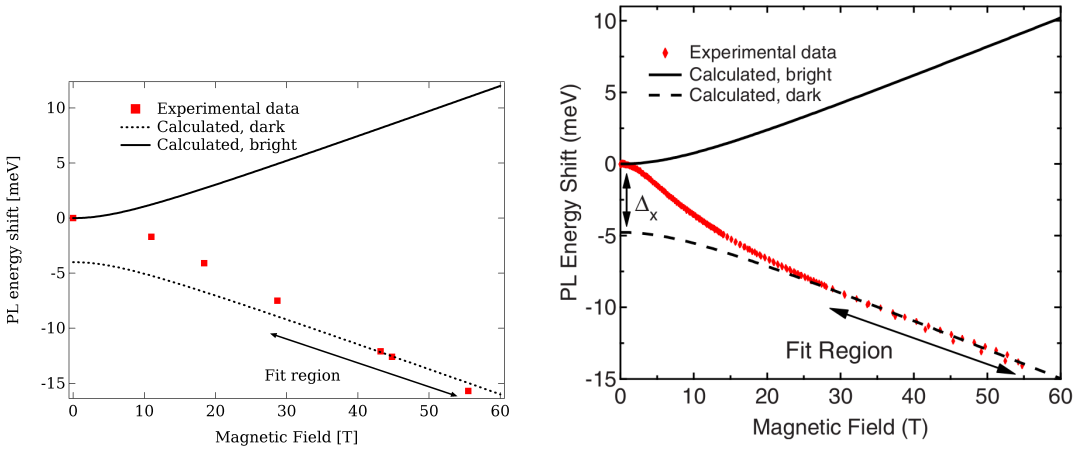

Figure 4.9 *– (a) The relative position of PL peaks as a function of magnetic field for the data acquired in Toulouse. Equation 4.9 is used to fit the points. The result yields a dark-bright splitting of $\Delta_x = 4.0$ meV and $\mu = 1.05$ meV/T nm^2, (b) Experimental (red diamonds) and calculated (solid and dashed lines) peak energy as a function of the SWNT-parallel component of magnetic field. The values $\Delta_x = 4.8$ meV and $\mu = 0.93$ meV/T nm^2 were determined by fitting the high magnetic field data. The values were used to extrapolate the complete field dependence of dark (dashed line) and bright (solid line) excitons [Shaver 2008b].*

pulse magnet which is shown in figure 4.9b [Shaver 2008a, Shaver 2008b]. The fit in figure 4.9b yield $\Delta_x = 4.8$ meV and $\mu = 0.93$ meV/T nm^2. These values are used to extrapolate the field dependence, presented in the figures 4.9. The agreement between theory and experiment supports the significance of $B_{\|}$ for determining the optical properties of SWNT. It also confirms the theoretical model developed in section 4.1.4.

Recent reports on photoluminescence measurements in DC-field magnets showed that strain can influence the value of the dark-bright zero field splitting [Nish 2008]. Direct observation of dark and bright excitons was also reported recently by photoluminescence on single carbon nanotubes [Matsunaga 2008, Srivastava 2008]. The measurements present the advantage to show very sharp peaks (few meV) and thus can resolve the dark and bright exciton peak unambiguously.

4.2 Dynamic alignment of SWNT

In section 2.5.2 we discussed the magnetic properties of SWNT. Calculations and experiments showed the existence of a magnetic anisotropy. Semiconducting tubes are diamagnetic both along and perpendicular to their long axis but the magnitude of the perpendicular susceptibility is higher. Metallic tubes are paramagnetic along their long axis and diamagnetic perpendicular to it. For both tube families the application of an external magnetic field will induce an alignment of the SWNT

with their long axis parallel to the magnetic field, if the tubes can move freely. The aim of this section is to investigate the dynamical behaviour of nanotubes under influence of a magnetic field.

4.2.1 Linear dichroism

From the selection rules exposed in section 2.2.4 we know that SWNT only absorb light with an electric vector parallel to the tube's long axis. This makes the use of linear dichroism a convenient tool to analyse the alignment of SWNT. Linear dichroism is a common technique to study the orientation of molecules and is usually easy to interpret [Rodger 1997].
Linear dichroism is defined as the difference between light linearly polarised parallel and perpendicular to an orientation axis . In our case this axis will be along the direction of the magnetic field.

$$LD = A_{\parallel} - A_{\perp} \tag{4.11}$$

The absorbance is defined as the logarithm ratio of light transmitted through a sample, T_s, and light transmitted through the background medium, T_0.

$$A = -\ln\left(\frac{T_s}{T_0}\right) \tag{4.12}$$

If the absorbance of the medium is polarisation independent the respective background contribution cancels out. Thus we can express equation 4.11 as a function of the transmittance of our ensemble of nanotubes, $T_\perp$ and $T_\parallel$, and we write

$$\begin{aligned} LD &= -\ln\left(\frac{T_\parallel}{T_0}\frac{T_0}{T_\perp}\right) \\ &= -\ln\left(\frac{T_\parallel}{T_\perp}\right). \end{aligned} \tag{4.13}$$

Figure 4.10 shows a plot of the linear dichroism of SWNT, suspended in an aqueous solution at a field strength of 71 Tesla as a function of photon energy. The experiment is performed in Voigt configuration at room temperature. The sign of the trace is positive everywhere. This is consistent with parallel alignment of nanotubes with respect to the magnetic field, as it follows from the selection rules of SWNT exposed in section 2.2.4 and the definition of the linear dichroism in equation 4.11. We additionally observe distinct peaks in the linear dichroism spectrum which can be explained by the presence of different tube chiralities in the sample. The peaks in the spectrum are the E_{11} absorption band energies, or more precisely the split absorption bands due to the Aharonov-Bohm effect, of the tubes present in the sample. We can conclude that all chiralities present in the sample are at least beginning to align parallel to the magnetic field. Hence the presence of a magnetic anisotropy in carbon nanotubes is verified.

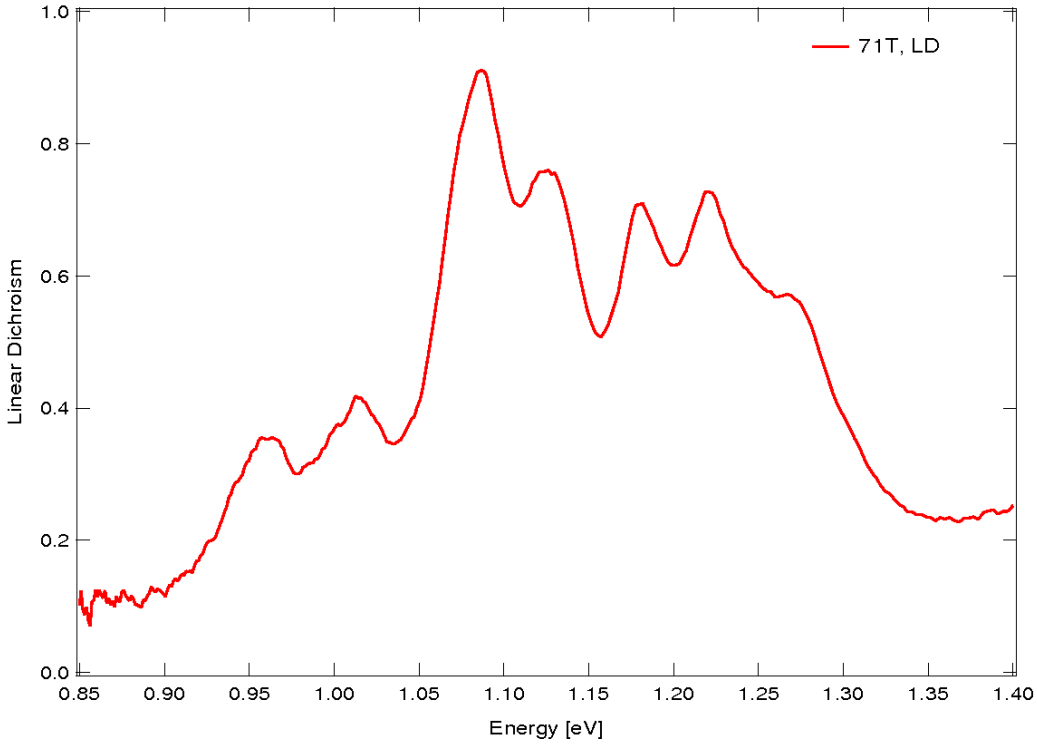

Figure 4.10 *– Linear dichroism spectrum of SWNT individually suspended in an aqueous solution at 71 Tesla. From the positive sign of LD we conclude that the alignment is parallel to the magnetic field. The peaks in the spectrum correspond to the different chiralities which are present in the solution.*

In the following, we will plot our linear dichroism data against time which makes it straightforward to compare to the magnetic field. When we express equations 4.11 and 4.12 as function of time we simply get:

$$LD(t) = A_{\parallel}(t) - A_{\perp}(t) = -\ln\left(\frac{T_{\parallel}(t)}{T_{\perp}(t)}\right) \tag{4.14}$$

We first note that two independent measurements, one for each polarisation, are necessary to determine the linear dichroism. Long-term fluctuations of the radiation source as well as the practical necessity to manipulate optical components between these measurements make it all but impossible to guarantee accurately reproducible conditions for the setup as a whole. However, by ensuring that the sample is homogeneous, well positioned and has the form of a plane-parallel slab we can at least make sure that the relevant interaction giving rise to $T_{\perp}(t)$ and $T_{\parallel}(t)$ remains independent of the exact point and – within the experimental limits – also the angle of incidence.
We now turn to including characteristics of the optical setup in order to express the linear dichroism as a function of the radiation intensities that are actually measured. The following expression relates the intensity I_{detector} measured at the

detector to the intensity I_{incident} on the sample via the transmittances T_{sample} and T_{setup} of the sample and the optical path between sample and detector.

$$I_{\text{detector}} = T_{\text{setup}}\, T_{\text{sample}}\, I_{\text{incident}} \tag{4.15}$$

It has already been mentioned above that T_{setup} and I_{incident} may vary from one experiment to the next. However, we can safely assume that no such changes occur *within* each experiment, i.e. while the magnetic field is applied and immediately beforehand. Thus,

$$\begin{aligned} T_{\text{setup},\perp}(B,t) = \quad & T_{\text{setup},\perp}(0,0) \neq \quad T_{\text{setup},\parallel}(B,t) = \quad T_{\text{setup},\parallel}(0,0), \\ I_{\text{incident},\perp}(B,t) = \quad & I_{\text{incident},\perp}(0,0) \neq \quad I_{\text{incident},\parallel}(B,t) = \quad I_{\text{incident},\parallel}(0,0). \end{aligned} \tag{4.16}$$

It is easy to see that by making use of these relations, equation 4.13 can again be rewritten as a function of the intensities $I_{\text{detector},\perp}(B,t)$, $I_{\text{detector},\perp}(0,0)$, $I_{\text{detector},\parallel}(B,t)$ and $I_{\text{detector},\parallel}(0,0)$ measured independently for each polarisation before and during the application of an external magnetic field.

$$\begin{aligned} LD_{\text{SWNT}}(B,t) &= \ln \frac{I_{\text{detector},\perp}(B,t)}{I_{\text{detector},\perp}(0,0)} - \ln \frac{I_{\text{detector},\parallel}(B,t)}{I_{\text{detector},\parallel}(0,0)} \\ &= -\ln\left(\frac{I_{\text{detector},\parallel}(B,t)}{I_{\text{detector},\perp}(B,t)}\right) - \ln\left(\frac{I_{\text{detector},\perp}(0,0)}{I_{\text{detector},\parallel}(0,0)}\right) \end{aligned} \tag{4.17}$$

The second term in equation 4.17 vanishes in the best case when $\frac{I_{\text{detector},\perp}(0,0)}{I_{\text{detector},\parallel}(0,0)} = 1$. This ratio remains nevertheless constant because these are only dependent on the differences of T_{setup} and I_{incident} between two experiments. This finally just sets an offset to the linear dichroism. Thus we can correct the experimental data by subtracting the ratio of the the zero field transmissions from the linear dichroism. A measurement of the LD allows us to determine the average alignment of the tubes. Dividing LD by the zero field absorbance of the sample yields the reduced linear dichroism LD^r :

$$LD^r = \frac{LD}{A} = \frac{A_\parallel - A_\perp}{A}. \tag{4.18}$$

Linear dichroism is usually an ensemble measurement and we express the alignment in the form of an effective angle, θ_{eff}. This effective angle is however an average over all orientations in the sample.

$$\cos^2(\theta_{\text{eff}}) = \langle \cos^2(\theta) \rangle \tag{4.19}$$

The nematic order parameter S is defined by

$$S(\Theta) = \frac{3\cos^2(\theta_{\text{eff}}) - 1}{2}, \tag{4.20}$$

as briefly discussed in section 4.1.5. We can now extend the reduced linear dichroism as a function of the effective angle for the general case [Rodger 1997]:

$$LD^r = 3 \cdot \left(\frac{1}{2} \left(3\cos^2(\alpha) - 1 \right) \cdot \frac{1}{2} \left(3\langle \cos^2(\theta) \rangle - 1 \right) \right) = 3 \cdot O(\alpha) \cdot S(\theta) \tag{4.21}$$

α represents the angle between the transition moment and the tube axis. The selection rules for light absorption imply [Shaver 2009] $\alpha = 0$ and the absolute alignment can be expressed through

$$LD^r = 3S(\Theta) = 3 \cdot \left(\frac{1}{2} \left(3\langle \cos^2(\theta) \rangle - 1 \right) \right) \tag{4.22}$$

Note that this remains an average description. When the value of the order parameter is close to 1 or $-\frac{1}{2}$, we can confidently conclude that the angle of the tubes is close to 0° or 90° with respect to the orientation axis. For the case $S = 0$ we get $\langle \cos^2(\theta) \rangle = \frac{1}{3}$ and $\theta = 54,7°$. But we can not deduce if the angle of all tubes is $54,7°$ or if the orientation is isotropic because $S = 0$ is the definition of isotropic orientation [Rodger 1997].

4.2.2 Experimental results

In the NIR we have a strong splitting of the absorption lines which is discussed in previous chapters. To avoid spectral induced changes as we see them for example in figure 4.10 (Aharonov-Bohm phase-shift), we integrate over the whole spectral range. The transmission is written

$$T^{av}_{\perp,\parallel} = \frac{1}{\varepsilon_1 - \varepsilon_2} \int_{\varepsilon_1}^{\varepsilon_2} d\varepsilon \frac{T_{\parallel,\perp}(\varepsilon, t)}{T_0(\varepsilon)} \tag{4.23}$$

The splitting in the E_{22} band is much weaker. Thus we can use wavelengths in the visible spectral range to make chirality dependent measurements. However the NIR-spectrometer is more powerful than the one for the visible spectral range. Here the experimentalist has to make a choice between performance and resolution. In a first time the aim is to generally describe the dynamic behaviour and an ensemble measure will be sufficient.
The whole process is a competition between the magnetic field, which tends to align the nanotubes, and the Brownian motion, which creates isotropic orientation in absence of external forces. The degree of alignment in equilibrium can conveniently be expressed by the ratio [Walters 2001]

$$\xi = \sqrt{\frac{B^2 \cdot N \cdot \Delta\chi}{k_B \cdot T}}, \tag{4.24}$$

where N denotes the number of carbon atoms in the SWNT, k_B the Boltzmann-constant and T the temperature. $\Delta\chi$ is known from equation 2.44. From equation

4.24 we can derive the condition to observe an alignment of nanotubes. The alignment energy has to be higher than the randomising energy and thus $\xi > 1$. In thermal equilibrium we can compute an angular distribution function $P(\theta)$, using θ as the angle between the tube's long axis and the magnetic field

$$\frac{\mathrm{d}P(\theta)}{\mathrm{d}\theta} = \frac{e^{\xi^2 \cos^2(\theta)} \sin(\theta)}{\int_0^{\pi/2} e^{\xi^2 \cos^2(\theta)} \sin(\theta)\ \mathrm{d}\theta} \tag{4.25}$$

4.2.2.1 Characterised DNA-wrapped SWNT

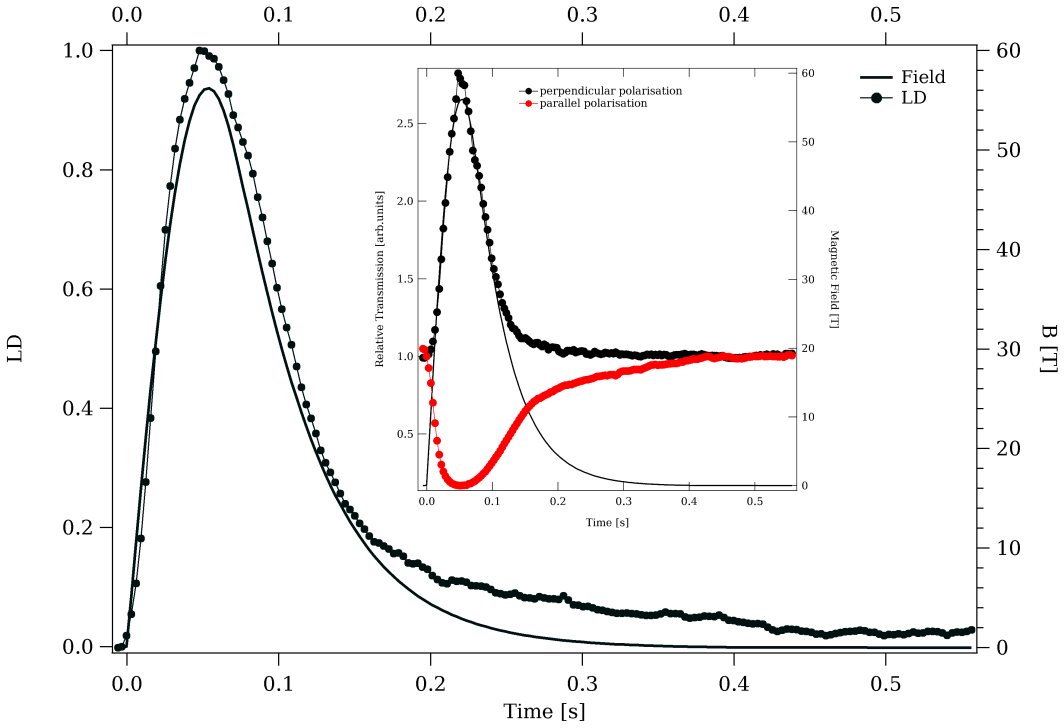

Figure 4.11 *– The linear dichroism of SWNT in a pulsed magnetic field as function of time (black circles + line). The magnetic field pulse is plotted for comparison (solid black line, right axis). Inset: transmission of the sample in perpendicular and parallel polarisation. By bringing the curves of the inset into relation we get the linear dichroism. The optical signals are almost following the magnetic field pulse.*

The samples are DNA wrapped HipCo single-walled nanotubes dispersed in 1% ioxidanol [Fagan 2006]. The tubes are individually suspended. The measurements are performed in Voigt geometry. The polariser is placed adjacent to the samples. An important parameter for further description of the alignment dynamics is the nanotube length, l. The nanotube length distribution in a sample can be determined by atomic force microscopy (AFM) or rheology measurements [Parra-Vasquez 2007]. We used the latter technique to determine the length distribution in the sample and we assume a log-normal probability distribution

$$\Omega(l) = \frac{1}{l\sigma\sqrt{2\pi}}\, exp\left(-\frac{(ln\ (l-\mu))^2}{2\sigma^2}\right) \tag{4.26}$$

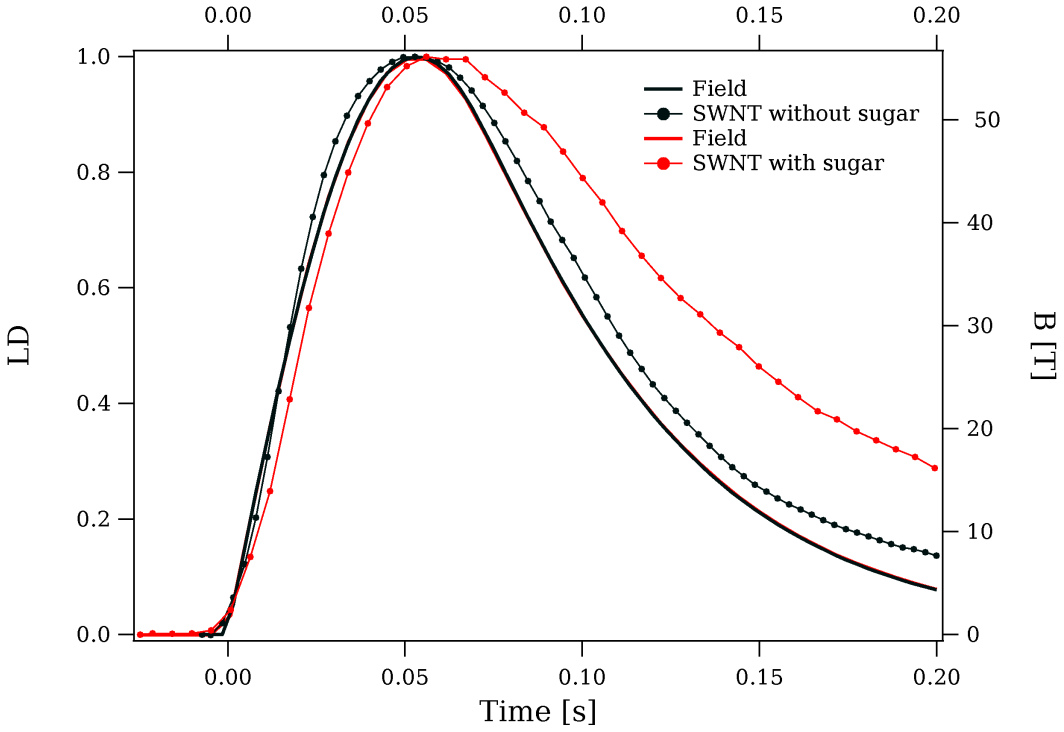

Figure 4.12 *– The normalised linear dichroism of the sample without and mixed with sugar. The higher viscosity has an influence on the dynamic of the process, delaying alignment and disalignment. This confirms the existence of a viscous drag. The lines between the points are guiding lines.*

where μ and σ are the mean value and the standard deviation respectively of the tube length l. The results of the rheology measurement yield a standard deviation of $\sigma = 0.8668$ and a mean length of $l = 168$ nm, with $\mu = log(l)$ and show that the sample is in the dilute regime[1].

Figure 4.11 shows the typical result for the alignment of SWNT in a pulsed magnetic field. The inset plots the transmission normalised by the zero field transmission, versus time. Once one measurement of each polarisation is obtained, we can use relation 4.17 to calculate the linear dichroism. We additionally normalised the LD by its maximum value. Although this washes out the information about absolute alignment, it is convenient to use this representation when the dynamics are compared [Shaver 2009]. We also plot the magnetic field pulse against time (solid black line and right axis). We note at first the resemblance between the linear dichroism and the magnetic field pulse. Two features are however altering the process. The

[1]Private communication J.Shaver, A.N.G.Parra-Vasquez

response of the alignment to the increase of the magnetic field is slightly delayed and the disalignment that lags behind towards the end of the pulse. Both features confirm the influence of a viscous drag that delays the establishment of equilibrium conditions [Ubrig 2010]. Note that the points represent averaged spectra in energy and time. We observe some points which seem to align before the start of the magnetic field but can attribute this to the averaging.
In order to investigate this effect further we varied the viscosity of the sample. To realise this variation we added 50% by weight of a mixture of sucrose and glucose in a 60/40 ratio. The results are shown in figure 4.12 where we compare the normalised alignment of the samples with low and high viscosity. The thickened solution strongly delays the features of alignment and disalignment. The maximum alignment is obviously delayed for the high viscosity sample with respect to the magnetic field. This clearly indicates a viscous movement of the SWNTs.
The temperature is an important parameter for the description of the alignment process and we studied the temperature dependence of both samples. The results for the sample mixed with sugar is shown in figure 4.13 while for the samples with low viscosity no detectable temperature dependence could be identified. We already saw in figure 4.12 that the disalignment is strongly slowed down for the high viscosity solution. Decreasing temperature enhances this effect.
This picture is in good agreement with the existence of a viscous drag. With increasing temperature the viscosity is lowered and a faster alignment is achieved when the field rises. The Brownian motion is enhanced at higher temperatures and an isotropic orientation is obtained faster with decreasing field.

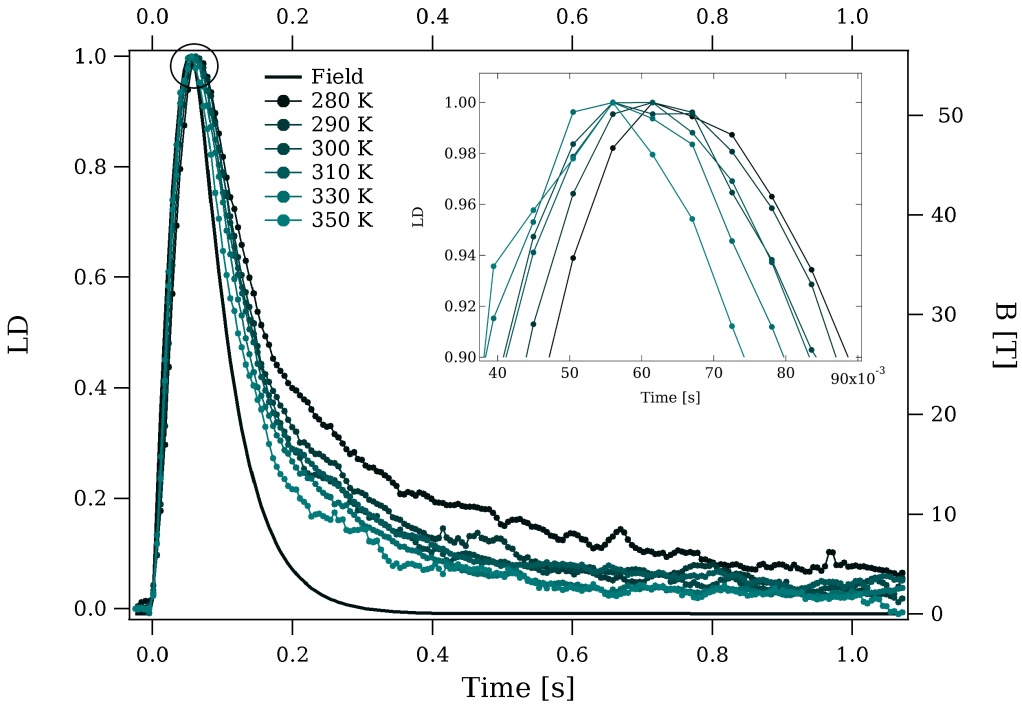

Figure 4.13 *– Normalised linear dichroism curves at temperature between 280 and 350 K for the sugar solution. A clear influence of temperature is becoming visible only at high viscosity. Increasing temperature induces faster alignment and disalignment, which is in perfect agreement with the picture of Brownian motion and viscous drag. In the inset we present a zoom of the region marked by a circle.*

4.2.2.2 Length Sorted SWNT

Because the analysis of samples with a broad length dispersion is complicated, we have investigated length sorted samples [Zheng 2003]. Two different sample batches were used for these experiments. In the first sample the main SWNT species is the (7,6) tube and the length is about 1 μm. The sample is dialyzed into 1 % mass/volume sodium deoxycholate (DOC). The main SWNT of the second sample is the (6,5) tube and the tube length in this solution is about 1.2 μm. The sample is in 10% iodixanol and 2% DOC. The absorbance of each sample is plotted as a function of the photon energy in figure 4.14. The strongest peak in each spectrum corresponds respectively to the $(7,6)$ and $(6,5)$ nanotube in figure 4.14a and figure 4.14b.

When measuring the magnetically induced linear dichroism for these samples, the alignment dynamics is found to be strongly different from the features observed in section 4.2.2.1. The linear dichroism dynamics for each sample is plotted in figure 4.15. The alignment in the magnetic field follows the magnetic field as we have seen before. The maximum alignment and the maximum field coincide. However in the down sweep and after the magnetic field the tubes are disaligning very slowly. This

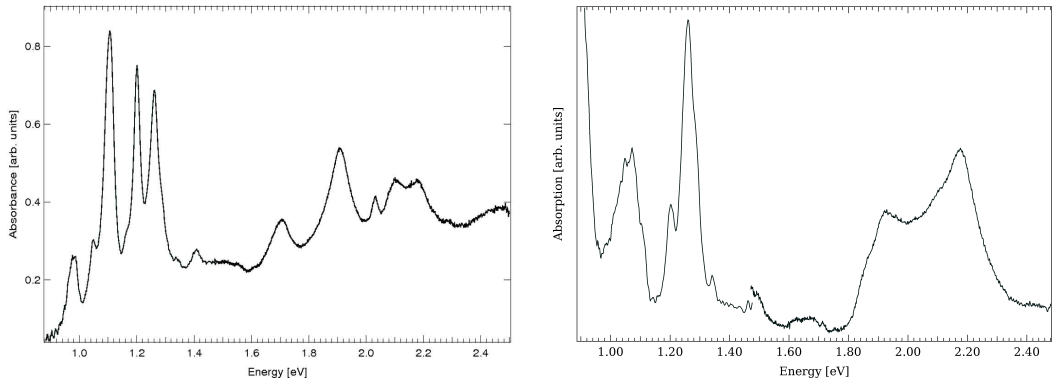

(a) **(b)**

Figure 4.14 *– Absorption spectra of two length sorted SWNT samples used in this section. (a) The so-called* $(7,6)$*-batch, with dominant* $(7,6)$ *nanotube and 1* μ*m length. (b) The so-called* $(6,5)$*-batch, with dominant* $(6,5)$ *nanotube and 1.2* μ*m length. The absorption spectra are showing well defined sharp lines. Two spectrometers were used to record other this whole spectral range.*

is in complete contrast to our previous observations, where even at high viscosity the initial, isotropic, state is recovered in less than 1 second, while the present case shows still significant alignment several seconds after the pulse. In addition there seems to be a large difference between the two samples in terms of absolute alignment. In order to clearly determine the amount of alignment in the sample we also measure the reduced linear dichroism.
In this series of experiments we use two different magnetic field pulses. In a first time we apply a 60 Tesla 300 ms long pulse of the 14 MJ generator, described in chapter 3. To complete the measurements we used the 70 Tesla short pulse combined with a 1 MJ transportable capacitor bank of the LNCMI-Toulouse. The pulse length was 20 ms. In figure 4.16 we show the results of the alignment experiments with these two different magnetic field pulses. We directly plot as a function of time the effective alignment angle of the sample, derived from the reduced linear dichroism through equation 4.22.
The pulse length does not play a significant role on the maximum alignment in particular for the longer tubes. There is no noticeable delay between the field maximum and the alignment maximum for both pulses and for both samples. This suggests that the characteristic alignment time constant is shorter than the rise time of the fast pulse. The maximum value of the effective angle for the $(7,6)$-batch is around

$$\langle \cos^2(\Theta) \rangle \approx 0.9, \tag{4.27}$$

while for the $(6,5)$-batch we have sensibly less alignment, i.e.

$$\langle \cos^2(\Theta) \rangle \approx 0.5. \tag{4.28}$$

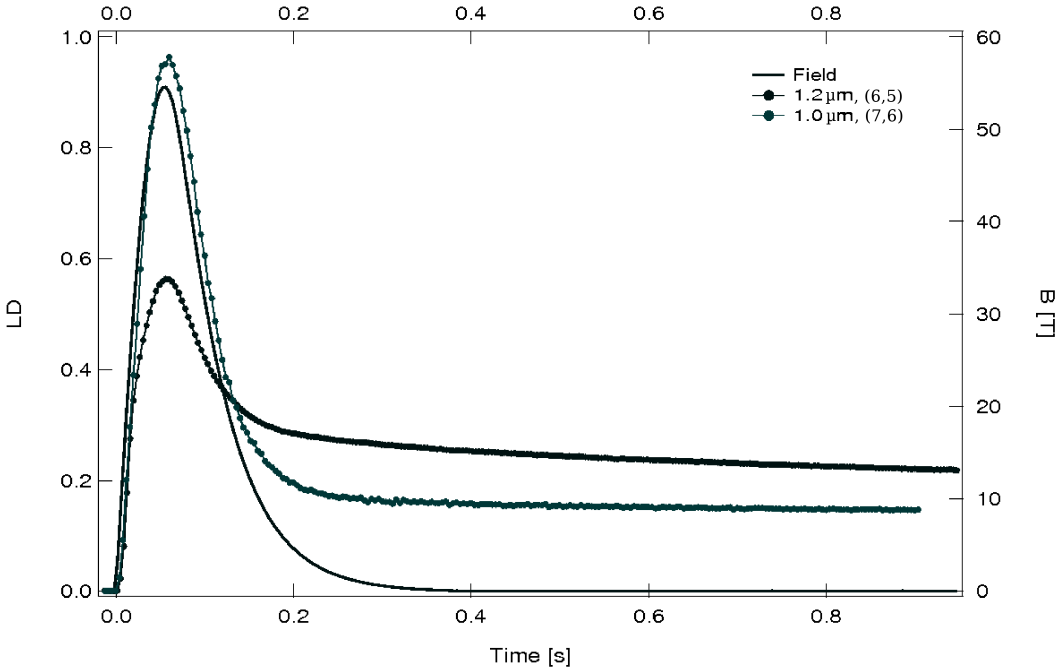

Figure 4.15 *– Linear Dichroism for length sorted 1.0 μm and 1.2 μm samples at room temperature. In particular after the magnetic field the dynamics is different from the tubes studied in the previous section. The tubes remain aligned for a long time even after the pulse. The absolute alignment for both samples seems to be different but from this figure a definite answer to this question can not be given.*

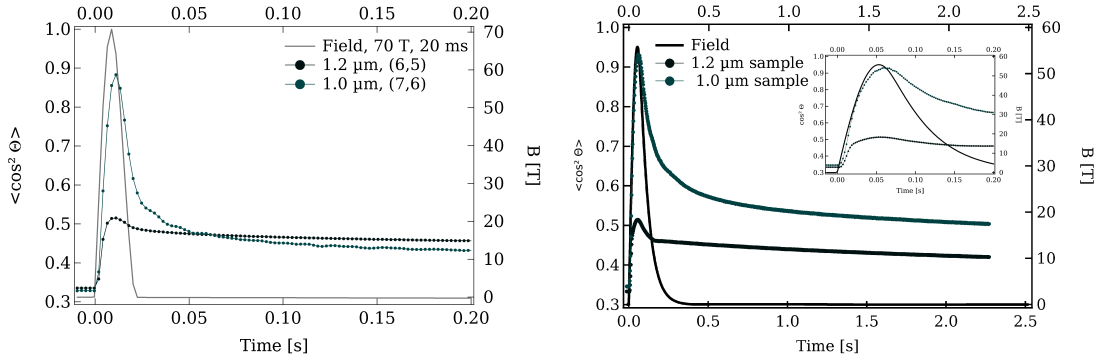

(a) **(b)**

Figure 4.16 *– The effective angle of the tubes in the sample in a (a) short and (b) long pulse for length sorted 1.0 μm and 1.2 μm samples at room temperature. While the short tubes reach almost complete alignment, the long tubes are far away from this point and don't show significant differences between the two pulse forms. In contrast the alignment after the field for the shorter samples is strongly influenced by the pulse form. The inset presents a zoom around the pulse.*

The very slow decay of both samples after the pulse however is puzzling. The value of the effective angle after the magnetic field differs for the two measurements of the $(7, 6)$-batch.

4.2.3 Rotational diffusion

4.2.3.1 Time-dependent external potential

To describe mathematically the alignment process we first apply the theory on rotational diffusion of Doi and Edwards [Doi 1986]. In this model, we consider the nanotube as a rigid rod with the vector $\underline{\mathbf{u}}$ which is parallel to the tube axis. We introduce the rotational operator

$$\mathcal{R} \equiv \underline{\mathbf{u}} \times \frac{\partial}{\partial \underline{\mathbf{u}}} , \tag{4.29}$$

which is the analogy to the gradient operator $\frac{\partial}{\partial R}$ when considering translational diffusion. The orientation of the tubes is described using the probability distribution function of $\underline{\mathbf{u}}$, $\Psi(\underline{\mathbf{u}}, t)$. We can assume that the surrounding liquid does not possess any velocity gradient. Taking into account a hydrodynamical torque on the rod we can write the Smoluchowski equation for rigid rods

$$\frac{\partial \psi}{\partial t} = \frac{k_B T}{\zeta_r} \mathcal{R} \left(\mathcal{R}\Psi + \frac{\Psi}{k_B T} \mathcal{R} U(B) \right) . \tag{4.30}$$

$U(B)$ is the external potential, i.e. the term where we will find the magnetic field. The constant ζ_r is the rotational friction and defines the rotational diffusion constant

$$D_r = \frac{k_B T}{\zeta_r} \tag{4.31}$$

The dimension of this constant is $(\text{time})^{-1}$. Through this definition we finally obtain

$$D_r = \frac{3 k_B T}{\pi \eta l^3 \varepsilon f(\varepsilon)} , \tag{4.32}$$

with

$$f(\varepsilon) = \frac{1 + 0.64\varepsilon}{1 - 1.5\varepsilon} + 1.659\varepsilon^2 \tag{4.33}$$

and

$$\varepsilon = \left(\ln \frac{l}{R} \right)^{-1} . \tag{4.34}$$

Where l is the tube length, η the viscosity of the solution and R is the radius of the tube. Equations 4.33 and 4.34 are factors reflecting the geometry of the

tubes [Parra-Vasquez 2007]. The magnetic field is introduced in the system as an external potential in equation 4.30. It is dependent on the number N of carbon atoms in the tube, which is dependent of the tube length l and of the orientation angle $\Theta(\underline{\mathbf{u}})$.

$$U(B) = -\Delta\chi N(l)B(t)^2\cos^2\left(\Theta(\underline{\mathbf{u}})\right) \tag{4.35}$$

The rotational diffusion differential equation 4.30 can be solved by expanding ψ as a function of spherical harmonics Y_n^m

$$\psi(l,\underline{\mathbf{u}},t) = \sum_{n=0}^{N}\sum_{m=0}^{N} A_n^m(l,t)Y_n^m(\underline{\mathbf{u}}) \qquad n,m \in 2i \text{ with } i \in \mathbb{N}. \tag{4.36}$$

Using Galerkin's method, the partial differential equation is converted into a system of ordinary differential equation. The detailed solution of this procedure can be found in [Parra-Vasquez 2009, Shaver 2008b, Shaver 2009].
The nematic order parameter can thus be expressed as a function of the spherical harmonics coefficient, which are solved for each time step numerically.

$$S(l,t) = 2\sqrt{\frac{\pi}{5}}A_2^0(l,t) \tag{4.37}$$

Note that this model is developed using the dilute regime approximation, which is based on the assumption that the concentration is low enough so that the tubes do not interact with each other.

4.2.3.2 Brownian motion

In absence of magnetic field the orientation of the nanotubes is isotropic or tends toward it. The process which is supposed to create random orientation is Brownian motion. It is the competing force to an external potential which tends to align the tubes. Describing rotational diffusion in absence of an external potential gives

$$\frac{\partial\psi}{\partial t} = \frac{k_B T}{\zeta_r}\mathcal{R}^2\Psi \tag{4.38}$$

We already discussed the analogy between classical diffusion and rotational diffusion. Equation 4.38 illustrates the similarity between both effects.
As for translational diffusion we can solve this equation with an ansatz based on Green's function, $G(\underline{\mathbf{u}},\underline{\mathbf{u}}',t)$. We thus get

$$\frac{\partial}{\partial t}G(\underline{\mathbf{u}},\underline{\mathbf{u}}',t) = D_r\mathcal{R}^2G(\underline{\mathbf{u}},\underline{\mathbf{u}}',t) \tag{4.39}$$

where $\underline{\mathbf{u}}$ is the orientation of the tube at time t and $\underline{\mathbf{u}}$' the orientation at time $t = 0$. The complete solution to solve the differential equation is described in [Doi 1986]. We finally obtain a time-dependent ordinary differential equation of first order for the correlation function $\langle\underline{\mathbf{u}}(t)\cdot\underline{\mathbf{u}}(0)\rangle$

$$\frac{\partial}{\partial t}\langle \underline{\mathbf{u}}(t)\cdot\underline{\mathbf{u}}(0)\rangle = -2D_r\langle \underline{\mathbf{u}}(t)\cdot\underline{\mathbf{u}}(0)\rangle \tag{4.40}$$

With the initial condition at $t = 0$:

$$\langle \underline{\mathbf{u}}(t=0)\cdot\underline{\mathbf{u}}(0)\rangle = 1\,, \tag{4.41}$$

we get for the solution of equation 4.40

$$\langle \underline{\mathbf{u}}(t)\cdot\underline{\mathbf{u}}(0)\rangle = e^{-2D_r t}\,. \tag{4.42}$$

We can transform equation 4.42 in

$$\langle (\underline{\mathbf{u}}(t)-\underline{\mathbf{u}}(0))^2\rangle = 2-2e^{-2D_r t}\,, \tag{4.43}$$

and at the same way one can show that

$$\frac{3}{2}\left((\underline{\mathbf{u}}(t)\cdot\underline{\mathbf{u}}(0))^2-\frac{1}{2}\right) = e^{-6D_r t}\,. \tag{4.44}$$

The latter relation can be directly expressed as a function of the angle Θ between the two orientations using

$$\cos^2(\Theta) = (\underline{\mathbf{u}}(t)\cdot\underline{\mathbf{u}}(0))^2 \tag{4.45}$$

4.2.3.3 Rotational diffusion for poly-disperse length

The model based on rotational diffusion can be used to describe the experimental results of section 4.2.2.1 where the measurements of DNA wrapped HipCo single-walled nanotubes dispersed in 1% ioxidanol are presented. Rheology measurements determined an average tube length of $l = 168$ nm with a standard deviation of $\sigma = 0.8668$.
Figure 4.17 compares the results of the simulation of rotational diffusion and the experimental data for samples with high and low viscosity. The solid red lines show the simulation performed with parameters determined from the rheology measurements. The agreement with the experimental data of the low viscosity samples is rather poor although it reproduces the dynamics qualitatively. We find an important disagreement for the samples mixed with sugar, i.e. the high viscosity samples.
However we can better reproduce the experimental data by modifying the length distribution and increasing the value of the mean length. For the low viscosity samples a length of 700 nm reproduces accurately the experimental data. For the high viscosity samples a good agreement between theory and experiment could be obtained, despite noticeable deviations below 10 Tesla, using a length distribution centred around 1500 nm. Note that this statement in only valid for the field down-sweep. In the up-sweep the shorter mean length distribution better matches the experimental data, as we can also see it in figure 4.17c. The inset in figure 4.17

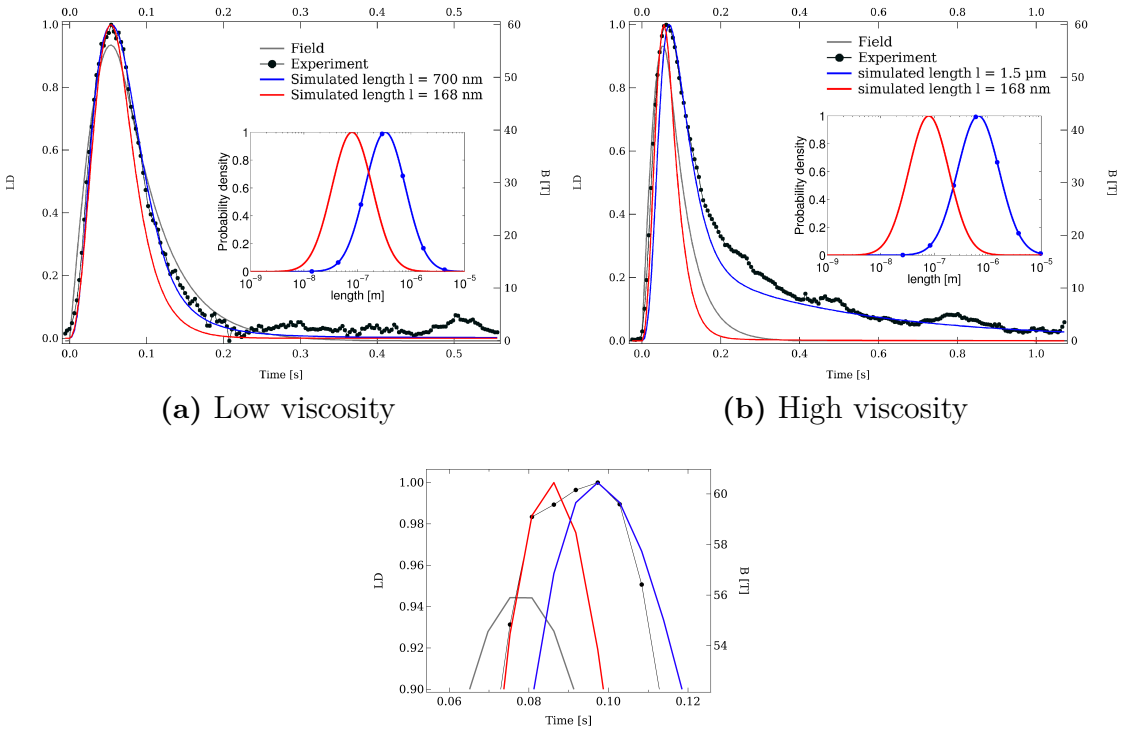

(a) Low viscosity

(b) High viscosity

(c)

Figure 4.17 *– Comparison between experimental data and theory for different length distributions. The inset shows the length distribution used for each simulation. The red solid lines present the values determined from the rheology measurements. The solid blue lines stands for the best match fit. (a) For the low viscosity sample a modified mean length reproduces the experimental data accurately, i.e. 700 nm instead of 168 nm. (b) A mean tube length of 1.5 μm matches the down sweep but still fails for the up sweep of the magnetic field. (c) Zoom of the maximum LD of figure 4.17b.*

shows a comparison of both length distribution used for the respective simulations. Although we are able to reproduce the experimental data using the model based on rotational diffusion, we find strong disagreement between the length distribution which fits the experimental data and the distribution which is determined using different characterisation methods. Moreover there is no physical argument to justify this difference. An attempt to explain this discrepancy is to consider the formation of tube bundles in the solution, which arrange to a tube with an effective length longer than the initial one. The characterisation of the samples however shows that the majority of SWNT are individually suspended and the remaining bundles contain mostly two tubes[2]. The results are confirmed by AFM measurements which give a slightly higher mean value for the tube length but it still can not explain the observed difference.
Reasonable agreement between the calculation and the experimental data is ob-

[2]Private communication, A.N.G.Parra-Vasquez

tained by maintaining the length distribution and magnetic anisotropy as determined independently within their experimental error bars and by increasing the viscosity. The results are shown in the figure 4.18. The inset of figure 4.18a shows the length distribution used for the simulations. It is very close to the distribution measured using the rheology method. The agreement is obtained for the dilute sample 4.18a with a viscosity of $\eta = 0.004$ Pa·s, i.e. 3 times higher than the rheological value. A slight mismatch is only found in the field up-sweep, while the small deviation around 0.2 s is probably induced by the movements of the magnet at the end of the pulse. The results suggest that the alignment dynamics of SWNT is not determined by the *bulk* viscosity of the solution. This may be due to specific interactions of the SWNT or their surfactants with the solvent. However the agreement between experiment and theory only holds for the samples with low viscosity as it is presented in figure 4.18b. Further speculations are thus not allowed.

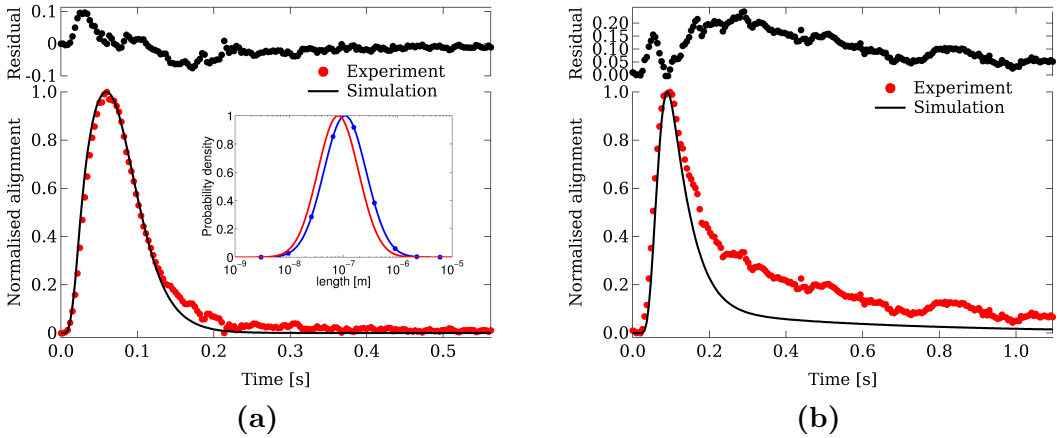

Figure 4.18 *– (a) Alignment experiment (red circles) and simulation (black solid line) at 280 K for a sample with low viscosity. The length distribution has a mean value of 240 nm and a standard deviation of 0.9 (blue solid line) and is presented in the inset. This mean value is within the error bars of the characterisation process. The magnetic anisotropy used was $\Delta\chi = 2.0$ emu/mol. For comparison we plot the length distribution obtained by the rheology measurements (red solid line). (b) The simulation repeated for the high viscosity samples. The values were kept constant except the viscosity. The simulation does not match the experimental data.*

A last possibility which might explain the disagreement between the length distribution which fits the data and which was determined by rheology measurements is to consider that the fit reflects the real length distribution of the sample, i.e. the measured volume fraction is not representative for the whole batch. As a matter of fact we only measure a small volume of the whole prepared batch whose length distribution can differ from the whole solution. The determination of the length distribution with the AFM technique, where also a small part of the prepared solution is selected to determine the length distribution, can yield very different mean values for different samples from the same batch [Parra-Vasquez 2007].

The interpretation of poly-disperse length data remain puzzling. However the present data do not allow further interpretations as there remain a considerable amount of unknown parameters. Further experiments were not possible as the samples are showing clear evidence of ageing and dried out.

4.2.3.4 Rotational diffusion for length sorted samples

The rotational diffusion simulations can not describe for the experimental results of the length sorted samples presented in section 4.2.2.2. Although one could assume that a mono-disperse system should be easier to analyse, the present experimental data are at least as puzzling as the previous ones.
To check on which points the model fails, we can now verify the value of the rotational diffusion constant. With single tube lengths we can obtain the experimental value of D_r by fitting the disalignment decay after the magnetic field pulse using equation 4.44. One can compare the results of the calculated constant and the fit. The values for the rotational diffusion constant are expect to be 30.36 s^{-1} and 49.62 s^{-1} at 295 K for the 1.2 μm sample and the 1 μm sample respectively. However the experimental data after the magnetic field fit only very poorly to a single exponential decay.
This is shown in figure 4.19a. We fit the relaxation of a slightly dilute sample with a single exponential, which lead to a value of 0.044 s^{-1} for the rotational diffusion constant. We now insert both values, the fitted and the expected value for D_r, into the simulation. The long disalignment, i.e. a small value of D_r, should necessarily be accompanied by a delay between the magnetic field maximum and the maximum alignment. On the other hand, the simulation with the higher value of the rotational diffusion constant is following the field pulse on the up- and down-sweep. Both features are not observed in the present experimental data. We will also see later that the decay is better reproduced by a double exponential decay.
The observed temporal behaviour of the alignment proves that the picture of non-interacting particles in the sample is not correct. Indeed one can quickly measure the concentration of nanotubes in the samples using absorption spectroscopy and the *Beer-Lambert* law, where the absorption is related to the concentration, c, the thickness, d, of the sample, and a material parameter, ε, by a linear relationship [Beer 1852]:

$$A = \varepsilon \cdot c \cdot d \,. \tag{4.46}$$

In figure 4.19b we show the case where the sample batch is mixed with its reference liquid. The aim is to decrease the SWNT concentration and try to enter the dilute regime. This limit is proportional to the length of the tubes and can be expressed in SWNT concentration [Duggal 2006]. The dilute regime is valid for overlap concentrations below $\frac{1}{\langle L^3 \rangle}$. Expressing this limit in nanotube concentrations we find the quantities summarised in table 4.1.
When we measure the concentration of both samples, using the work of [Jeong 2007] as reference for the material parameter ε, even for our very dilute samples, the

concentration of nanotubes in the solution is above the limits computed in table 4.1 and we are not in the dilute regime.

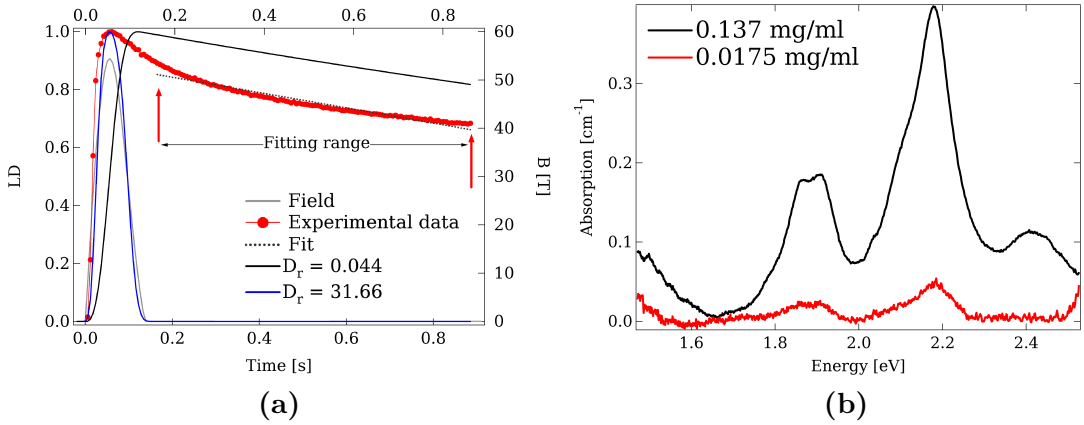

Figure 4.19 *– (a) Simulations performed with the theoretical computed rotational diffusion constant in the dilute regime and the fitted parameter from the experimental data (solid blue and black lines respectively). Both simulations do not match the result of the experiment. The sample here is from the (6,5) batch (red markers and line) and the fit is the dashed dark grey line. (b) Absorption measurement to determine the concentration of a nanotube sample using Beer-Lambert's law.*

Table 4.1 *– Limit of dilute regime for present samples*

Tube length [μm]	concentration [mg/ml]
1.0	$4.5 \cdot 10^{-4}$
1.2	$2.6 \cdot 10^{-4}$

In the semi-dilute regime the tubes can still move freely but in contrast to the dilute regime their movements are hindered by entanglement with other tubes. *Pecora* [Pecora 1985] extended the theory of *Doi* and *Edwards* to the semi-dilute regime. It consists of defining an angle of free rotation $\frac{a}{l}$ where a is the distance between nearest neighbour. The rotational diffusion constant is then

$$D_r = \frac{a^2}{l^2} D_r^0 \tag{4.47}$$

where D_r^0 is the rotational diffusion constant in the dilute regime defined in equation 4.32. From topological arguments one can estimate the parameter a [Pecora 1985]

$$a \approx \frac{1}{cl^2} \tag{4.48}$$

Where c is the concentration of the solution. Finally we get a new dependence for the rotational diffusion constant with

$$D_r = \beta \frac{D_r^0}{c^2 l^6} \tag{4.49}$$

where β is a dimensionless numerical factor.
Equation 4.49 predicts a dramatic slowing of the rotational diffusion. Remember in the dilute regime we have $D_r^0 \propto l^{-3}$ while now the relation is $D_r \propto l^{-9}$. This is the only modification one has to take into account when expressing rotational diffusion in the semi-dilute regime. It however preserves a single exponential decay in the disalignment dynamics. The rotational diffusion in the semi-dilute regime will thus not reproduce the experimental data.
Looking at figure 4.20a we see that it is necessary to introduce other parameters to describe the process. There we plot the order parameter S of both samples directly as a function of the magnetic field. We get the typical hysteresis in alignment we already know from the work of e.g. [Shaver 2009], where the lower branch corresponds to the field up-sweep and the upper branch to the down-sweep. We can distinguish a feature which has not been observed in this kind of experiment before. In the up-sweep we can identify a slope change, marked by arrows in figure 4.20a around 30 and 40 Tesla for both samples studied.
It is known that an external magnetic field can induce a nematic orientational order from a zero field state where it does not exist [Helfrich 1970], in particular when the molecules have a high aspect ratio [Onsager 1949]. A well known system which can be approximated by rigid rods and shows this kind of effect is the *tobacco mosaic virus* [Fraden 1993]. Recent investigations demonstrated this transition on bent-core liquid crystals at fields above 20 Tesla [Ostapenko 2008]. When a liquid crystal is in its nematic phase, the order parameter is only weakly affected by the external field due to the saturation of alignment. This effect could explain the feature observed in figures 4.20a and 4.20c. After the change of slope marked by arrows, the field dependence of the order parameter is decreased. The effect is less obvious in the (7,6)-batch sample, probably due to its lower SWNT concentration, but shows the same trends as the (6,5)-batch sample. Unfortunately we only have two samples with different length and we thus can not identify if this effect is related to the tube length. For comparison we add a calculated curve of the up-sweep where we can not detect any significant change in slope. This curve also exhibits a B^2-behaviour as expected.
In addition, the external field can alter the nematic-isotropic transition temperature [Lelidis 1993] as well as the critical end point [Ostapenko 2008]. The effect of temperature in our data is demonstrated in figure 4.20c, even though it remains small. The temperature seems to shift the position of the supposed transition but the lack of experimental points in the field up-sweep do not allow further conclusions.
If there is a magnetic field induced phase transition we would expect to see it in the down-sweep too. However if the sweep time of the field is much higher than the orientational time of the molecule, the transition can be prevent [Fraden 1993]. In fact the relaxation of the nanotubes in the down sweep is much lower than the

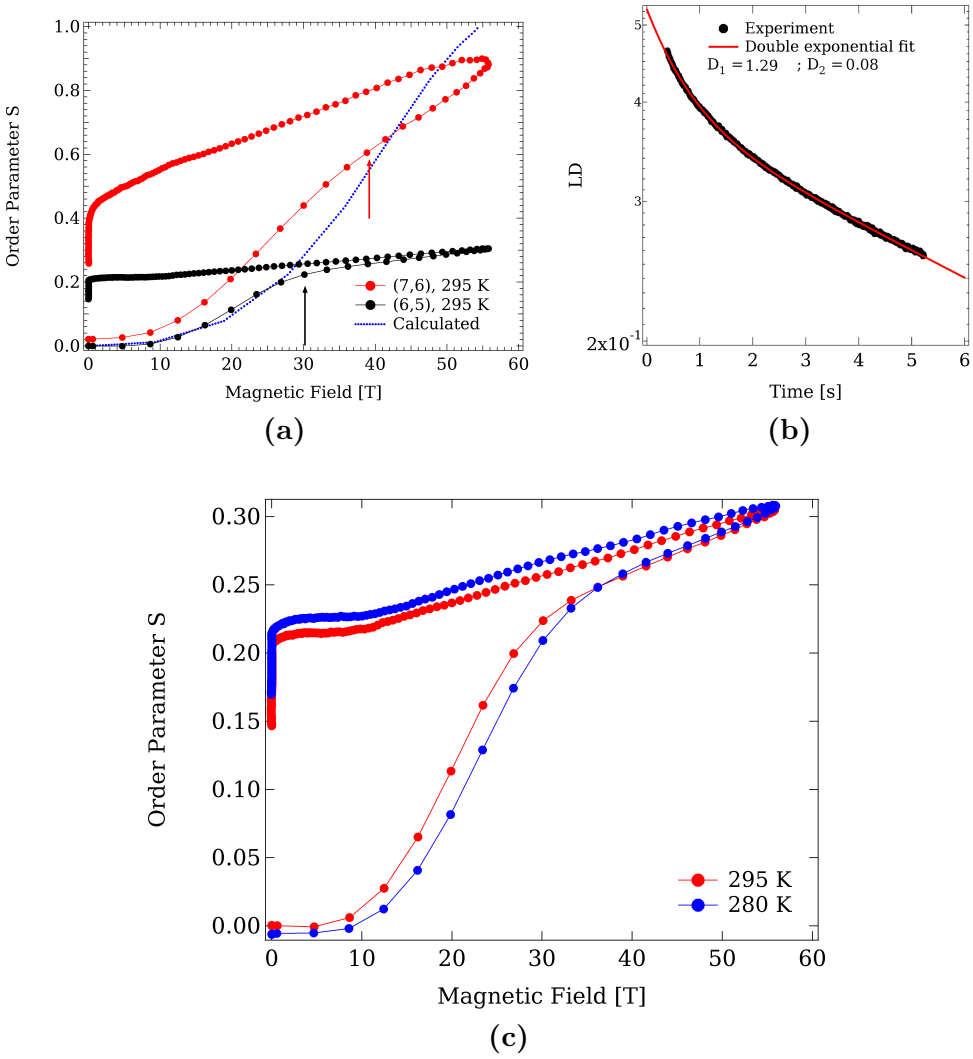

Figure 4.20 – *(a) The order parameter as a function of the magnetic field. The lower branch is the field up-sweep. We indicate with arrows the positions where we identify a change in the slope. The effect is less pronounced for the (7,6)-batch sample but shows the same overall trends as the $(6,5)$-batch. (b) Decay of the experimental data in a logarithmic scale. A double exponential function $(A_1 exp(-D_1 t) + A_2 exp(-D_2 t))$ the data very well and thus at least two dynamics are necessary to describe the process. (c) In this figure we show the influence of temperature for the (6,5)-batch sample.*

decay time of the magnetic field. We can however detect some kinks in the down-sweep at approximately the same value of the order parameter where we identify the slope change in the up-sweep.

In figure 4.21 we compare the order parameter as a function of the square of the magnetic field for different concentrations in the field up-sweep. For decreasing concentration the saturation of alignment occurs at higher fields. At the same time,

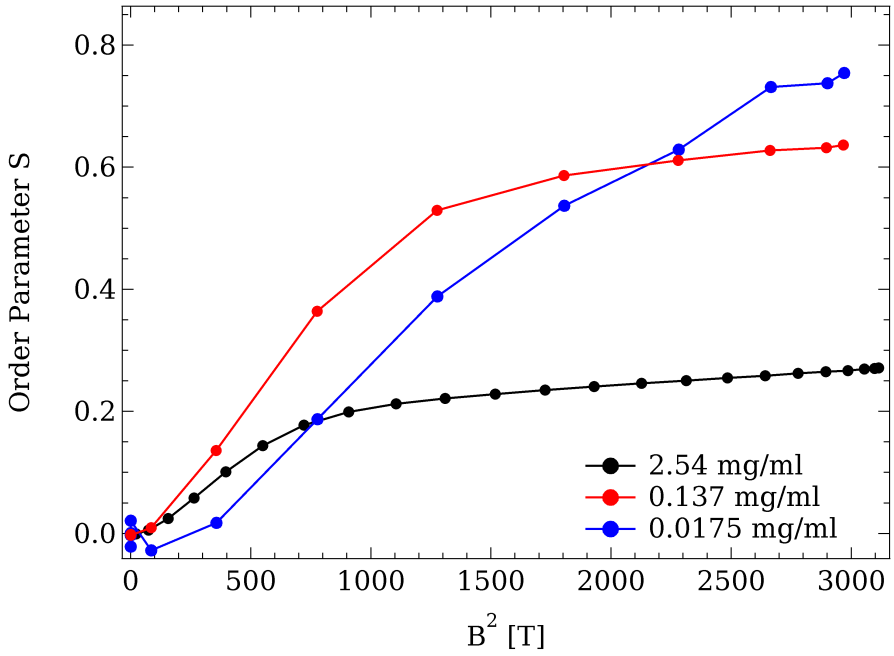

Figure 4.21 *– The order parameter as a function of the square of the magnetic field in the field up-sweep for different concentrations. In the beginning the order parameter in proportional to B^2. The field at which saturation occurs is concentration dependent as the amount of alignment in the samples, expressed by the order parameter S.*

the value of the order parameter at saturation increases with decreasing concentration which is consistent with the previous observation but also shows that the saturation is depending on the concentration. This suggests that the alignment is not homogeneous in the sample.
The decay after the magnetic field fits much better to a double exponential decay, i.e.

$$f(t) = A_1 \exp(-D_1 t) + A_2 \exp(-D_2 t), \tag{4.50}$$

as it is presented in figure 4.20b. We can extract two time constants for the decay dynamics (D_i). There is a factor greater than ten between both values. This suggests that the decay has to be described by two different dynamics. The observation of two decay times was also reported by [Ouano 1980] or [Leezenberg 1996] on different systems where the interaction of the investigated molecule with its solvent is strong.
Two models are used to describe the apparition of different relaxation times. The *diffusion in two environments*-theory (DITE) [Shears 1973] envisions the existence of two environments. In one environment the nanotube can rotate freely in a cage, with small interaction with the molecules building this cage. This cage is characterised by the free volume available, referring to the theory of *Cohen* and *Turnbull* [Cohen 1959]. In the other environment the rotational motion is hindered by

the matrix and motion is only possible in a cooperative process. A second theory, the *restricted rotational diffusion*-theory (RRD) [Warchol 1978] defines two types of motion, one fast and one slow motion. The fast relaxation arises from rotation restricted to a cone. The segments building the border of the cavity are supposed to be immobile, relative to the motion of the tube. The slow relaxation time is due to cooperative motion of the tubes with the boundary of the cone cavity. However the simple determination of the order parameter do not allow more detailed conclusions because, as it was already pointed out, this measurement is only an average over all orientation angles of molecules in the samples.

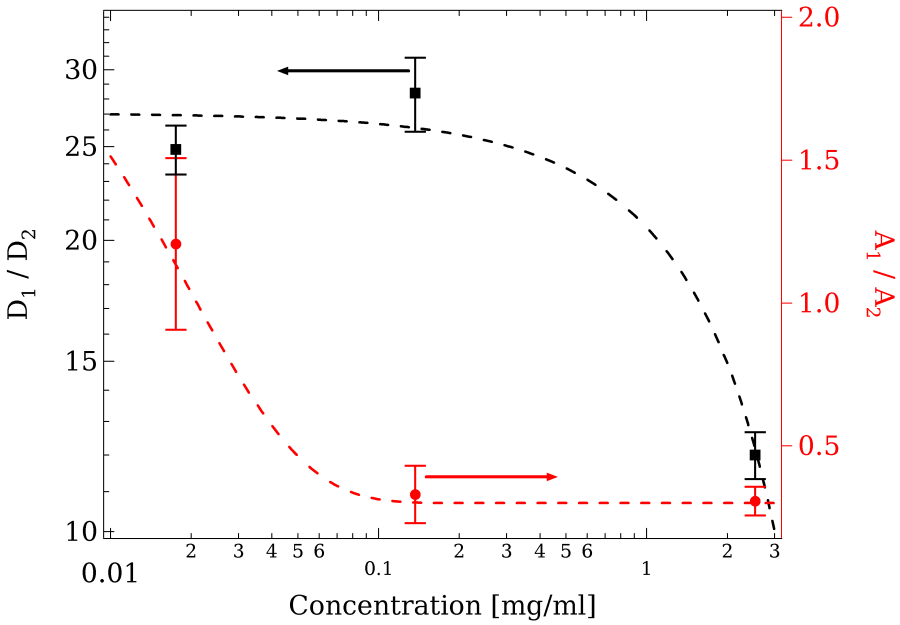

Figure 4.22 *– Ratio of the fitted relaxation times in double exponential decay as a function of concentration on the left axis (black squares). D_1 is the fast relaxation and D_2 the slow relaxation (Compare with figure 4.20b). On the right axis the ratio of the fitting factors A_i are presented (red circles). The dashed lines are guiding lines.*

However we can take into account a last consideration. In figure 4.22 we plot the ratio of the fast and the slow decay times, fitted with a double exponential, as a function of the sample's concentration. The ratio is increasing with decreasing concentration. This fact is consistent with the scenarios described above. While at high concentration less free space is available, the decay is more dominated by cooperative processes and the ratio of the relaxation times decreases.
At low concentrations cooperative processes becomes less important. Thus the relaxation time of individual tubes is dominating the decay. Approaching the semi-dilute to dilute regime limit, the diffusion constant becomes independent of the concentration. The fitted decay should again agree with the values one can deduce from equations 4.32 or 4.49 because $D_{\text{fast}} \gg D_{\text{slow}}$.
This interpretation is also consistent with the concentration dependence of the ratio

of the fitting factors A_i added on the right axis of figure 4.22. This fitting parameter can be interpreted as a weighting of each contribution in the sum of two exponential functions. As the concentration increases the ratio decreases, which is tantamount to a more important contribution of cooperative motion in the sample. In contrast to that findings, at low concentration the factor of the fast decay prevails and cooperative motion can be neglected, in agreement with the definition of the dilute regime approximation.

4.3 Summary

We discussed in this section the magnetic brightening of dark excitons in a magnetic field. We utilised highly aligned samples to demonstrate conclusively that a parallel, tube-threading magnetic field is the dominant source of changes in spectral energy and intensity at high values of the magnetic field. We also determined the splitting between dark and bright bands of $(6, 5)$ SWNTs in our sample by fitting the experimental data to a model based on exchange-split bright and dark exciton bands with Aharonov-Bohm-phase-dependent energies, masses, and oscillator strengths.
In the second part of the chapter we discuss the alignment dynamics of SWNT in solution in a pulsed magnetic field using linear dichroism and a model based on rotational diffusion. Through the analysis of characterised poly-disperse samples suggest that the investigated part of the solution is not representative enough. However the interpretation of this results remain difficult due to the poly-dispersed length. We also investigate length sorted samples which show an unexpected long decay after the pulse. This behaviour can not be reproduced by current theoretical models. A qualitative analysis suggests to take into account different dynamics in the alignment decay. A field induced isotropic to nematic liquid phase transition can be the source of this peculiar behaviour but has to be confirmed by further investigations.

Chapter 5

From graphene to graphite

Contents

Graphite is named from the Greek word *graphein* which means to write or to draw. The etymology illustrates directly the historical main utility of this material. It is a layered compound completely composed of the carbon atoms. The in-plane chemical bonds between carbon atoms are very strong, in contrast to the inter-layer coupling which is rather weak. Thus it is quite simple to detach some layers from a bulk of graphite as it happens every day with our pencils. Nevertheless the first report of experimental preparation of a mono-layer graphite is only found in 2004 [Novoselov 2004b]. Since this work, graphene has been investigated with great interest and new production methods are rapidly developed since graphene is expected to have great potential for technological application [Berger 2004, Geim 2007a]. The discovery of graphene was awarded in 2010 with the Nobel prize. The rise of graphene also renewed the interest in the properties of graphite which is obviously easier to handle experimentally than the one atom thick graphene. However, as graphite is a more complex system, its electronic properties are not yet fully understood.
In this chapter we will discuss the experimental results obtained in magneto-transmission measurements on epitaxial grown graphene and thin graphite.

5.1 Magneto-optical spectroscopy of graphene

5.1.1 Multilayer Graphene

Let us now start from the brief description of the samples used in this experiments. It consists of multi-layer graphene grown on SiC. Such systems are obtained by heating a SiC crystal. As described in detail by Berger *et al.* [Berger 2004] the silicon will desorb from the top layers and there remain thin graphitised layers which quantity can be controlled by temperature and heating time.
Graphene can be obtained both from the carbon and the silicon-terminated surface of SiC, however with important differences in the quality of the sample. The silicon face produces few layers or monolayers but with low mobility, whereas the carbon face produces several layers but with higher mobility [Hass 2006]. It was also demonstrated that the first layers of graphene next to the substrate are highly influenced by and bonded to the substrate [Varchon 2007].
Despite the multi-layer character and the presence of the mentioned doped first layer, epitaxial graphene exhibit the same features as exfoliated graphene, i.e. Shubnikov-De Haas oscillations with a Berry phase shift of π, which is the same phase shift as for Dirac fermions [Berger 2006]. Raman spectroscopy studies revealed that the layers are electronically decoupled from each other and thus can be considered as graphene [Faugeras 2008]. Angle-resolved photo-emission experiments confirmed the linear dispersion relation which is familiar from mono-layer graphene [Bostwick 2007]. Infrared spectroscopy measurements at low magnetic fields also showed the expected transitions for Dirac fermions between Landau levels [Sadowski 2006].
The samples for the present work were grown on the carbon face of SiC. The number of layers is estimated to be around 90[1]. Note that the first few layers adjacent to the substrate are supposed to be highly doped while the other layers are undoped. In a transmission measurement we should expect to measure the contribution of all layers. The large majority of them is undoped and we can thus assume to deal with an undoped sample as it was shown in [Orlita 2008b].

5.1.2 Magneto-transmission of epitaxial graphene

5.1.2.1 Magnetic field dependence

First experiments were performed measuring the transmission through a sample with epitaxial growth graphene. The sample was placed in Faraday configuration and the field applied perpendicular to the graphene planes. The experimental setup was described in detail in chapter 3. Figure 5.1 shows typical transmission spectra of a sample in magnetic fields between 30 and 59 Tesla. The spectra were obtained without any polarisation.
Since the absorption lines in this energy regions are weak, we normalised all spectra

[1] Private communication of P.Plochocka

by the zero-field transmission. We observe distinct absorption peaks in the spectra, which can be selected and assigned to a value of the magnetic field. Some selected transitions are denoted by markers in figure 5.1. These are the transitions between Landau levels obeying the selection rules developed in section 2.4.3. Some spectra however seem to be richer than one would expect from simple single layer graphene. We will discuss this issue later and focus here only on the lines we can assign to transition of mono-layer graphene as the most distinguished ones.

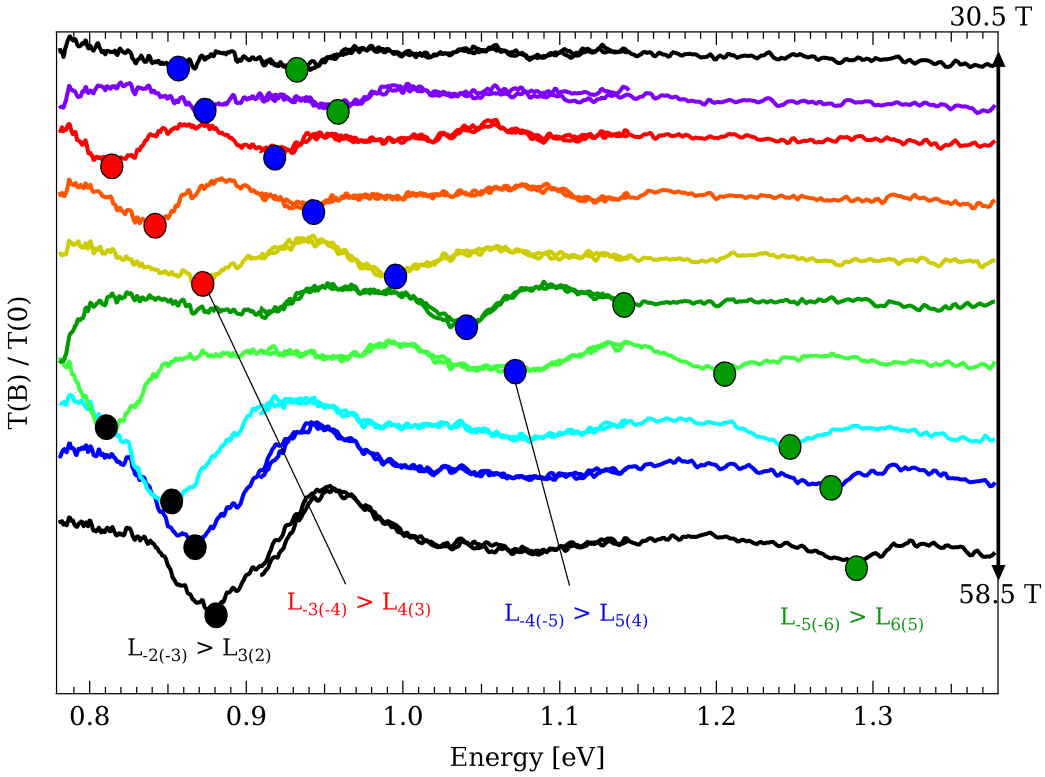

Figure 5.1 *– Typical transmission cascade plot through a sample of epitaxially grown graphene on SiC at high magnetic fields and 4.2 K. All spectra are normalised by the zero-field transmission and offset for clarity. The transmission peaks correspond to transitions between Landau levels. Each peak position can now be assigned to the corresponding magnetic field value as it is shown in the figure, where we marked some transitions (coloured circle points).*

We can now plot the position of the absorption lines we identify in all spectra against the magnetic field, as presented in figure 5.2. We add to our data the results of the work by Sadowski *et al.* [Sadowski 2007] and by Plochocka *et al.* [Plochocka 2008] to give a complete overview of the Landau level transitions in multi-layer graphene from 0 to 60 Tesla in the available spectral energy range. The x-axis is scaled as $\sqrt{B}$. The experimental points are well described by a straight line and we can conclude that they exhibit a clear $\sqrt{B}$-dependence which is the signature of massless relativistic particles as it was shown in equation 2.31. This observation agrees with the report of Sadowski *et al.* [Sadowski 2007]. This is an additional proof that multi-layer graphene hosts the presence of massless relativistic particles

and can be considered as graphene. In figure 5.2 we use only one fitting parameter for all transitions, which is the Fermi velocity, v_F.
The value of Fermi-velocity employed was $v_F = 1.03 \cdot 10^6\ m/s$, in agreement with previously reported values [Plochocka 2008].

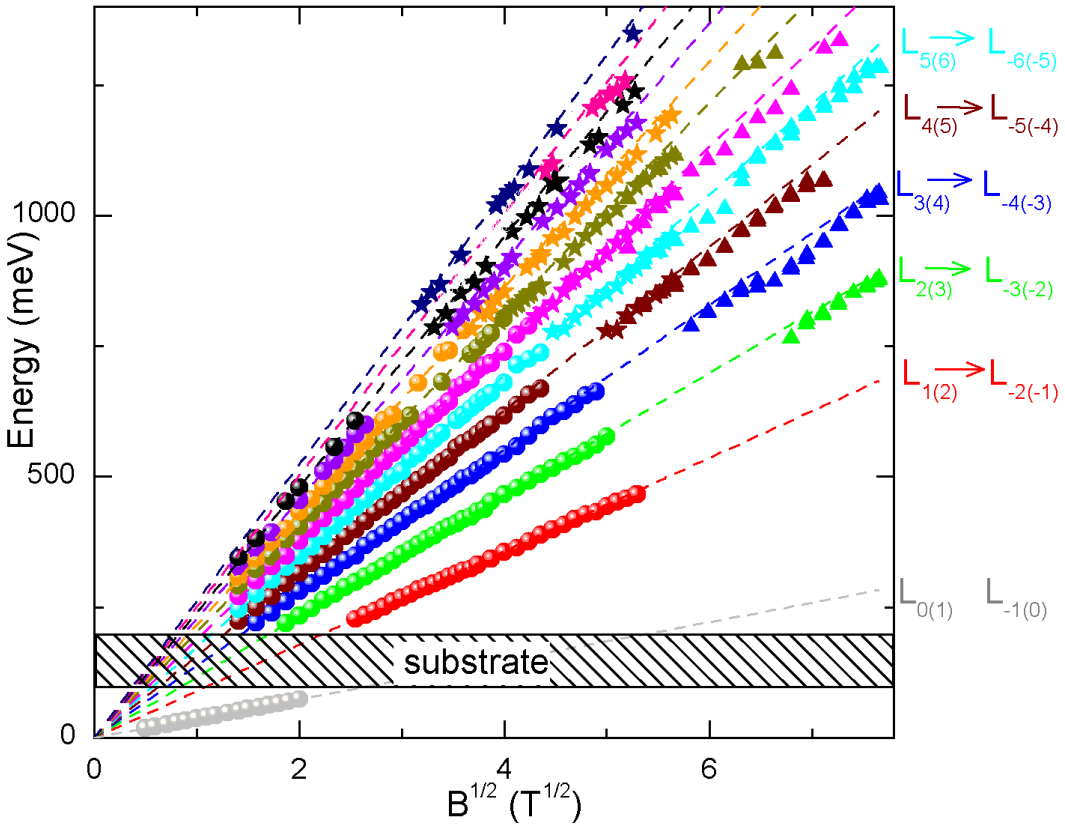

Figure 5.2 *– Landau level fan-chart for graphene. Each peak position identified in the spectra is plotted against the corresponding magnetic field. The Landau levels are following the $\sqrt{B}$ dependence which is the signature of massless Dirac fermions. Filled triangles are the data obtained with pulsed magnetic fields up to 60 Tesla from the actual work. The coloured stars are the results from magneto-transmission experiments up to 34 T [Plochocka 2008] and the circles results from the first FIR spectroscopy measurements [Sadowski 2007]. The dashed lines presents the theoretical transitions.*

We will now focus on the high field and, more important, on the high energy part of figure 5.2. Looking at these data we find that all experimental transitions are slightly below the theoretical expectation which however match the experimental points at low magnetic fields and energy. This effect is getting stronger with increasing energy.
A more rigorous treatment of graphene in the presence of higher order interactions shows that the band structures have to be corrected by next-nearest-neighbour in-

teractions, t'. The strength of the next-nearest-neighbour interaction was estimated with respect to the nearest neighbour hopping, t, $\frac{t'}{t} \approx 0.1$. This leads to a modified energy dispersion relation of Landau levels and is written [Plochocka 2008]

$$\varepsilon_{\sigma,n} = \hbar\omega_c^g \frac{3t'}{\sqrt{2}t}\frac{a}{l_B}n + \sigma\hbar\omega_c^g\sqrt{n}\left(1 - \frac{3w^2}{8}\left(\frac{a}{l_B}\right)^2(n + \mathcal{O}(n^0))\right) \tag{5.1}$$

The conduction and valence bands are denoted by $\sigma = +$ and $\sigma = -$ respectively. w is a fitting parameter and determined to be about 2.8. Note that taking into account next-nearest neighbour interactions has two consequences for the dispersion of graphene. The more dominant effect is the deformation of the band, the effect of trigonal warping. It scales strongly with energy. The second effect is the emergence of an asymmetry between electrons and holes.
With our experimental techniques we observe the transition between Landau levels $-n \to n+1$, denoted $+$, or $-(n+1) \to n$, denoted $-$. The transition energy has therefore additional contributions, given by

$$\Delta E^{\pm} = \mp\frac{9t'}{2}\left(\frac{a}{l_B}\right)^2 + \frac{3a^2w^2}{64\hbar^2 v_F}\left(\hbar\omega_c^g\left(\sqrt{n+1} + \sqrt{n}\right)\right) \tag{5.2}$$

In this equation we can clearly identify both contributions of the next-nearest neighbour corrections. The first term is the electron-hole asymmetry and will be discussed later. The second term is the effect of trigonal warping. Figure 5.3 is comparing the deviation from the $\sqrt{B}$-dependence of the theoretical model and the experimental data as a function of energy. We thus build the difference of the experimental data with the perfect $\sqrt{B}$-dependence.
The solid black line in figure 5.3 is the result of the theoretical model in absence of asymmetry, where we have chosen the same parameter $w = 2.8$ as in [Plochocka 2008]. We can see that this value of the fitting parameter describes our new high field data quite well and the deviation is indeed dependent of energy as it is expected for trigonal warping. We additionally plot the full description including the electron-hole asymmetry in this figure. We clearly see that the additional asymmetry contribution is very small with respect to the trigonal warping and to the experimental resolution and can be neglected in this description. With this model we can explain the small deviation from the $\sqrt{B}$-prediction we observe at high energies.

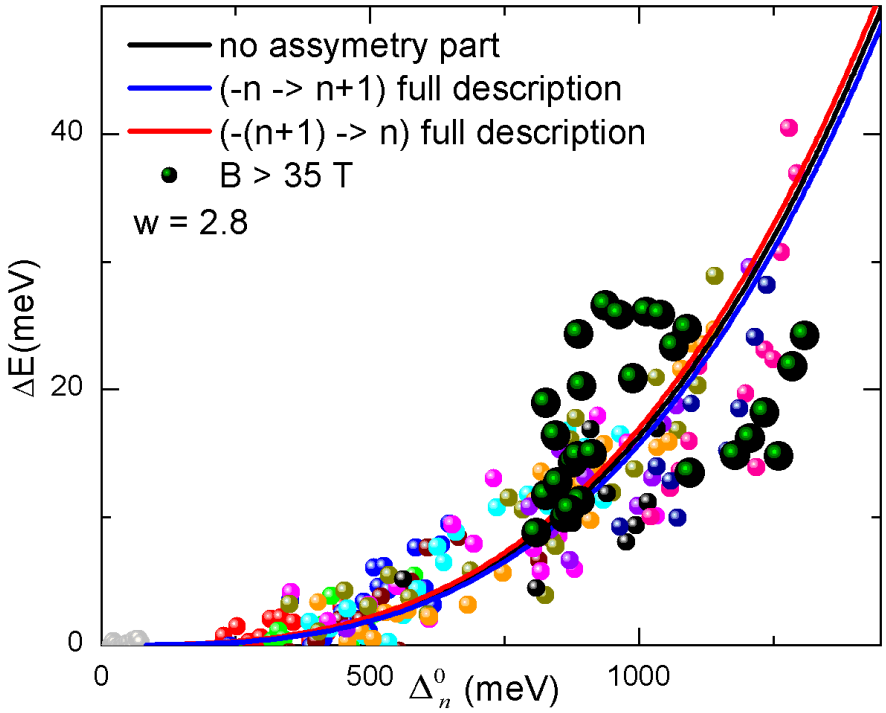

Figure 5.3 *– Deviation from the $\sqrt{B}$-dependence of the experimental points as a function of transition energies, i.e. $\Delta_n^0 = \hbar\omega_c^g\left(\sqrt{n+1}+\sqrt{n}\right)$. Small coloured circles are the experimental points obtained in [Plochocka 2008]. The black/green circles are the experimental points from the present work. The black line is the theoretical expectation with the fitting parameter $w = 2.8$. The agreement with the previous report is very good. Red and blue solid lines are the full description of equation 5.2 in presence of weak electron-hole asymmetry.*

5.1.2.2 Electron-electron interactions in graphene

Recent reports investigate the cyclotron resonance of graphene and bi-layer graphene on SiO_2 substrates in terms of many body interactions [Jiang 2007]. The work interprets the observed blue-shift from the $\sqrt{B}$-law on one Landau level as the signature of electron-electron interactions. This observation is a violation of Kohn's theorem [Shizuya 2010].

This theorem states that many-body interactions, like electron-electron interaction, do not affect the cyclotron resonance [Kohn 1961]. The main argument of Kohn's theorem says that the cyclotron resonance only sees the centre of mass motion, in which the internal force of the electron-electron interaction has no effect. However the theorem holds for electrons moving in a perfect translational symmetric potential and impurities or non-parabolicity can make electron-electron interactions visible in cyclotron resonance measurements.

Recent theoretical investigations showed when electron-electron interactions are taken into account one should expect a blue shift of the energy for inter-band transition with respect to the perfect $\sqrt{B}$-dependence due to the renormalisation of the

cyclotron frequency ω_c [Shizuya 2010]. It can explain the experimental observations made by Jiang *et al.* in [Jiang 2007].
In equation 2.38 we saw that the Landau levels, n, in graphene scale proportional to

$$sgn(-(n+1))\sqrt{|n|+1} - sgn(n)\sqrt{|n|}. \tag{5.3}$$

We can use this relation and normalise the observed high field transitions shown in figure 5.2 by their respective slopes. We expect to find all points on the same line after this treatment. We plot the corresponding experimental points in figure 5.4 as a function of $\sqrt{B}$.

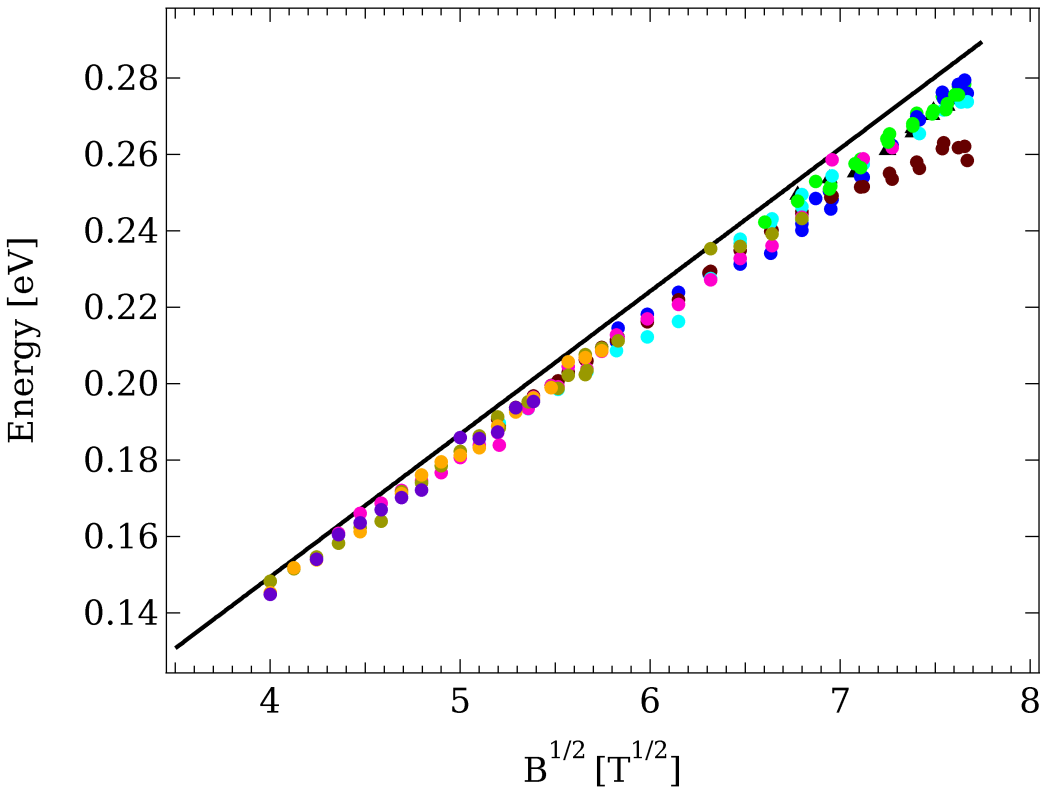

Figure 5.4 *– Theoretical (solid red) and experimental (filled circles) transitions from figure 5.2 normalised by their respective slopes. The colour code of figure 5.2 for the transitions is preserved. The Fermi-velocity was fixed at $v_F = 1.03 \cdot 10^6 m/s$ to trace the theoretical expectation. We can only observe a slight red shift of the experimental points at higher energies which is in excellent agreement with the next-nearest-neighbour model of Plochocka et al. as discussed in section 5.1.2.1. We can conclude that we do not observe electron-electron interaction induced shift in multi-layer graphene on SiC.*

The observation we make is in contrary to the experimental findings reported by Jiang *et al.*. The only distinguishable feature we can observe in figure 5.4 is a slight red shift of the experimental points with respect to the $\sqrt{B}$-behaviour. However

this effect is already explained in previous section as due to trigonal warping.
At low fields Orlita *et al.* also reported that in multilayer graphene on SiC no deviations of the cyclotron resonance are found due to many body effects [Orlita 2008b]. The difference between the experimental observations of graphene on SiO_2 and SiC is probably due to the role of the substrate. The mentioned work [Jiang 2007], where the experimental findings were interpreted as a signature of electron-electron interactions, used exfoliated graphene on SiO_2 substrates. The dielectric constant of SiC is higher than in SiO_2 ($\varepsilon_{SiC} \approx 10$ [Patrick 1970] and $\varepsilon_{SiO_2} = 3.9$). Thus the screening between the carriers is enhanced which reduces electron-electron interactions in multi-layer graphene on SiC.

5.1.2.3 Polarisation resolved spectra

We additionally performed polarisation resolved experiments on graphene with the setup described in chapter 3. In figure 5.5 we show six selected spectra at different magnetic field strengths. We directly compare the σ_+- and the σ_--spectra with each other by putting them in the same figures. The sign of polarisation was arbitrarily assigned because the direction of polarisation was not determined.

In figure 5.5 we observe the same peaks as in figure 5.1. As mentioned above the spectra are richer than simple mono-layer graphene. Note that all measurements were performed on two samples and the observation are reproducible whenever the features are more pronounced in these spectra.
Note the transmission signals of figure 5.5 in both polarisations are greater than unity at different energies. This means that the transmission of the sample is higher than at zero magnetic field. The simplest way to explain this effect is to invoke optical sum rules. The integrated spectrum over the whole spectral range has to be constant and thus each absorption dip has to be compensated in the spectrum [Smith 1976]. Graphene is also expected to show a very large Faraday rotation [Crassee 2010]. This has an important impact on the refractive index and thereby on the reflection and transmission coefficients. Values above unity for $T(B)/T(0)$ are also observed in [Crassee 2010].
Let us now note several differences in each picture displayed in figure 5.5. A common feature of all pictures is the higher oscillator strength for the spectra assigned with σ_+ in particular at high magnetic field and for the $L_{-2(-3)} \rightarrow L_{3(2)}$ transition. Other peaks at various field strengths are showing clear polarisation dependence e.g. vanishing for opposite polarisation.
Note that a polarisation dependence is not expected when considering a perfect linear dispersion relation, i.e. only taking into account the presence of nearest-neighbour hopping and for undoped graphene.
If we take the difference between the energy we expect for the $-n \rightarrow (n+1)$ and the $-(n+1) \rightarrow n$ transitions following the model described in equation 5.2 we get a non-zero term which is written

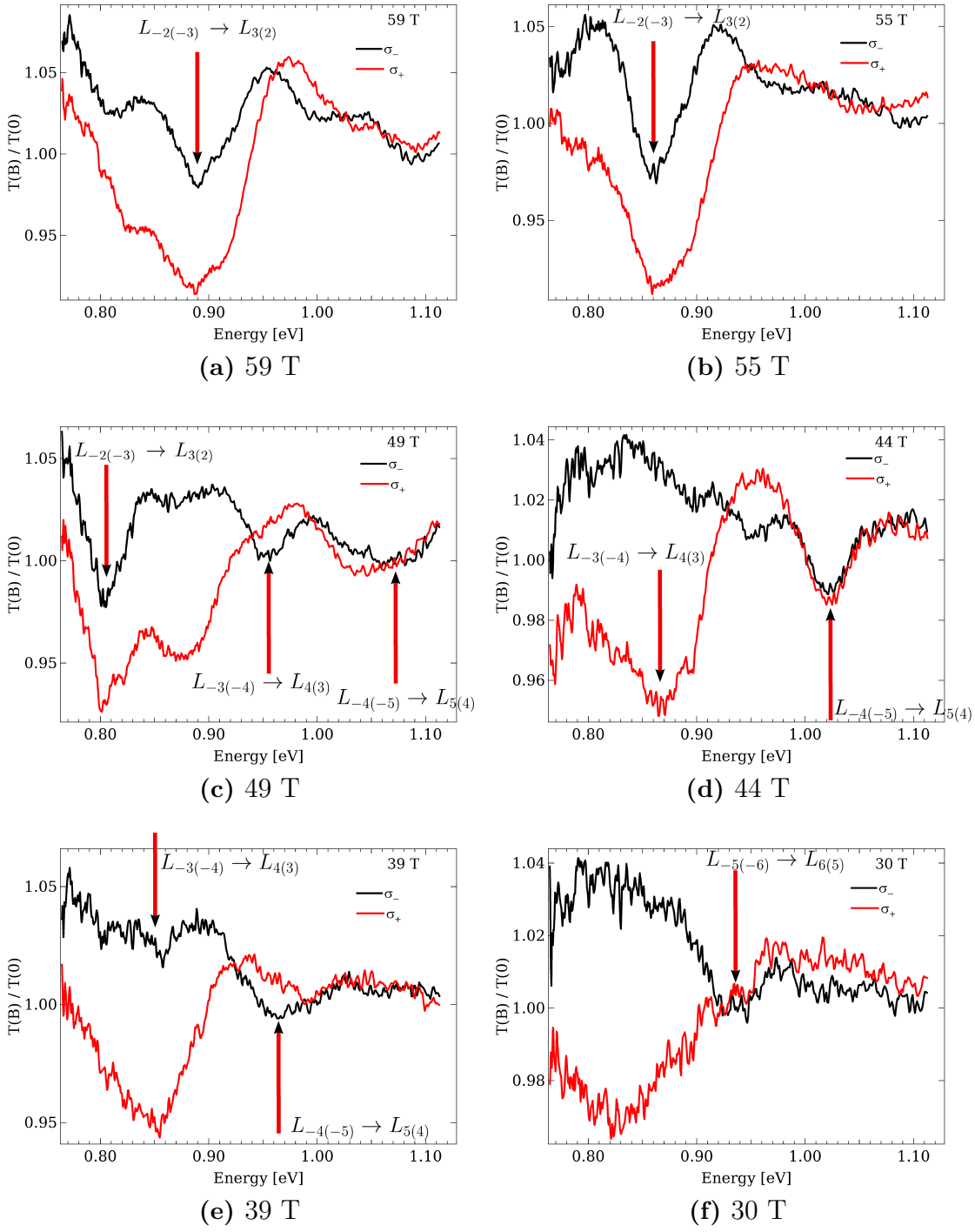

(a) 59 T **(b)** 55 T

(c) 49 T **(d)** 44 T

(e) 39 T **(f)** 30 T

Figure 5.5 *– Polarisation resolved spectra in fields between 30 and 60 Tesla. σ_- and σ_+ spectra are directly compared to each other. In particular the different intensities of the lines are puzzling and not expected even in presence of electron-hole asymmetry. The arrows are marking the expected transition energy for graphene transitions.*

$$A = \frac{3\sqrt{2}a}{l_B}\frac{t'}{t} \approx 0.08B \text{ [meV, B in T]}. \tag{5.4}$$

The existence of this terms requires the existence of an electron-hole asymmetry. The strength of the asymmetry here is not dependent of n and has a magnitude of $A \approx 5$ meV at 60 Tesla. This is rather close to our experimental resolution. The peak width is very large (≈ 50 meV) even at very low temperatures which is not helpful to detect this small effect. In addition the described model does not predict any influence on the oscillator strength. We thus can not claim that the difference between the spectra is due to an electron-hole asymmetry.
Recent optical conductivity calculations investigate optical transitions in graphene, a quantity which is directly linked to the oscillator strength [Gusynin 2006]. Although these calculations focus on the fundamental transition, i.e. $L_{-1(0)} \rightarrow L_{0(1)}$, they do not predict any difference in oscillator strength for opposite polarisation. The simplest approach for magneto-optical properties of graphene can be obtained from the Kubo-Greenwood formula [Kubo 1957, Greenwood 1958, Moseley 1978] which is given by

$$Re(\sigma^{\pm}(\omega)) = \frac{4e^2|eB|\gamma}{\omega h\pi}\sum_{n,m} |\langle m|\, v_{\pm}\, |n\rangle|^2 \frac{f_n - f_m}{\Delta E - \hbar\omega + \gamma^2} \tag{5.5}$$

where γ is a broadening parameter, $f_{m,n}$ is the occupation of the nth Landau level and $\Delta E = E_m - E_n$ the transition energy. $\langle m|\, v_{\pm}\, |n\rangle$ is the matrix element of the velocity operator such that $|\langle m|\, v_+\, |n\rangle|^2 = \alpha\delta_{|m|,|n|+1}$ and $|\langle m|\, v_-\, |n\rangle|^2 = \alpha\delta_{|m|,|n|-1}$ with $\alpha = v_F^2/2$ in n or m equal to zero and $\alpha = v_F^2/4$ otherwise [Abergel 2007, Gusynin 2006, Sadowski 2006].
From the point of view of the above described theories equation 5.5 can not explain such a difference in oscillator strengths. Indeed since we are measuring at high energies we can assume to be far away from the Fermi energy where a difference in occupation of Landau levels could play a role [Orlita 2008b, Sprinkle 2009]. I.e. we can assume $f_n - f_m = 1$.
We recall here that Deacon *et al.* introduced different velocities for electrons and holes instead of one Fermi-velocity to describe an electron-hole asymmetry [Deacon 2007]. This would be a way to explain the difference in oscillator strength. However this model has a different microscopic origin and is attributed to corrections of the nearest neighbour overlap integral. At magnetic fields of approximately 30 Tesla this model is expected to give corrections larger than 15 meV, which however could not be identified in our data and by other magneto-transmission measurements at these field strengths [Plochocka 2008].
The features observed in our spectra can not be explained using the electron-hole asymmetry. A hypothesis will be discussed in the following.

5.1.2.4 Bi-layer contributions

In order to explain the polarisation dependence of the spectra in figure 5.5 we suggest a level crossing due to contributions of bi-layer graphene. In figure 5.1 the $L_{-4(-5)} \rightarrow L_{5(4)}$ transition is abruptly disappearing at field strengths above 50 Tesla ($\sqrt{B} \approx 7$ T$^{1/2}$). However a closer inspection of the spectra reveals that the transition is strongly broadening and dramatically deviating from the experimental expected transition. As shown in the spectra in figure 5.5 we observe additional transitions which are polarisation dependent. We plot the energy positions of the polarisation resolved experiments as a function of magnetic field in figure 5.6a. We can detect some transitions which are clearly deviating from the theoretical prediction presented by the black solid lines.

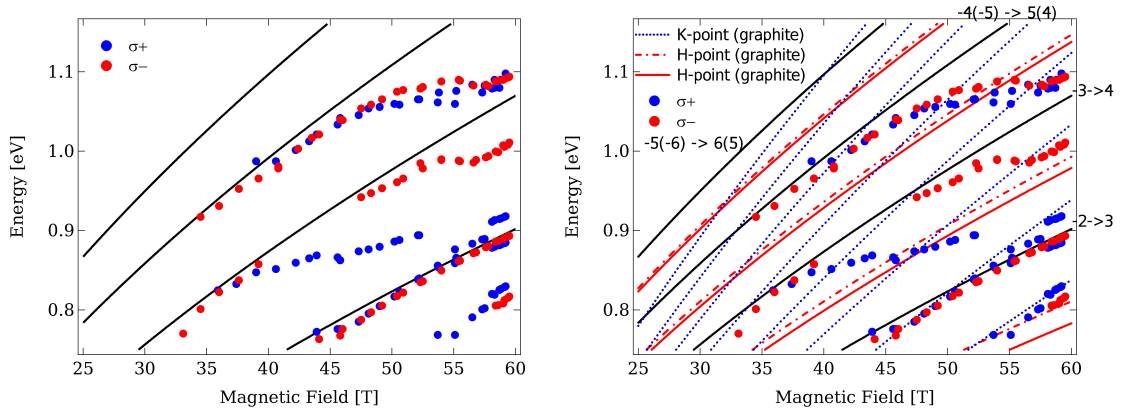

Figure 5.6 *– (a) Experimental positions of polarisation resolved transitions observed between 30 and 59 Tesla (blue and red circles). The theoretical graphene transitions are denoted by the black solid lines. (b) We add the bi-layer transitions from the model discussed in section 2.6.2. Dotted blue lines are transitions from the* ***K****-point of graphite. Solid red and dot-dashed red lines represent* ***H****-point transitions of graphite denoted with their apparent selection rules* $\Delta n = 0$ *and* $\Delta n = 2$ *in figure 2.14b. Levels deviating from the graphene transitions are ending on the bi-layer transitions.*

We then can add the transitions we get from the effective bi-layer model as developed in section 2.6.2. This case is presented in figure 5.6b. We can see that some transitions seem to begin to follow the bi-layer transition we added to the fan-chart. Note that the agreement between the theoretical lines and the experimental points is better at lower photon energies. The sample investigated in figure 5.5 also showed some bi-layer transitions at low magnetic fields in the far-infrared spectral range[2]. One could however ask why the bi-layer contributions are not more visible in the spectra which are not polarisation resolved. The polarisation seems to be accurately resolved and the transmission after the pulse normalised by the zero field transmis-

[2]Private communication, P.Plochocka

sion yields a straight line at unity, excluding displacements or other systematical errors. In addition to this the bi-layer peaks are broader than the transitions attributed to massless Dirac fermions and polarisation dependent (see section 2.6.2). The graphene transition remain well defined most of the time in both polarisations (see figure 5.5). In the polarisation independent spectra the supposed bi-layer contributions are thus compensated by their polarisation dependence and more importantly by their broadness.
Some transitions corresponding to mono-layer transitions seem however to be polarisation dependent. For example the $L_{-3(-4)} \rightarrow L_{4(3)}$ transition is present in the σ_+ spectrum at 39 Tesla and vanishing at 49 Tesla. In figure 5.7 we show that this behaviour is mostly induced by the polarisation dependence of the bi-layer contributions we observe in our spectra.
We first fit the σ_--spectra at 49 Tesla with different Lorentzian peaks. As we can see in figure 5.7a the fit accurately reproduces the experimental data. We also fit the σ_+-spectrum keeping the width of the observed lines constant. The mono-layer graphene transitions yield the same result as the σ_--spectrum as can be seen on the peak form of each single peak fit below the spectra in figure 5.7. The polarisation dependence is thus induced by the additional bi-layer contribution we observe in the spectrum.

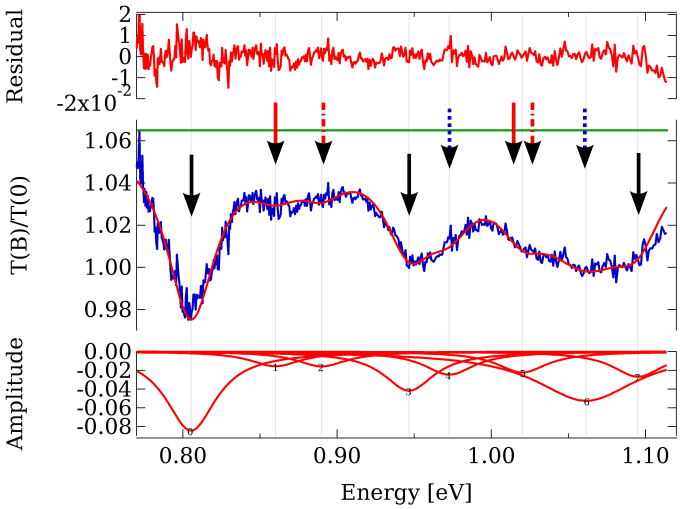

(a)

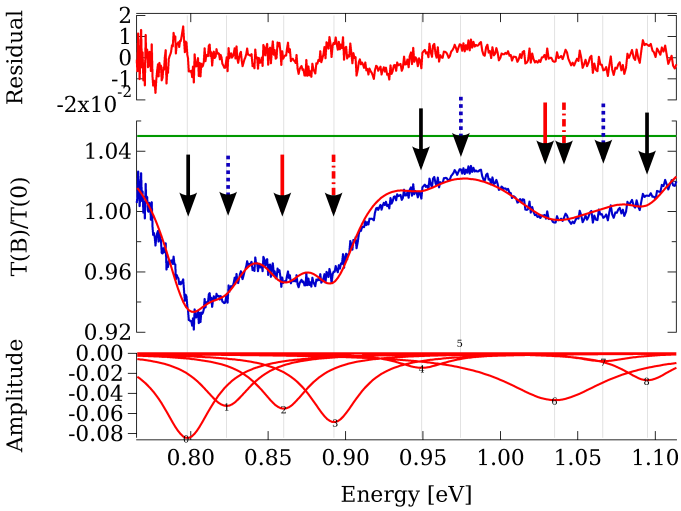

(b)

Figure 5.7 – *(a) Fit of the 49 Tesla σ_--spectrum with Lorentzian peak forms. The graphene transitions are denoted by the black arrows. The additional peaks are corresponding to transitions from the effective bi-layer model. The colour and line code of figure 5.6 for the other arrows which correspond to the bi-layer transitions is preserved. (b) Fit of the 49 Tesla σ_+-spectrum. The mono-layer graphene absorption peaks yield the same result as for σ_-. The polarisation dependence is thus induced by the bi-layer transitions. The reflection and transmission coefficients are also strongly affected probably due to the Faraday effect. It introduces an additional complication.*

However we have a slight disagreement for the $L_{-3(-4)} \rightarrow L_{4(3)}$ transition peak which seem to be missing in the σ_+-spectrum. In figure 5.7b the amplitude of this transition is smaller than in the σ_--spectrum but clearly present. As discussed before graphene exhibit a strong Faraday rotation [Crassee 2010] and can induce a large difference in the refractive index for left and right handed circularly polarised light. The scale of the differential transmission indicate that the reflection and transmission coefficients of the sample are clearly affected by this effect. This can additionally influence the observed amplitude of the transition. However as we do not have any information on the reflection of the sample this remains only a hypothesis.
We are aware of the fact that the need of many parameters to fit the spectra with additional bi-layer transitions makes the interpretation ambiguous. However the analysis of a second sample is consistent with the assumption that the observed polarisation dependence is induced by additional bi-layer transitions. In figure 5.8 we present the polarisation resolved spectra of the second sample. Its polarisation dependence is obviously weaker than the sample presented in figure 5.5. The main difference between both samples is that the sample in figure 5.8 only shows very weak bi-layer transitions. In this figure we presume the presence of some absorption peaks corresponding to the transitions of bi-layer graphene (marked by grey arrow).
Considering all previously exposed arguments we suggest that the observed polarisation dependence might be induced by bi-layer transitions.

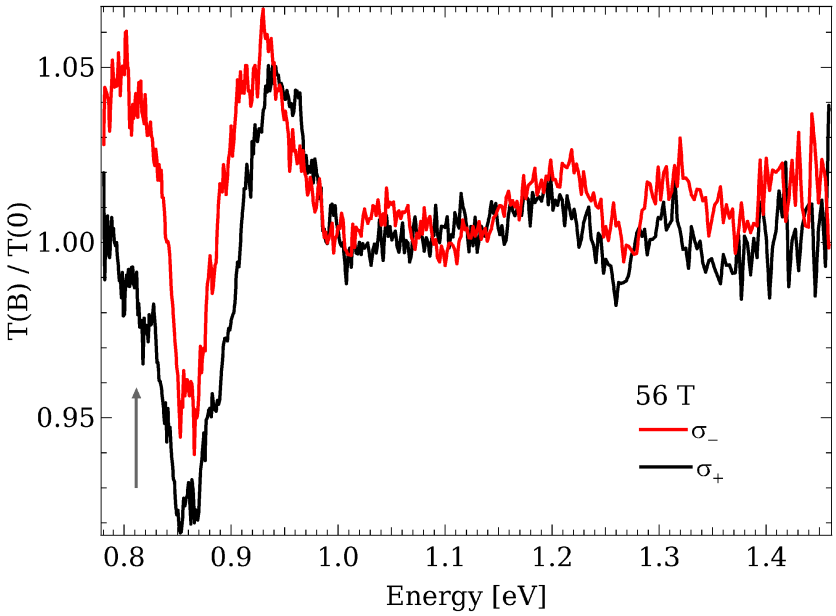

Figure 5.8 *– σ_+ and σ_- polarisation resolved spectra at 56 Tesla for a second sample. The bi-layer contribution is very weak but present and polarisation dependent. Its position is marked by the grey arrow. The difference in amplitude is much weaker than for the first sample. We can conclude that the observed polarisation dependence in multi-layer graphene on SiC is induced by the additional transitions we may attribute to bi-layer graphene.*

5.1.2.5 Temperature dependence

The effective mass of semiconductors shows in general a temperature dependence as the band structure varies with temperature. In analogy, we want to probe the temperature dependence of the transitions in graphene in order to identify any thermal effects on Dirac fermions. A representative spectrum for each measured temperature at a magnetic field strength of 58 Tesla is plotted in figure 5.9. The temperature was varied between 4.2 K and 295 K. We can assign the most pronounced peak to the $L_{-2(-3)} \rightarrow L_{3(2)}$ transition.
The remarkable quality of these kind of graphene samples can be observed in this figure. In contrast to conventional low dimensional systems the Landau level transitions are still clearly visible at room temperature. To check if we can identify any significant temperature effect we fit the observed transitions with a Lorentzian line shape and assume thermal broadening of the peak. Note at high temperatures the absorption peak seems to be slightly distorted and one may fit the absorption line with two Lorentzian peaks. However no effect can be resolved within our experimental resolution and at this day there is no theory which would explain the presence of a second peak.
In figure 5.10 we plot the fitted area and width of the main peak as function of temperature. In addition we fit the experimental points which yield $8.58{\cdot}10^{-2}$ meV/K for the slope of the line. This is in very good agreement with the Boltz-

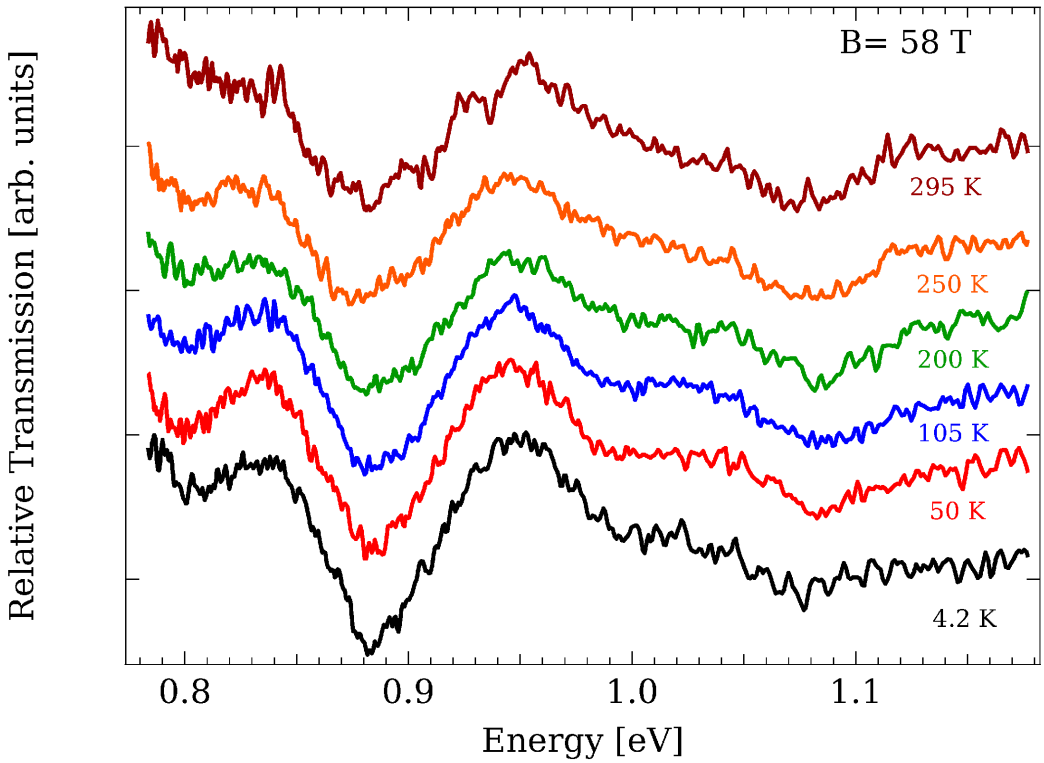

Figure 5.9 *– Spectra at 58 T at temperature between 4.2 K and 295 K. The only observed feature is the weakening in intensity of the transition lines. No shift or new peak apparition can be noted which indicates a pure sample.*

mann constant defined by k_B =8.62·10^{-2} meV/K. The full width at half maximum is increasing proportional to the thermal energy. The peak area remains constant. The decreasing intensity can thus be attributed to the thermal broadening of the Landau level transition.
Our observation agrees with recent reports on temperature dependent transmission measurements at low magnetic fields on the fundamental $L_{-0(-1)} \rightarrow L_{1(0)}$ transition. The observation of Landau level transitions at room temperature indicates that the carrier mobility in this samples is very high even at room temperature. It is estimated to be around $2.5 \cdot 10^5$ cm^2/(V·s) which is one order of magnitude higher than in standard two dimensional GaAs (10^4 cm^2/(V·s)) [Orlita 2008b].

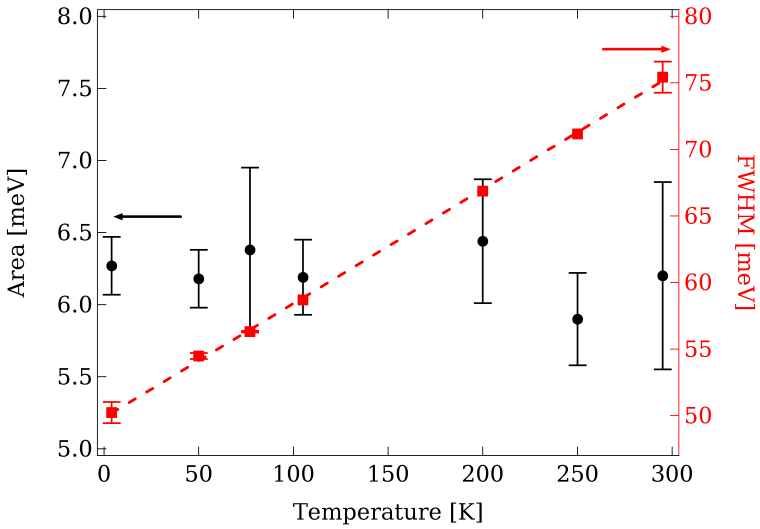

Figure 5.10 *– Temperature dependence of the fitting parameter, FWHM (red squares, right axis) and area (black circles, left axis). The intensity decrease with increasing temperature is consistent with simple thermal broadening as witnessed in the width of the peak. The dashed line is the fit of the peak width and the slope corresponds to the Boltzmann constant.*

5.2 Magneto-optical spectroscopy of graphite

5.2.1 Sample

Let us now turn to the results of the magneto-transmission measurements of natural graphite. The sample used in this experiments was around 100 nm thick. Such a thin layer was obtained by mechanical exfoliation of natural graphite. We have used a thin layer to be able to measure a transmission signal as graphite is an opaque material.

The experimental setup is described in chapter 3. The measurements were all performed in Faraday configuration. The *c*-axis of the crystal is thus parallel to the magnetic field. Part of these measurements were also performed at the DC-field facility in Grenoble.

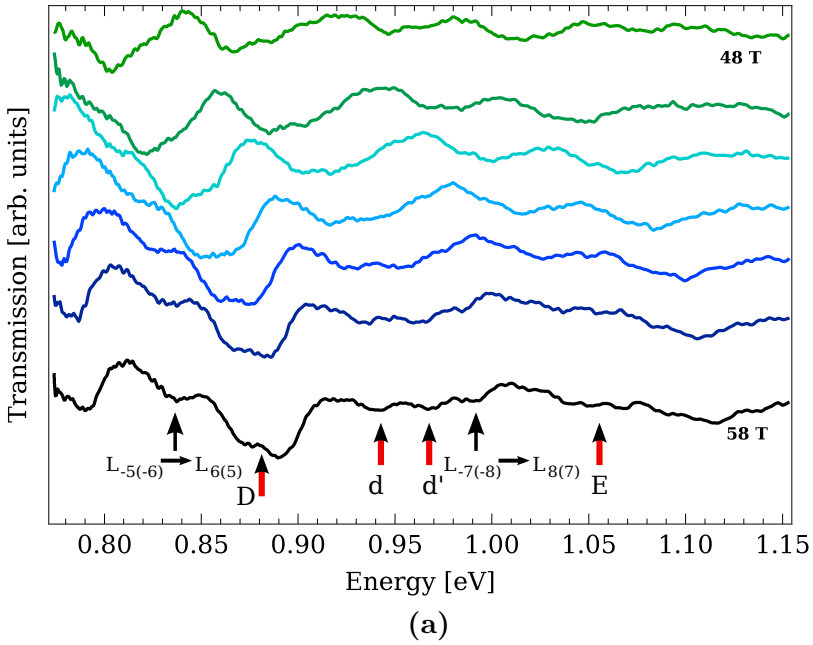

(a)

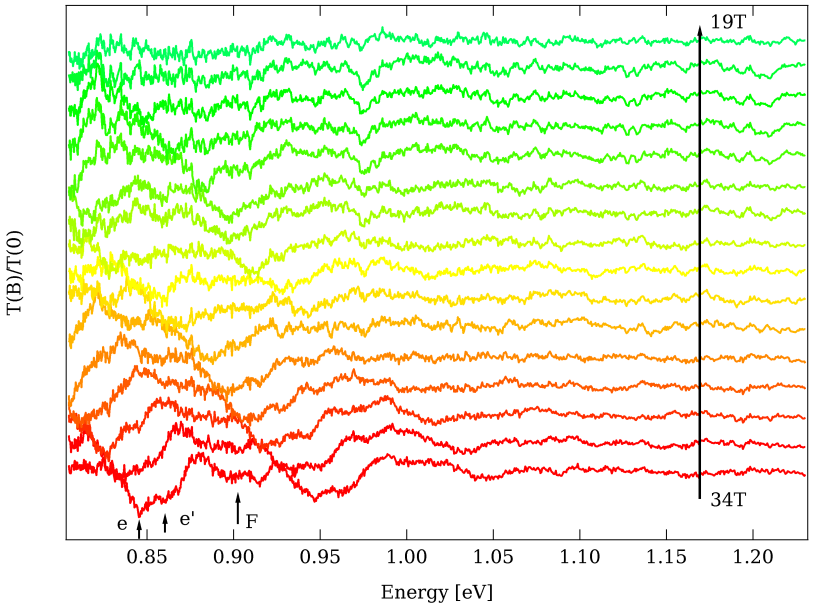

(b)

Figure 5.11 – *(a) Absorption spectra of graphite at various magnetic fields in the range from 58 to 48 Tesla. As expected graphite is showing a rich spectrum with several absorption peaks governed by transitions around the **H**- and the **K**-point. The absorption lines show a strong field dependence. The assignment of the peaks is described in the text. Additionally we observe the D-transition which seem to split at high fields. (b) Absorption spectra of graphite at various magnetic fields in the range from 19 to 34 Tesla performed in a DC-magnet at LNCMI-Grenoble at a temperature of 8 K. We still observe a rich spectrum. We can also identify a splitting in the graphene like transition (F).*

5.2.2 Magnetic field dependence

Typical experimental results are presented in figures 5.11a and 5.11b for transmission experiments in different magnetic fields. These experiments were performed without light polarisation. In figure 5.11a we select some representative spectra between 48 and 58 Tesla obtained with a pulsed magnet at LNCMI-T. In figure 5.11b we show the spectra obtained between 19 and 34 Tesla in a DC-magnet at LNCMI-G which complete the magnetic field dependence in the same spectral energy range. Since the absorption in this energy range is weak, the spectra are all normalised by the zero field transmission and offset for clarity.
As expected the absorption spectra of graphite is much richer than the one of graphene due to the more complex band structure and hence more allowed transitions (see figure 2.14b). We can also identify a strong magnetic field dependence of our identified transitions, indicating that we indeed observe Landau level transitions. Additionally it seems that some peaks (e.g. D) are showing a splitting when the magnetic field increases. Such a splitting is very surprising because there is no previous report of the observation of such a behaviour and it is not expected from theory.
For convenience we recall in table 5.1 the selection rules established in section 2.6. Each peak is displayed by the different markers in figure 5.12. We calculate the energy of the predicted optical transitions at the **H**- and **K**-point of graphite using the effective bi-layer model developed in section 2.6.2 and written explicitly in equation 2.47. The aim is to describe the Landau level fan-chart with only two coupling parameters, i.e. γ_0 and γ_1, to take the intra- and inter-layer coupling into account respectively. This is equivalent to treating graphite as a series of effective bi-layers whose effective coupling depends on k_z.
We assign the observed transitions at the **H**-point with help of the Landau level fan-chart which will be discussed in detail later. In figure 2.14b the dipole allowed transitions in graphite are presented. The graphene like transition $E_{3-}^{3(2)} \rightarrow E_{3+}^{2(3)}$ have the same energy as the $E_2^{2(1)} \rightarrow E_1^{1(2)}$ transitions which have a quantum number n which is lower by one. These lines are labelled with capital letters and correspond to the dipole allowed transition $|\Delta n| = 1$.
The dipole allowed transitions with $|\Delta n| = 0$, which correspond to the mixed transitions $E_{3-}^3 \rightarrow E_1^2$ and $E_2^2 \rightarrow E_{3+}^3$ are labelled with small letters, and are dipole for-

Table 5.1 *– Assignment of the Landau level transitions in graphite. The features are extensively discussed in section 2.6.*

Label	**H**- or **K**-point	Apparent selection rule	Particularity
D,E,F,...	**H**	$\|\Delta n\| = 1$	Graphene-like
d,e,f,...	**H**	$\|\Delta n\| = 0$	
d',e',f',...	**H**	$\|\Delta n\| = 2$	
$L_{-n(-m)} \rightarrow L_{m(n)}$	**K**	$\|\Delta n\| = 1$	

bidden in graphene. Finally, the transition named with small letter and prime (e.g. d') shows dipole allowed degenerate 'mixed' transitions $E^2_{3-} \rightarrow E^3_1$ and $E^3_2 \rightarrow E^2_{3+}$ which correspond to transitions with $|\Delta n| = 2$ of the series from the **H**-point, a transition which is usually dipole forbidden. The **H**-point transitions depend only on the parameter γ_0 and evolve always as $\sqrt{B}$ as we derived in equation 2.49.
Peaks denoted in the form $L_{-n(-m)} \rightarrow L_{m(n)}$ are transitions from the **K**-point of graphite. The **K**-point transitions begin to have large quantum numbers in this energy range and are thus very weak. The **K**-point transitions are on the other hand also dependent on the coupling parameter γ_1. At low energies, i.e. $E \ll \lambda\gamma_1$, the transitions evolve linearly with magnetic field before increasing as $\sqrt{B}$ at high energies, i.e. $E \gg \lambda\gamma_1$. At the **K**-point we have $\lambda\gamma_1 = 0.75$ eV so that we are in an intermediate regime.
Using the tight binding parameters fixed at $\gamma_0 = 3.15$ eV, which corresponds to Fermi-velocity of $v_F = 1.02 \cdot 10^6 m.s^{-1}$, and $\gamma_1 = 0.375$ eV we plot the theoretically predicted optical transitions in graphite on figure 5.12. On the top of the calculations the position of each absorption line is shown. The values of the tight-binding parameters were determined from magneto-absorption measurements at lower magnetic fields [Orlita 2009b].
In figure 5.12 we can see very good agreement between the theory and the experimental data. This is remarkable in particular when we take into account that the calculated energies are not fitted to the data, i.e. the parameters were not adjusted to our data. The most pronounced peaks are the **H**-point transitions labelled with capital letters and presented by the thick blue line corresponding to the apparent selection rule $|\Delta n| = 1$. The remaining transitions arising from the **H**-point are weaker but well distinguishable in the spectra. Their field dependence is plotted with red dotted and dot-dashed lines.
The **K**-point transitions, black dashed lines and black stars, are only observed at high magnetic fields. On the other hand, the lowest quantum number for this series in our spectra is $n = 5$. For completeness we have included phenomenologically the electron-hole asymmetry as suggested in the work of Henriksen *et al.* [Henriksen 2008] and Chuang *et al.* [Chuang 2009]. We use here different Fermi-velocities for electrons, $v_e = 1.098 \cdot 10^6 m.s^{-1}$, and holes, $v_h = 0.942 \cdot 10^6 m.s^{-1}$. This values are slightly different from the values determined by Chuang *et al.* in order to match the "average" value of $\gamma_0 = 3.15$ eV. Due to the high quantum number of the **K**-point transitions and the weak absorption lines this electron-hole asymmetry is below the experimental resolution.

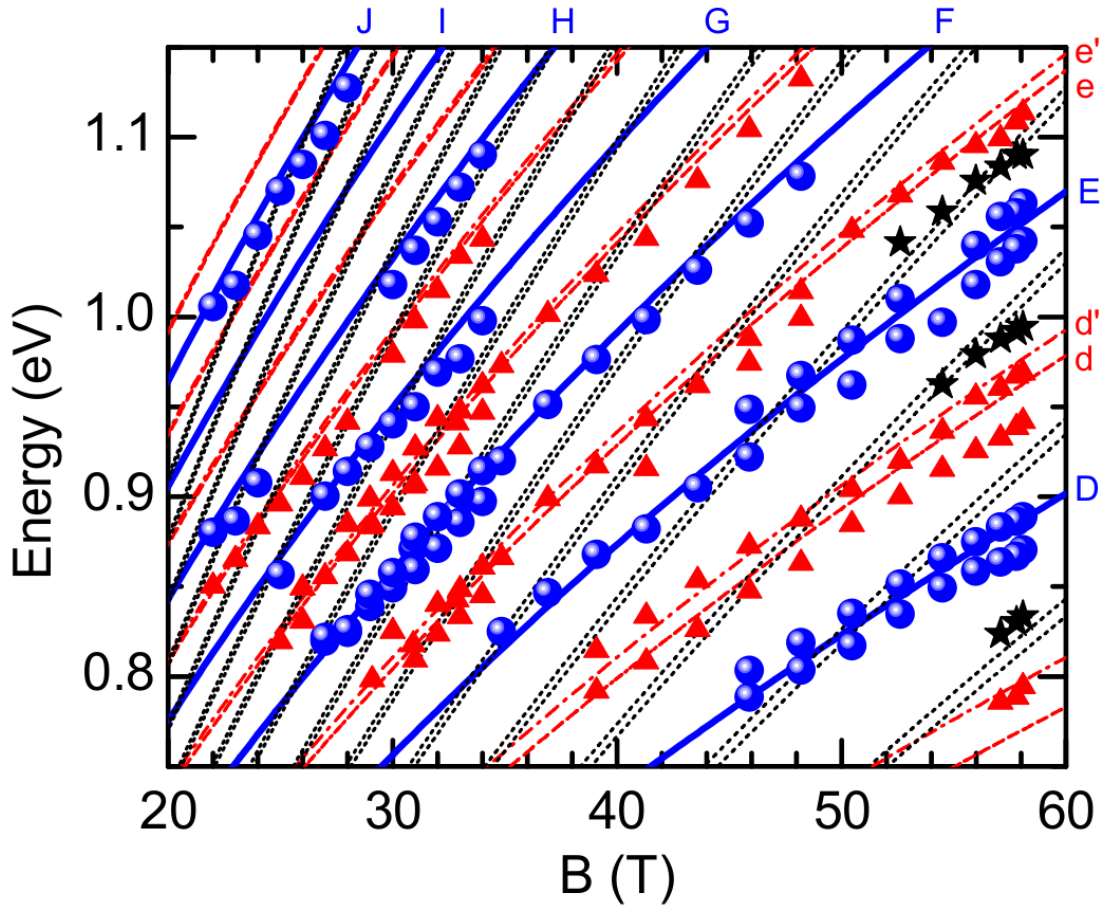

Figure 5.12 *– Landau level fan-chart of graphite at high magnetic fields and high energy. The experimental observed transitions are assigned for the* ***H****-point (graphene like) with blue balls,* ***H****-point with* $|\Delta n| = 0$ *and* 2 *are displayed by red triangles;* ***K****-point transitions are the black stars. The lines are the calculated energies of the dipole allowed H-point (solid, dotted and dot-dashed lines) and* ***K****-point (black dashed lines) transitions as described in the text.*

5.2.3 Splitting in the graphene-like transition

As mentioned above the main transitions in our spectra show what looks at first sight to be splittings. This is rather unexpected and is not observed in magneto-transmission experiments on graphene [Plochocka 2008]. This apparent splitting is clearly observed in the transitions D, E and F in figures 5.11b, 5.11a and 5.13, which are the graphene like transitions with effective selection rule $|\Delta n| = 1$. Remember, the field dependence is governed by equation 2.49.
A closer inspection of the magnetic field evolution in figure 5.12 indicates that the calculated transition better fits the lower energy transition for fields below 50 Tesla before fitting better to the high energy feature at fields above 54 Tesla. This scenario could however be attributed to an avoided level crossing rather than a splitting. The inspection of the D-transition in the absorption spectra of figure

5.11a supports this hypothesis. It is clearly seen that the peak form evolves with magnetic field. At low fields the lower lying peak is pronounced, while in contrast to this at the highest fields the higher energy peak predominates. There is however a lack of theoretical models which could reliably explain this anti-crossing.
We can exclude an inhomogeneity in the sample. The measurements were repeated several times and we did not irradiate the same region of the sample at each experiment. We could not detect any impact on the splitting. Furthermore a slightly different Fermi-velocity for different regions would simply lead to a strong field dependence in the position of both peaks. However we only observe a field dependence in intensity.

5.2.4 Temperature dependence

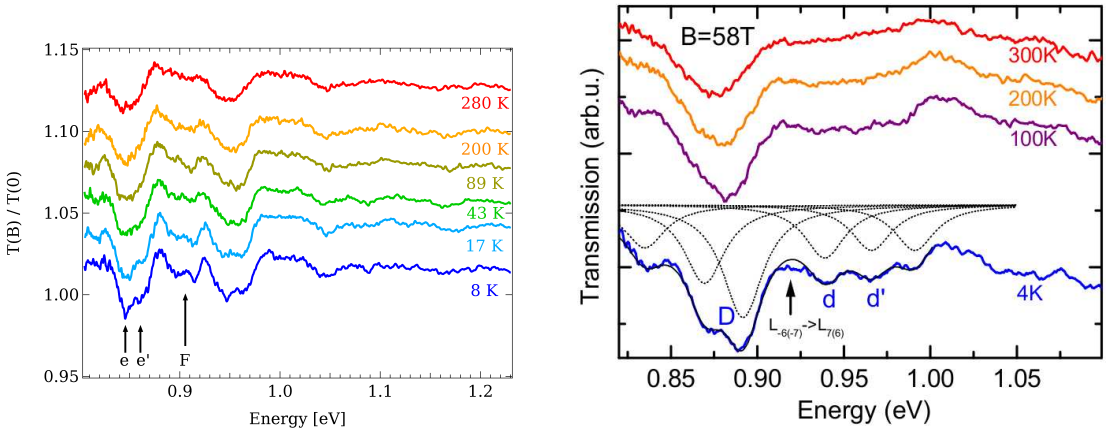

(a) (b)

Figure 5.13 *– Temperature dependence of graphite in (a)a DC-field and (b) a pulsed field where the field values are 34 and 58 Tesla respectively. A temperature of almost 50-100 K is sufficient to suppress the splitting of the main transitions. Most of the peaks are still visible even at room temperature. (b) Spectra used to fit the experimental data at different temperatures (4 K - 300 K) with Lorentzian shape functions (black dashed lines). The thin black line is the fit for the spectra at 4 K. It matches the experimental data very well and the small disagreement can be attributed to the "missing"* $L_{-6(-7)} \rightarrow L_{7(6)}$ *transition from the* ***K****-point.*

We varied the temperature in the pulse field experiment between 4 K and room temperature and between 8 K and room temperature in the static field experiments. Spectra at each temperature step are displayed in figure 5.13.
Graphite exhibits a clear temperature dependence. Most of the absorption lines however only undergo thermal broadening, as we also saw in multi-layer graphene. The lines are often only weakly visible at room temperature. The transition which seems to split is still visible at room temperature but has a clear temperature dependence.

The most pronounced observation in the temperature dependent experiments is that a temperature of 50-100 K is already sufficient to suppress the apparent splitting. However even at room temperature the transition remains visible. We present the temperature dependent spectra again in figure 5.13b but we fit the 4 K spectra with a Lorentzian line shape fixing the full width at half maximum (FWHM) at 28.5 meV for all transitions. The result of the fit (solid black line) describes the data well. The individual peaks are shown as dotted lines. The broadening of the transition is of the order of the energy separation. With increasing temperature we keep all parameters constant and increase the broadening of our Lorentzian lines. It results in a reasonable fit for the high temperature data but in a mismatch for the D-transition. To fit this peak we have to change the amplitude of the Lorentzian components, in addition to the already broadened FWHM. There is no physical argument which can explain this amplitude change to fit the data. We can therefore conclude that thermal broadening alone cannot explain the observed temperature dependence of the D, E, F-transitions.
Note we can detect a small disagreement between the fit and the experiment around 0.92 eV. It can be explained by the presence of the $L_{-6(-7)} \rightarrow L_{7(6)}$ transition from the **K**-point which could not be assigned in the fan-chart in figure 5.12.

5.2.5 Polarisation resolved measurements

Considering the full SWM-model we do not expect a splitting at all since the effect of trigonal warping disappears at the **H**-point. We can check if the non-vertical inter-layer coupling parameter γ_4, which is supposed to introduce an electron-hole asymmetry, contributes to the splitting. Therefore we resolve our spectra with circular polarisation. This case is presented in figure 5.14 where we show two spectra for different polarisation and we focus on the transitions D, d and d'. We use the same setup like in the previous section with an achromatic $\lambda/4$-wave plate and polariser. We clearly see in this picture that the D-transition is unaffected by the polarisation and this splitting cannot be explained under any circumstances by an electron-hole asymmetry. In contrast the d and d' transitions clearly are polarisation resolved, where one of the lines is almost vanishing either with σ_+ or σ_- excitation. This behaviour can be explained with the selection rules we sketched in figure 2.14b where either the $E_{3-} \rightarrow E_1$ or the $E_2 \rightarrow E_{3+}$ transition prevails. This is in any case a good confirmation about the quality of polarised light. Unfortunately we only assigned the polarisation arbitrarily and thus cannot assign the transition formally.
We have to keep in mind that although trigonal warping terms are vanishing at the **H**-point they induce magnetic breakdown effects in vicinity of the **H**-point which could be observed in magneto-optical spectra at the **H**-point [Nakao 1976]. This occurs from the anti-crossing of the Landau levels from the E_3 band with the Landau levels from E_1 and E_2 bands, see figure 2.14a for details.

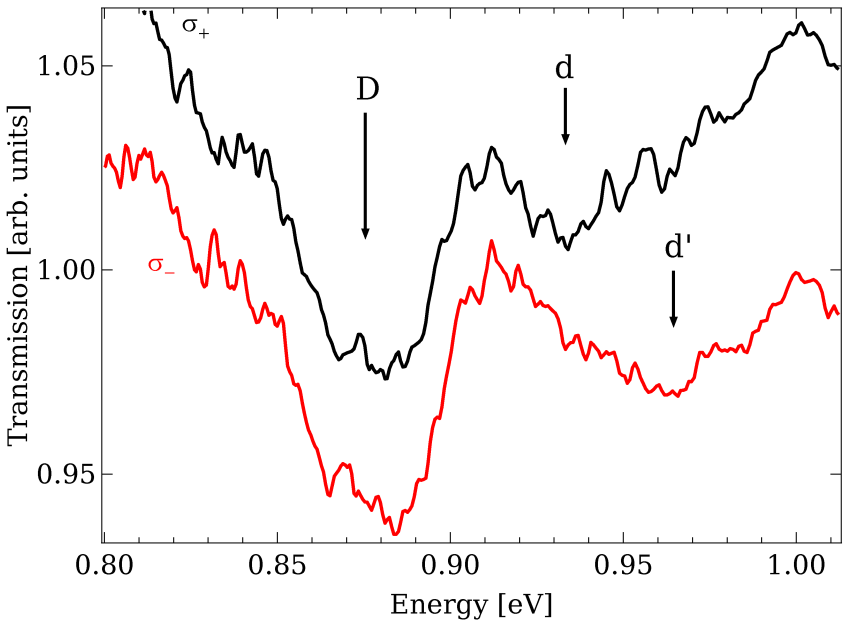

Figure 5.14 *– Polarisation resolved spectra at 58 Tesla and 4 K. While no polarisation dependence can be identified in the spectra of the D-transition, the d- and d'-transitions vanish either in σ_+ and σ_-. The splitting of the main peak can thus not be explained by thermal broadening or electron-hole asymmetry.*

5.3 Summary

We have investigated in this section the magneto-optical properties of multi-layer graphene. We completed the Landau level fan-chart for graphene up to 60 Tesla in the energy range of 0.8 to 1.2 eV. The experimentally observed deviations can be attributed to effects of trigonal warping induced by next-nearest-neighbour interactions. These are also predicted to introduce an electron-hole asymmetry. We could not identify such an asymmetry in our polarisation dependent spectra because this effect is probably below our experimental resolution. We also observe contributions which can be attributed to bi-layer structures in the sample. Finally, deviations of the experimental Landau levels due to electron-electron interactions were not observed in the present data.
In the second part of the chapter we performed magneto-optical experiments to probe the **H**- and **K**-point Landau level transitions in natural graphite . As expected the transmission spectrum of graphite is richer than the one of graphene and is dominated by the graphene-like transitions of the **H**-point. A reduced SWM-model with only two parameter γ_0 and γ_1 correctly describes all observed transitions apart from a splitting observed for the graphene like transitions. Polarisation resolved measurements confirm that the apparent splitting of the graphene like series at high magnetic field cannot be attributed to an asymmetry of the Dirac cone. At current time no explanation has been found.

Chapter 6

Conclusion

In this thesis we completed an study of the magneto-optical properties of single-walled carbon nanotubes, graphene and graphite as well as the alignment dynamic of carbon nanotubes in a pulsed magnetic field. We used absorption and photoluminescence techniques combined with high magnetic fields, among the highest obtainable at these days, to study these systems.

Magnetic fields are a powerful tool for examining the excitonic nature of the optical response of single walled carbon nanotubes. Through the performed measurements we could identify the role of the tube-threading flux determining the changes in peak energy and intensity as a function of magnetic fields. This was done using highly oriented SWNT. However there remain some open questions. Among these is the influence of the environment of the SWNT, which seems to play a significant role but is not yet clarified. Encouraging work is underway to understand for example the influence of strain [Nish 2008]. Micro-photoluminescence on single nanotubes can also give a sharper representation of the excitonic nature of the optical response. Such measurements demonstrated the magnetic brightening at fields of only 4-5 Tesla [Matsunaga 2008, Srivastava 2008].

We also measured the dynamic alignment of SWNT. Due to their intrinsic magnetic anisotropy an external magnetic field aligns the tubes parallel to itself. We used linear dichroism as the experimental method to investigate the dynamics of this process, which gives a direct access to the order parameter. We first studied a sample with known length distribution. Although theories seem to be predetermined for these systems the interpretation of poly-disperse length samples remain very difficult. The experimental data are however only well reproduced by length distributions which are different from the length distribution which was obtained by the characterisation of the sample. However even the characterisation methods show very large experimental error bars in particular when only a small part of the prepared solution is used to characterise it. We thus conclude that our samples are not representative enough to match the determined value for the complete solution. To facilitate the interpretation and avoid to handle length distributions, we measured the alignment of solutions with length sorted tubes. The high concentration of these samples led us to reformulate the rotational diffusion in the semi-dilute

regime for this process. But even this extension of our model can not reproduce the experimental data accurately.
A closer inspection of the field dependence in the up-sweep of the alignment showed an effect which resembles to a magnetic field induced phase transition from an isotropic to nematic liquid crystal. This effect can explain some features we observe in our data. In addition, the order parameter of the sample is showing a concentration and field dependent saturation and the alignment decay is best fitted by a double exponential decay. Two competing theories, the diffusion in two environments [Shears 1973] and the restricted rotational diffusion [Warchol 1978], can qualitatively explain the process. However more experimental data are needed to clarify the issue, in particular concerning the interaction of the solvent or the surfactant with the nanotubes, which is completely neglected here.

Our investigation of the magneto-optical properties of multi-layer epitaxial graphene confirmed the influence of trigonal warping on the band structure of graphene in the high energy limit which was proposed by Plochocka *et al.* [Plochocka 2008]. Additionally we could not identify the signature of electron-electron interactions, although they have been observed on mono-layer graphene on SiO_2 in recent works [Jiang 2007]. We attribute this to the dielectric properties of the SiC-substrate used here.
The effect of next nearest neighbour interactions, which lead to trigonal warping, is supposed to introduce an electron-hole asymmetry in graphene which is predicted to be polarisation dependent. Graphene shows a strong polarisation dependence and we attribute this behaviour to weak influences of inter-layer coupling apparently corresponding to transitions of bi-layer graphene. Different theories predict the existence of an electron-hole asymmetry but up today there is only one work which reports its observation [Deacon 2007]. Our results do not confirm such an electron-hole asymmetry.

Finally we close this work with magneto-transmission measurements, which have been used to probe the **H**- and **K**-point Landau level transitions in natural graphite. A graphene like series together with a series of transitions exclusive to graphite were observed. A reduced Slonczewski-Weiss-McClure-model with only two parameters, the inter-layer coupling γ_0 and the intra-layer coupling γ_1, correctly describes all observed transitions. Polarisation resolved measurements confirm that the apparent splitting of the graphene like series at high magnetic field can not be attributed to an asymmetry of the Dirac cone. We suggest that an avoided level crossing might explain this splitting but more theoretical and experimental work is needed to clarify this issue which remains unexplained.

Appendix A

Assignment table

A.1 Assignment table

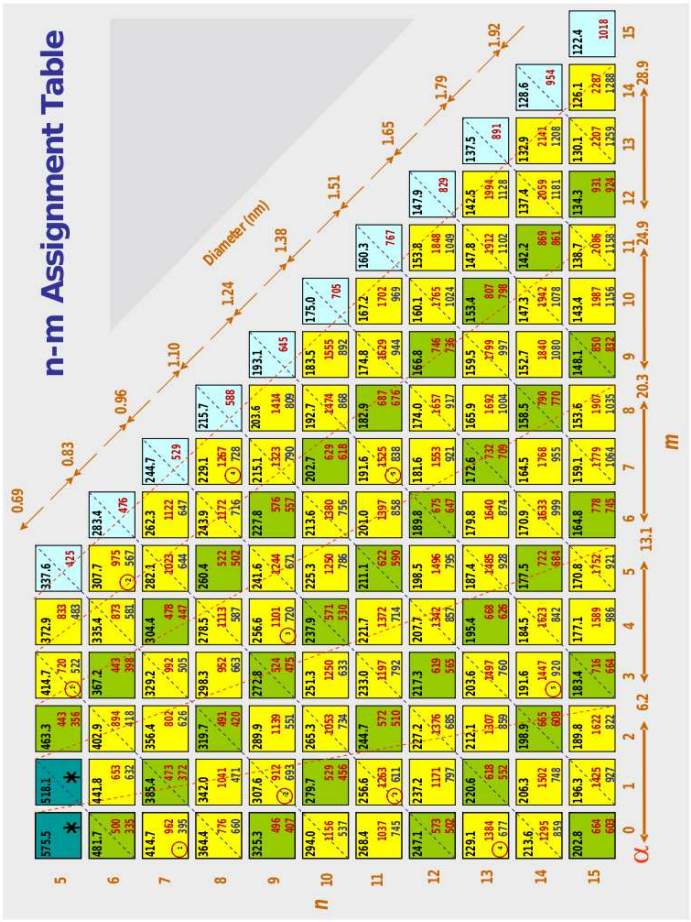

Figure A.1 – *Assignment table for SWNT from [Sivarajan 2004]*

Appendix B

Résumé

Contents

Cette partie annexe veut résumer le travail en langue française de façon complète. Comme ce travail a été effectué en France il est donc logique d'avoir au moins une partie ou un résumé rédigé dans la langue du pays hôte.
Le lecteur ne trouvera aucune information nouvelle dans cette partie et les figures utilisées pour illustrer les explications sont également strictement les mêmes que dans la partie principale. Cette partie a pour but d'informer le lecteur francophone des résultats que nous avons obtenus pendant ce travail. Par contre nous nous contenterons de résumer ces résultats.
Le travail se structure en quatre parties différentes. Les premiers résultats ont été obtenus grâce à la photoluminescence des nanotubes de carbone où nous avons essayé de démasquer la propriété de la luminescence des excitons sombres (*dark exciton*).
La deuxième partie, portant toujours sur les nanotubes de carbone, investit leur alignement dynamique lorsqu'ils sont soumis à un champ magnétique. Effectivement, dû à une anisotropie magnétique dans les nanotubes de carbone, lorsqu'on applique un champ magnétique à des nanotubes solubles dans un liquide on va pouvoir observer une dynamique d'alignement. Le rôle sera de découvrir quels sont les phénomènes et paramètres physiques qui gouvernent ce procédé.
Nous nous intéresserons par la suite à l'absorption du graphène sous champ magnétique intense et en particulier aux transitions entre les niveaux de Landau dont les propriétés diffèrent nettement des gaz d'électrons bi-dimensionnels conventionnels. Finalement l'intérêt qu'aura éveillé le graphène dans le domaine de la recherche, nous a amené à vérifier les propriétés d'un matériau à priori bien connu, le graphite. En appliquant les mêmes méthodes que pour le graphène nous avons pu identi-

fier les transitions entre niveaux de Landau dans le graphite qui sont évidemment plus riches compte tenu du caractère tri-dimensionnels de sa structure du cristallographique.

B.1 Spectroscopie des nanotubes de carbone

Les prédictions théoriques autour des interactions photons-électrons dans les nanotubes envisagent la formation de paires électron-trou fortement corrélées après absorption d'un photon. Dans certains cas on peut redéfinir cette paire électron-trou comme une quasi-particule appelée exciton. Ces excitons peuvent se former dans des systèmes unidimensionnels tels que les nanotubes de carbone parce que les interactions de Coulomb sont amplifiées.
Il aura fallu malgré tout attendre les années 2005 pour obtenir les premières preuves expérimentales de l'existence de ces quasi-particules. Un des nombreux points non résolus est la faible efficacité quantique des nanotubes de carbone. En effet seul un faible pourcentage de photons absorbés dans une expérience de photoluminescence est réémi. Rapidement les excitons sont pointés du doigt et on identifie théoriquement en tout seize niveaux excitoniques, dûs aux différentes dégénérescences de moments électroniques de spins et de vallées. En théorie un seul de ces niveaux est supposé se recombiner en émettant un photon. Les autres sont appelés exciton sombre. Avec un champ magnétique on peut briser la symétrie d'inversion temporelle qui va permettre la recombinaison radiative d'un excitons sombres.
La figure B.1 montre plusieurs spectres d'absorption d'un échantillon de nanotubes de carbone alignés avec différentes configurations de polarisation et d'orientation. On obtient une augmentation significative de l'absorption uniquement lorsque l'axe du tube est parallèle au champ magnétique et à la polarisation. Ceci démontre que les tubes sont bien alignés dans l'échantillon et que uniquement un champ parallèle à l'axe du tube influence les propriétés des excitons dans les nanotubes. Nous ne pouvons pas, malgré tout, détecter un clivage évident du pic d'absorption mais uniquement un net élargissement qui peut être considéré comme un précurseur de ce clivage.
La luminescence des excitons sombres peut-être simplement décrite par un système hyperbolique à deux niveaux dans lequel les dispersions des deux excitons s'écrivent

$$E_{\beta,\delta} = \frac{-\Delta_x \mp \sqrt{\Delta_x^2 + \Delta_{AB}(B)^2}}{2} \tag{B.1}$$

où $i = \beta, \delta$ dénote les états initalement radiatifs et sombres. Δ_{AB} est le déphasage Aharonov-Bohm induit par le champ magnétique. Cette équation peut être utilisée pour ajuster les données expérimentales obtenues par les expériences de photoluminescence.
Cela est réalisé dans la figure B.2. Nous obtenons une valeur de $\Delta_x = 4.8$ meV pour la séparation exciton sombre et lumineux ce qui est en bon accord avec des expériences récentes menées sur des nanotubes individuels.

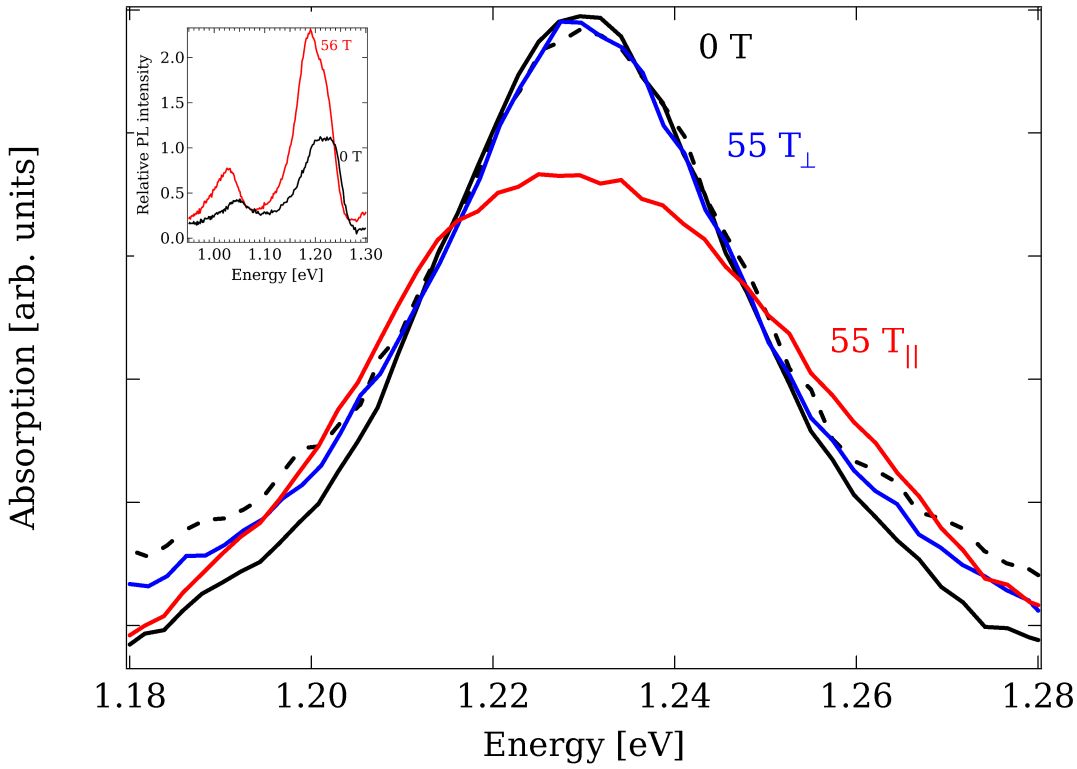

Figure B.1 *– Spectre d'absorption d'un échantillon de nanotubes de carbone alignés en différentes configurations de polarisation et d'orientation par rapport au champ magnétique. On obtient une augmentation significative de l'absorption uniquement lorsque l'axe du tube est parallèle au champ magnétique et à la polarisation. L'insert représente un spectre de photoluminescence du même échantillon sans champ et à 55 Tesla.*

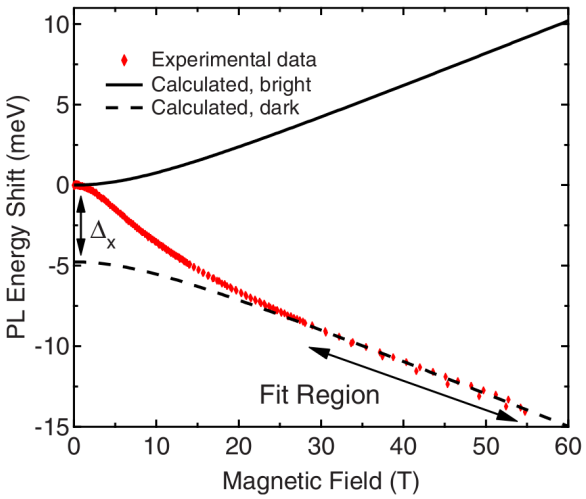

Figure B.2 *– Données expérimentales (point rouge) et décalage théorique (lignes noires) de la position en énergie du pic de photoluminescence en fonction du champ magnétique parallèle à l'axe du tube. On obtient pour le résultat en ajustant les données expérimentales les valeurs* $\Delta_x = 4.8$ *meV et* $\mu = 0.93$ *meV/T nm*^{2}*. Ces valeurs sont réutilisées pour compléter la dépendence en champ magnétique des deux excitons.*

B.2 Alignement des nanotubes de carbone

Dans la seconde partie nous étudions l'alignement dynamique des nanotubes de carbone isolés en solution. Les propriétés magnétiques de ces nano-objets sont fortement anisotropes. Nous étudions des tubes semiconducteurs. Ceux-ci sont diamagnétiques le long de leur axe et perpendiculaires à celui-ci mais la valeur de la suceptibilité perpendiculaire est plus élevée. La différence est définie par

$$\Delta\chi = \chi_{\parallel} - \chi_{\perp} = 1.5 \cdot 10^{-5} emu/mol \tag{B.2}$$

Lorsqu'on applique un champ magnétique les nanotubes vont donc s'aligner parallèlement à celui-ci.

Les règles d'absorption de la lumière par un nanotube vont être propices à ce type d'expérience. En effet seulement une onde avec un vecteur de champ électrique parallèle au tube va être absorbé. Nous pouvons donc utiliser le dichroisme linéaire, une méthode courante pour mesurer l'alignement de molécules. Il se définit par la différence d'absorption de la lumière polarisée parallèlement et perpendiculairement par rapport à un axe choisi, dans notre cas par rapport à l'axe parallèle au champ magnétique.

$$LD = A_{\parallel} - A_{\perp} \tag{B.3}$$

Pour obtenir l'information sur l'alignement total il faut par contre remonter au dichroisme linéaire réduit, définit par

$$LD^r = \frac{LD}{A} = 3S = 3\left(\frac{1}{2}\langle \cos^2(\theta) \rangle + \frac{1}{2}\right) \tag{B.4}$$

où A est l'absorption isotropique à champ nul.
Les données expérimentales vont être décrites par un modèle à base de rotation diffusionelle. Le premier échantillon étudié a été caractérisé afin d'obtenir la distribution de longueur des nanotubes dans la solution, un paramètre fondamental pour la description théorique du processus.
Le dichroisme linéaire est représenté en fonction du temps dans la figure B.3. De plus, sont représentées les simulations avec les paramètres de la solution obtenus avec les mesures rhéologiques et les paramètres qui reproduisent au mieux les données expérimentales.
On constate que les deux courbes théoriques diffèrent sensiblement; en particulier pour l'échantillon avec une viscosité élevée. En effet, les simulations qui reproduisent les données expérimentales donnent une longueur moyenne de nanotube de 700 nm et 1500 nm pour la solution à faible et forte viscosité. La mesure rhéologique a obtenu une longueur moyenne de 168 nm. L'hypothèse la plus probable est que les échantillons ne sont pas assez représentatifs pour reproduire la distribution de longueur de la solution entière. Uniquement une petite partie (3-4 gouttes) de la

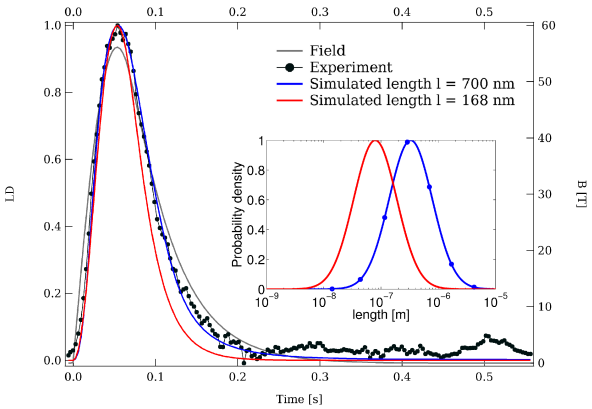

(a) $\eta = 0.001$

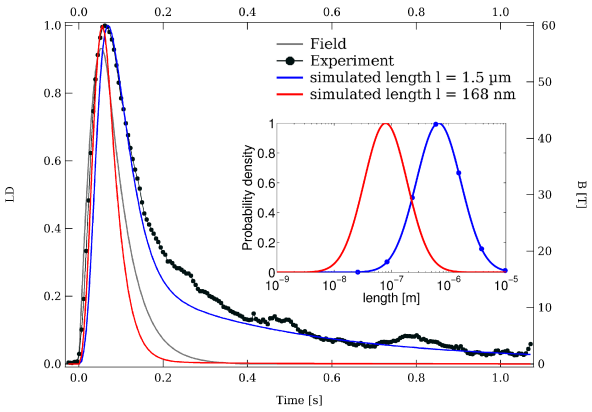

(b) $\eta = 0.01342$

Figure B.3 *– Résultats expérimentaux comparés aux simulations pour les échantillons caractérisés. (a) Échantillons à faible viscosité (b) et viscosité élevée. L'insert compare la répartition de longueur des nanotubes dans la solution obtenue par mesure rhéologique et la répartition qui reproduit les données expérimentales.*

solution préparée est utilisée pour l'expèrience. Lors des mesures AFM pour déterminer la distribution des longueurs, qui généralement montre des barres d'erreurs très grandes, guère plus de tubes ne sont utilisés.

Néanmoins, ces données restent difficiles à interpréter et une constante fondamentale est inaccessible avec ces échantillons: la constante de rotation diffusionelle. Nous démarrons donc de nouvelles mesures avec des échantillons contenants une seule longueur de tube.

Le comportement mesuré est étonnamment différent des mesures précédentes comme on peut le voir dans la figure B.4. L'alignement persiste encore quelques secondes après l'impulsion magnétique. De plus, les modèles théoriques se trouvent dans l'incapacité de reproduire même approximativement la dynamique observée.

Une première étape pour résoudre le paradoxe est de vérifier l'approximation du régime dilué qui est l'approximation utilisée pour la description faite auparavant.

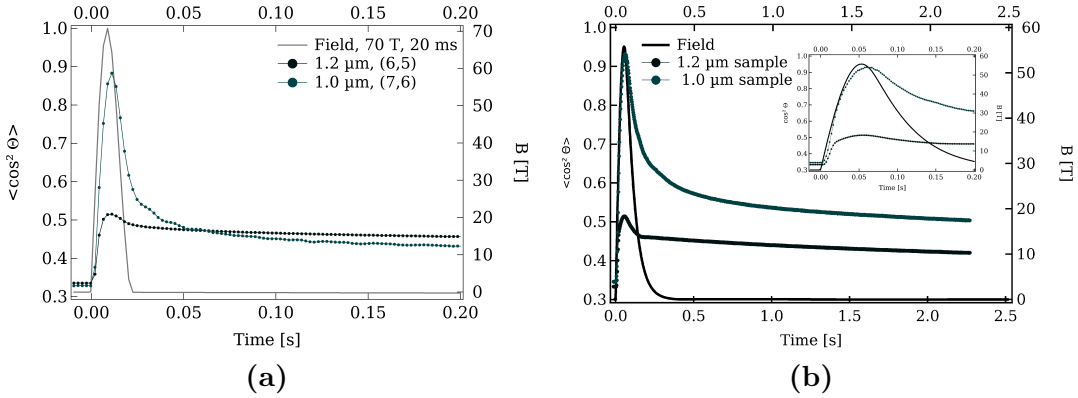

Figure B.4 *– L'angle effectif des nanotubes dans une impulsion de champ (a) 20 ms et (b) 350 ms pour les deux échantillons étudiés. Les modèles de rotation diffusionelle échoue complètement pour la description de ces courbes expérimentales. Les insertions montrent une vue agrandie autour du maximum.*

La concentration mesurée est en effet trop élevée pour que le régime dilué soit encore valide. Nous sommes donc au moins dans le régime semi-dilué. Les tubes peuvent se déplacer librement mais se gênent mutuellement.
Ces nouveaux échantillons ont l'avantage cette fois de rendre accessible la constante de diffusion rotationelle. Lorsqu'on ajuste le désalignement des nanotubes à la fin de l'impulsion magnétique avec une décroissance exponentielle on obtient la valeur de cette constante.
Nous pouvons donc tenter deux approches. La première consiste à récupérer la valeur du fit et de l'insérer dans le modèle théorique développé à cet effet. La deuxième méthode, plus laborieuse, consiste à reformuler le problème dans le régime semi-dilué.
Finalement quelque soit la méthode utilisée aucune n'apporte un résultat satisfaisant au problème comme on peut le constater dans la figure B.5b. Les courbes théoriques du modèle semi-dilué ne reproduisent pas les courbes expérimentales. De plus lorsqu'on compare la constante de diffusion attendue et les résultats du fit, il y a un facteur dix entre les deux valeurs.
D'autre part en examinant le désalignement après l'impulsion de plus près on se rend compte que le processus n'est pas parfaitement exponentiel. Ce qui suggèrerait que nous ne prenons pas tous les effets en compte et qu'il y aurait plus qu' un simple mouvement brownien. Les données expérimentales sont très bien reproduites par un déclin double exponentiel qui fournit un coefficient de diffusion rapdide ($1.29\ s^{-1}$) et un coefficient lent ($0.08\ s^{-1}$). Le rapport entre les paramètres de fit est illustré dans la figure B.5a. Ceci explique également que la description dans le régime semi-dilué ne décrit toujours pas le processus expérimental correctement. De plus lorsqu'on examine l'alignement dans la montée de l'impulsion, dans la figure B.5a, on remarque un changement abrupt de la pente. Cela rappelle fortement le comportement d'une susceptibilité lors d'une transition de phase. Il existe deux théorie pour ex-

pliquer ce comportement. La première est la diffusion dans deux environnements (DITE). Proportionellement au volume libre disponible une première contribution à relaxation rapide permet au molécule de diffuser librement. La contribution avec une relaxation lente est due à des phénomènes coopératifs. La deuxième théorie est la rotation diffusionelle restreinte (RRD). Les molécules forment des cônes où une molécule peut diffuser librement dans les limites de son cône qui l'entoure. La relaxation lente est également due à des phénomènes coopératifs. La figure B.5b montre bien qu'avec concentration diminuante les phénomènes coopératifs deviennent moins important (paramètres A_i) ainsi que le rapport des coefficients de diffusion croît. Ceci reste consistent avec les théories développées plus tôt. Plus la est concentration basse nous nous attendons a retrouvé le comportement d'un système dilué.

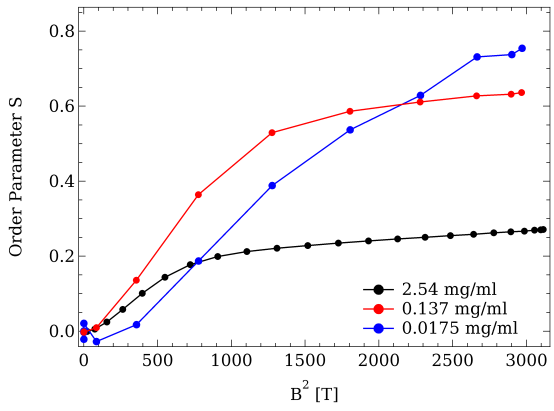

(a)

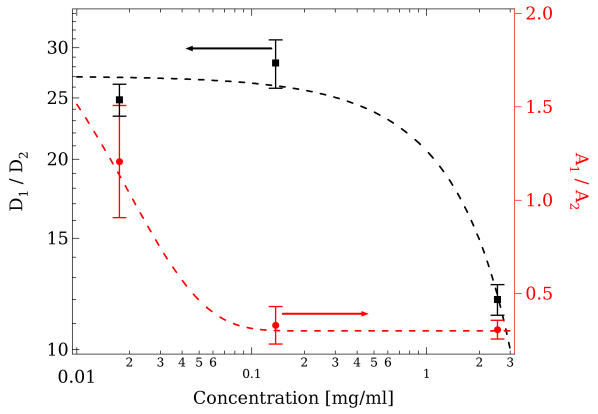

(b)

Figure B.5 *– (a) Courbe expérimentale en fonction du champ magnétique à différente concentration. On constate une saturation de l'alignement en fonction du champ et de la concentration. L'insert démontre qu'il y a deux dynamiques à prendre en compte. (b) On constate que le désalignement après l'impulsion magnétique ne décroît pas de façon parfaitement exponentielle. Le rapport des paramètres de fit d'une double exponentiel sont en bon accord avec les modèles probables pour expliquer le phénomène.*

B.3 Spectroscopie du graphène

Nous changeons de matériau et nous nous interessons à l'absorption du graphène dans le domaine spectral de l'infrarouge proche sous champ intense. Le champ magnétique va imposer la quantification de Landau des porteurs de charge. Nous observons la transition entre ces niveaux. Le graphène est une monocouche de carbone. Cependant il a été montré qu'en fabriquant du graphite par epitaxie sur un crystal de SiC, cette forme multicouche avait les mêmes propriétés que le graphène.
Dû à la nature relativiste des électrons dans le graphène nous ne retrouvons pas la loi ordinaire pour un gaz électronique bi-dimensionels

$$E = \hbar\omega_c \left(n + \frac{1}{2}\right) \tag{B.5}$$

mais une relation en racine du champ magnétique

$$E = v_F \sqrt{\hbar e B n} \tag{B.6}$$

où n est le niveau de Landau. Une constante importante dans la description du graphène est la vitesse de Fermi, v_F, qui est l'équivalent de la vitesse de la lumière pour les photons.
Dans la figure B.6 sont représentées les transitions permises entre niveaux de Landau en fonction de la racine carrée du champ magnétique (lignes pointillées). Par dessus nous avons ajouté les transitions observées expérimentalement dans les champs très intenses (triangles). De plus le tableau est complété par les transitions observées lors de deux travaux antérieurs de Sadowski *et al.* et Plochocka *et al.* (cercles et étoiles respectivement).
On s'aperçoit que les transitions sont bien linéaires avec la racine du champ magnétique ce qui veut dire que nous avons effectivement à faire à des particules relativistes et bien du graphène. À fort champ et haute énergie nous observons néanmoins une légère deviation de la courbe théorique. Cette déviation peut-être expliquée lorsqu'on prend en compte des interactions d'ordre plus élevé comme l'interaction au plus proche voisin. À cette interaction sont associés deux phénomènes:

- Déformation trigonale et
- asymmétrie électron-trou

Cette dernière est plus faible mais peut être detectée à l'aide de la lumière polarisée et nous reviendrons plus tard sur le phénomène. La déformation trigonale est par contre présente. Notamment lorsqu'on calcule la déviation attendue avec la déviation des points expérimentaux on obtient un très bon accord entre le modèle et l'expérience (cf. figure 5.3).

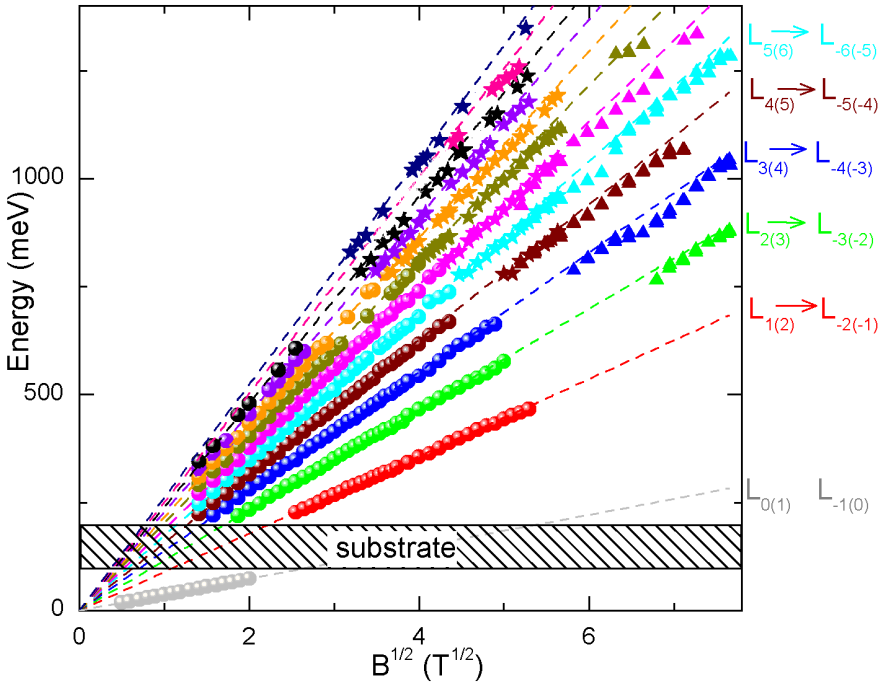

Figure B.6 *– Transitions entre niveaux de Landau prédient par la théorie et observées pendant l'expérience (lignes pointillées et triangles). Pour compléter la figure sont ajoutées les observations expérimentales de [Plochocka 2008] (étoiles) et [Sadowski 2007] (cercles).*

Afin de détecter l'asymmétrie électron-trou nous avons répété l'expérience en nous servant de lumière polarisée circulairement. Des spectres à différents champs magnétiques sont représentés dans la figure B.7. Effectivement nous pouvons clairement detecter une différence entre deux spectres de polarisation opposée. Par contre ce qui est moins attendu est l'apparition, parfois même très faible, de transitions supplémentaires entre les energies prévues par la théorie des particules relativistes et sans masse.
Notons aussi qu'à 60 Tesla, notre champ maximum, l'asymmétrie électron trou est prédite pour être de l'ordre de 5 meV. Cette valeur est très proche de la résolution du spectromètre, donc l'effet recherché est très dur à identifier.
De plus lorsque nous traçons les énergies de transitions observées en fonction du champ magnétique on s'aperçoit que les lignes supplémentaires qui apparaîssent pourraient provenir du graphène bicouche. C'est pourquoi nous pensons plutôt observer les influences du graphène bi-layer, ce qui expliquerait notamment les dépendances en polarisation, et qui masquerait l'asymmétrie électron-trou.
Pour complètement comprendre les spectres et les phénomènes présent observés il est nécessaire de savoir que le graphène produit une rotation Faraday très grande, modifiant ainsi les coefficients de transmission et de réflection. Cela induit une perturbation supplémentaire, mais reste en accord avec l'interprétation de nos spectres.

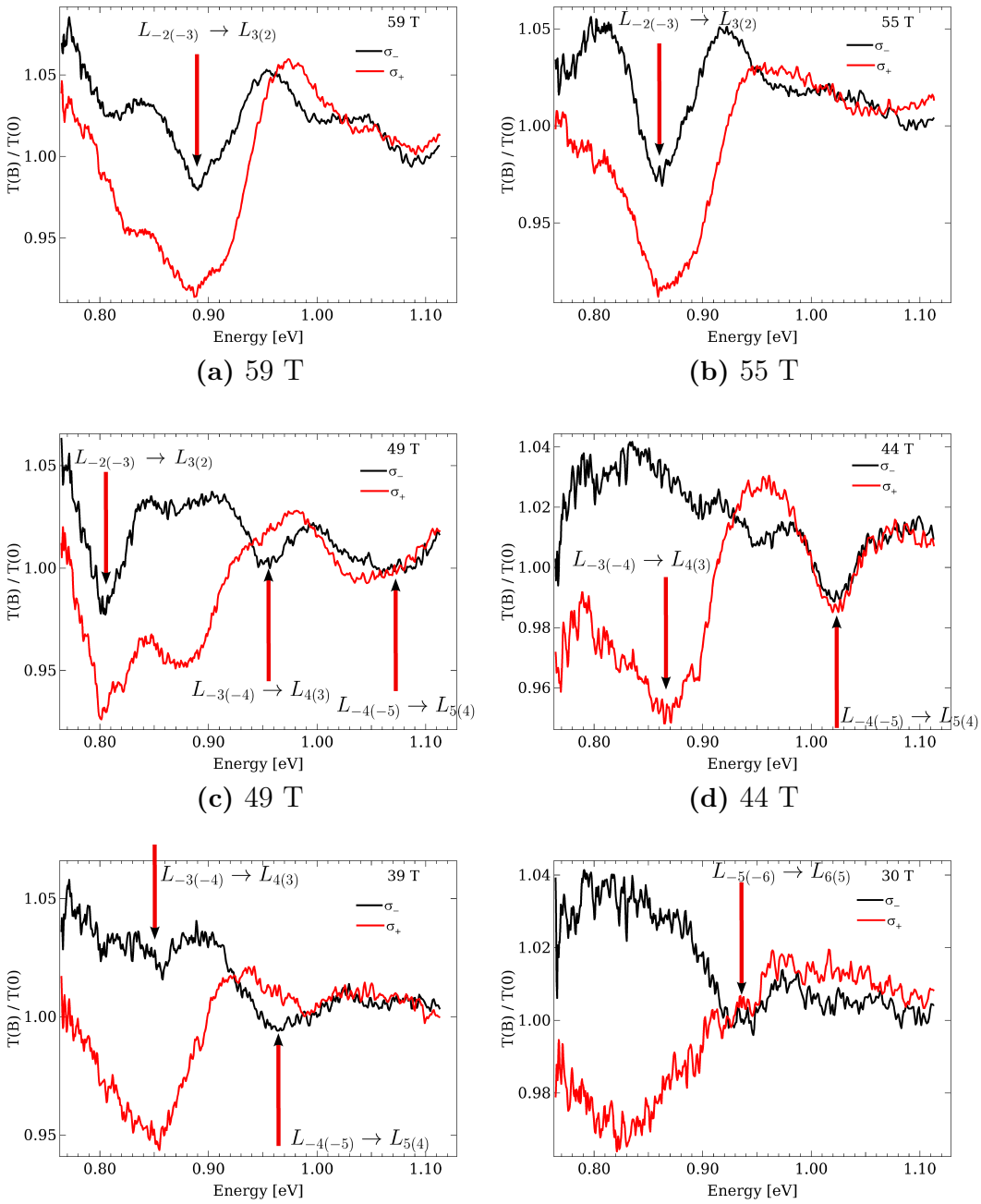

(a) 59 T **(b)** 55 T

(c) 49 T **(d)** 44 T

(e) 39 T **(f)** 30 T

Figure B.7 *– Spectre enregistré avec polarisation opposée à différente valeur du champ magnétique.*

B.4 Spectroscopie du graphite

Nous finissons ce manuscrit avec la spectroscopie du graphite à haute énergie et sous champ magnétique intense. Un cristal de graphite a été exfolié mécaniquement afin d'obtenir une couche très mince pour que la lumière passe à travers l'échantillon; le graphite étant un matériau opaque même pour les ondes infrarouges proches.
Comme dans les parties précédentes nous mesurons la transmission de lumière à travers l'échantillon pendant limpulsion de champ magnétique. Pour une meilleure visualisation des effets observés nous normalisons chaque spectre par le spectre de transmission en absence de champ magnétique.
La figure B.8 nous montre des spectres typiques à 58 T (figure B.8a) et 34 T (B.8b) obtenus dans un aimant pulsé du LNCMI à Toulouse et dans un aimant statique du LNCMI à Grenoble. Pour affiner les mesures nous avons varié la température de l'échantillon de 4.2 K jusqu'à la température ambiante, c'est-à-dire 295 K.
Nous distinguons différents pics d'absorption correspondant aux transitions entre les niveaux de Landau. Dans le graphite nous obtenons un spectre beaucoup plus riche dû à une structure de bande plus complexe dont on obtient un plus grand nombre de transitions dipolaires permises. Néanmoins la majorité des propriétés optiques et électroniques peuvent être expliquées par la structure de bande autour de l'axe **H**-**K**-**H** de la zone de Brillouin du graphite.

Chaque pic d'absorption observé peut enfin être assigné en énergie et champ magnétique et nous obtenons la dépendance en champ des transitions de niveaux de Landau dans la figure B.9. La structure des niveaux de Landau peut évidemment être obtenu en tenant compte du modèle Slonczewski-Weiss-McClure (SWM) avec sept paramètres de liaison forte pour décrire la structure de bande entière du graphite. La structure des niveaux de Landau a par ailleurs été obtenue par *Nakao*. En se basant sur son modèle on peut néanmoins prendre en compte quelques simplifications et on obtient le modèle bi-couche effectif.

La majeure partie de cette simplification est de considérer uniquement deux paramètres du modèle SWM, l'interaction entre proches voisins γ_0 et l'interaction entre couches γ_1. On peut faire ces simplifications car les paramètres importants, comme la déformation trigonale et l'asymétrie électron-trou, s'annulent autour du point **H**.
Les niveaux de Landau obtenus à l'aide de ce modèle simplifié sont tracés dans la figure B.9. Nous apportons la précision ici que les lignes théoriques n'ont pas été réellement ajustées aux points expérimentaux. Nous avons uniquement choisi les valeurs disponibles dans la littérature qui s'approchait au plus de nos données expérimentales. La concordance entre l'expérience et la théorie est remarquable.
En examinant les spectres attentivement, on peut se rendre compte que le pic d'absorption dominant qui correspond à une transition de ligne bleue, c'est-à-dire les transitions que l'on peut également observer dans le graphène. Les pics de cette famille semblent se séparer ce qui n'est pas prévu par les modèles théoriques. On

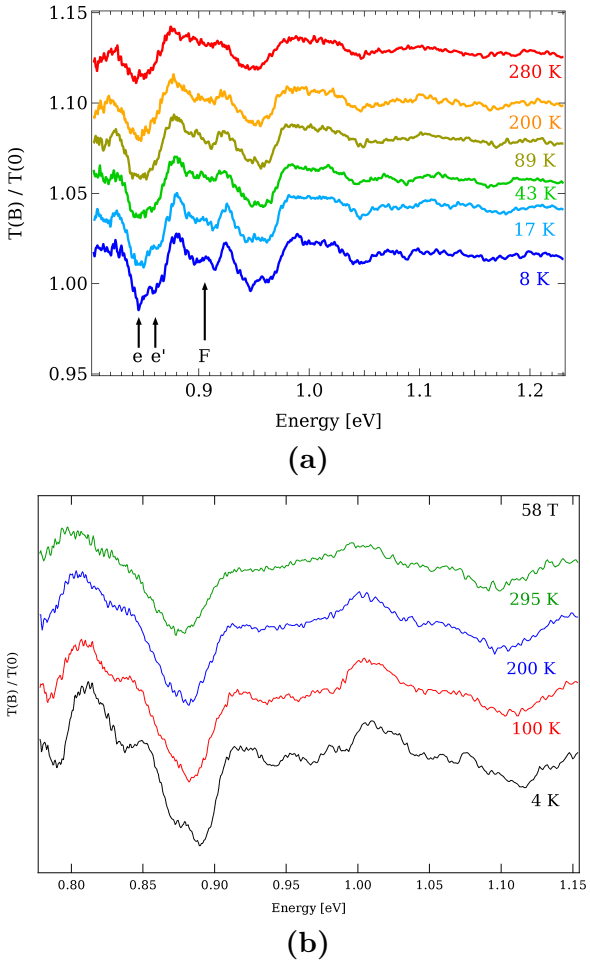

Figure B.8 *– Dépendance en température du graphite dans (a) un champ continu et (b) pulsé. La valeur du champ magnétique est de 34 et 58 Tesla respectivement. Une température de 100 K est suffisante pour supprimer le clivage. Beaucoup de lignes d'absorption sont encore visible même à température ambiante.*

se rend compte que ce clivage disparaît rapidement en augmentant la température. Une température de 100 K est déjà largement suffisante pour faire disparaître le clivage.

Pour tenter d'expliquer cet effet, nous ajustons les pics d'absorption observés à 4.2 K avec une forme Lorentzienne. Ceci est représenté dans la figure B.10a. Notons la légère déviation des deux courbes autour de 0.92 eV qui peut être expliquée par une transition du point **K** qui n'a pas pu être identifiée dans les spectres. Nous gardons les paramètres du fit constant et répétons l'opération pour les températures plus hautes en laissant la largeur du pic libre. Les spectres peuvent être reproduits correctement en tenant compte de l'élargissement dû à l'énergie thermique, excepté pour les transitions du type graphène qui nécessitent que l'on varie l'amplitude pour

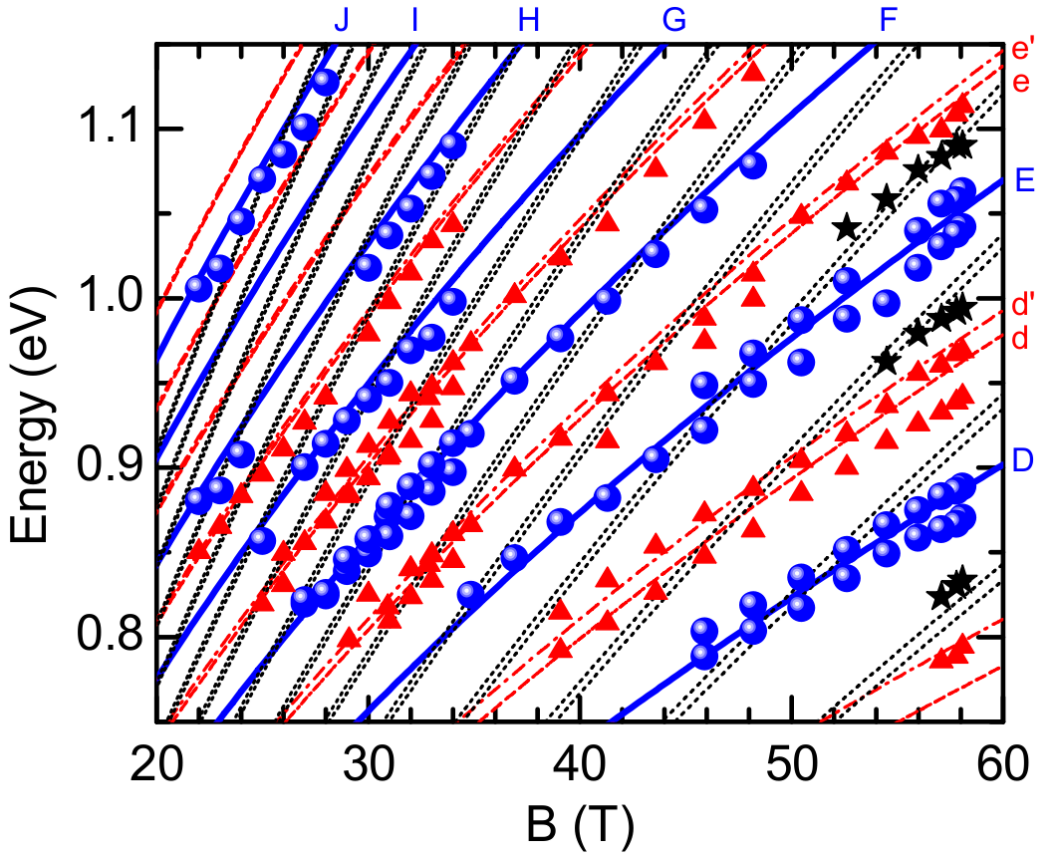

Figure B.9 *– Dépendance en champ des transitions entre les niveaux de Landau. Les points bleus représentent les données expérimentales. Les lignes sont les transitions entre niveaux de Landau théorique d'après le modèle bi-couche effectif. Les lignes bleues représentent les transitions du point* ***H*** *que l'on peut retrouver également dans le graphène. Les lignes rouges sont également des transitions du points* ***H*** *mais entre différentes bandes. Les lignes noires sont les transitions du point* ***K*** *du graphite. L'accord entre théorie et expérience est très bon.*

obtenir un accord convenable entre le calcul et l'expérience. Il n'y a, par contre, aucune justification physique à cela. La dépendance en température ne peut pas être expliquée uniquement par l'élargissement dû à l'énergie thermique.

Une asymétrie électron-trou pourrait expliquer le clivage observé. Pour identifier un tel phénomène nous polarisons la lumière circulairement. Deux spectres de polarisation opposée sont représentés dans la figure B.10b. Nous ne pouvons déceler une dépendance en polarisation pour le pic du type graphène. La résolution en polarisation est très bonne car les prochains pics (d et d') sont nettement dépendants de la polarisation de la lumière. De ce fait, une asymétrie électron-trou ne peut en aucun cas expliquer le clivage observé.

Nous suggérons d'expliquer ce phénomène par un croisement de niveau. En effet lorsqu'on examine soigneusement la dépendance en champ du pic d'absorption

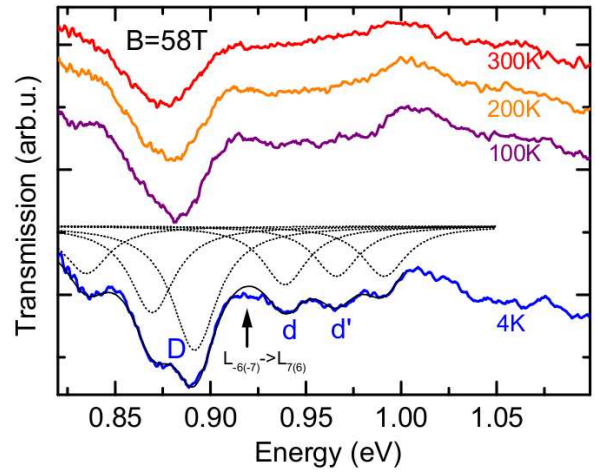

(a)

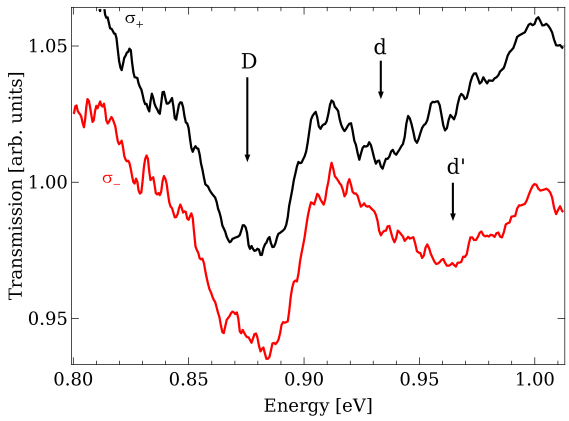

(b)

Figure B.10 *– (a) Spectre dépendant en température utilisé pour le fit. Pour l'exemple le fit à 4 K est montré. La concordance entre les deux courbes est très bonne. La petite déviation autour de 0.92 eV peut être expliquée par la transition du point* ***K*** *qui n'a pas pu être identifée dans le spectre. (b) Spectre de polarisation opposée qui démontre d'une part la bonne qualité de la polarisation qui peut résoudre les pics d et d' et d'autre part que le clivage de la transition D ne peut en aucun cas être attribué à une asymétrie électron-trou.*

D dans la figure B.9 on s'aperçoit que le pic d'énergie plus élevée reproduit la courbe théorique à fort champ. À bas champ, ce sont les points plus faible en énergie qui prennent le relais. Ceci est un bon indicateur d'un croisement de niveau. D'avantage de travaux théoriques et expérimentaux seront nécessaires pour clairement trancher la question.

B.5 Conclusion

Nous avons traité pendant ce travail quatre sujets différents. Dans un premier temps nous avons mis en évidence qu'il faut un champ parallèle à l'axe du nanotube pour observer l'effet Aharonov-Bohm et la luminescence de l'état exciton sombre. Ces expériences sont en bon accord avec des mesures effectuées sur des tubes individuels.

Nous nous sommes en suite interessés à l'alignement des nanotubes dans un champs magnétiques. Nous avons décrit le processus à l'aide d'un modèle basé sur la diffusion rotationelle. Un premier échantillon avec une distribution de longueur de nanotubes connue, ne reproduit pas cette distribution. La seule conclusion que nous pouvons tirer de ces données est que les échantillons mesurés ne sont pas assez représentatifs pour l'ensemble de la solution préparée. Pour approfondir nos études nous avons répété ces mesures avec des nanotubes d'une seule longueur. Dû à la forte concentration de nanotubes dans échantillons, nous obtenons un résultat très différent. Nous avons montré qu'une transition de phase d'un liquide isotrope vers nématique, associé à un déclin coopératif, est une hypothèse plausible pour expliquer cet effet.

Un autre matériau mesuré pendant ce travail est le graphène multicouche sur SiC. Nous avons pu étendre et confimer des études antérieures à des champs allant jusqu'à 60 Tesla et à des énergies de 1.2 eV. La dépendance en polarisation est attribuée à des influences de graphène bicouche présent dans l'échantillon et non à une asymmétrie électron-trou qui reste encore à observer.

Finalement nous fermons la boucle des allotropes de carbone avec l'étude du graphite. Étudié également en transmission nous avons pu décrire les niveaux de Landau dans le graphite à l'aide d'un modèle bicouche montrant que les paramètres plus proche voisin et intercouche sont les plus dominants. De plus nous observons un clivage des transitions de type graphène qui n'est pas prévu par notre modèle. Nous privilégeons ici la piste d'un croisement de niveau empêché mais il reste des travaux théoriques et expérimentaux à effectuer pour comprendre le phénomène.

Bibliography

[Abergel 2007] D. S. L. Abergel and Vladimir I. Fal'ko. *Optical and magneto-optical far-infrared properties of bilayer graphene*. Phys. Rev. B, vol. 75, no. 15, page 155430, Apr 2007. 86

[Ajiki 1993] H. Ajiki and T. Ando. *Magnetic properties of carbon nanotubes*. Journal of Physical Society of Japan, vol. 62, page 2470, 1993. 2

[Ajiki 1994] H. Ajiki and T. Ando. *Aharonov-Bohm effect in carbon nanotubes*. Physica B: Condensed Matter, vol. 201, pages 349 – 352, 1994. 2, 16, 26

[Ajiki 1995] H. Ajiki and T. Ando. *Magnetic Properties of Ensembles of carbon nanotubes*. Journal of Physical Society of Japan, vol. 64, page 4382, 1995. 27, 28

[Ando 1997] Tsuneya Ando. *Excitons in Carbon Nanotubes*. J. Phys. Soc. Jpn., vol. 66, no. 4, pages 1066–1073, 1997. 2, 16, 17

[Ando 2006] T. Ando. *Effects of valley mixing and exchange on excitonsin carbon nanotubes with Aharonov-Bohm flux*. Journal of Physical Society of Japan, vol. 75, page 024707, 2006. 47, 49

[Ando 2008] T. Ando. Topics in applied physics, volume 111. Springer-Verlag Berlin Heidelberg, 2008. 47

[Avouris 2007] P. Avouris, Z. Chen and V. Perebeinos. *Carbon-based electronics*. Nat Nano, vol. 2, no. 10, pages 605–615, October 2007. 1

[Bachilo 2002] S.M. Bachilo, M.S. Strano, C. Kittrell, R.H. Hauge, R.E. Smalley and R.B. Weisman. *Structure-Assigned Optical Spectra of Single-Walled Carbon Nanotubes*. Science, vol. 298, no. 5602, pages 2361–2366, 2002. 16, 44, 45

[Beer 1852] A. Beer. *Bestimmung der Absorption des rothen Lichts in farbigen Flüssigkeiten*. Annalen der Physik und Chemie, vol. 86, pages 78–88, 1852. 70

[Berger 2004] C. Berger, Z. Song, T. Li, X. Li, A.Y. Ogbazghi, R. Feng, Z. Dai, A.N. Marchenkov, E.H. Conrad, P.N. First and W.A. de Heer. *Ultrathin Epitaxial Graphite: 2D Electron Gas Properties and a Route toward Graphene-based Nanoelectronics*. J. Phys. Chem. B, vol. 108, pages 1520–6106, 2004. 77, 78

[Berger 2006] C. Berger, Z. Song, X. Li, X. Wu, N. Brown, C. Naud, D. Mayou, T. Li, J. Hass, A. Marchenkov, E.H. Conrad, P. First and W.A. de Heer. *Electronic Confinement and Coherence in Patterned Epitaxial Graphene*. Science, vol. 312, page 1191, 2006. 78

[Bernal 1924] J. D. Bernal. *The Structure of Graphite*. Proceedings of the Royal Society of London. Series A, vol. 106, no. 740, pages 749–773, 1924. 18

[Bostwick 2007] A. Bostwick, T. Ohta, T. Seyller, K. Horn and E. Rotenberg. *Quasiparticle dynamics in graphene*. Nat Phys, vol. 3, no. 1, pages 36–40, January 2007. 78

[Castro Neto 2009] A. H. Castro Neto, F. Guinea, N. M. R. Peres, K. S. Novoselov and A. K. Geim. *The electronic properties of graphene*. Rev. Mod. Phys., vol. 81, no. 1, pages 109–162, Jan 2009. 7, 9, 20, 22

[Chuang 2009] K.-C. Chuang, A.M.R. Baker and R.J. Nicholas. *Magnetoabsorption study of Landau levels in graphite*. Phys. Rev. B, vol. 80, page 161410(R), 2009. 29, 30, 96

[Cohen 1959] Morrel H. Cohen and David Turnbull. *Molecular Transport in Liquids and Glasses*. The Journal of Chemical Physics, vol. 31, no. 5, pages 1164–1169, 1959. 74

[Crassee 2010] Iris Crassee, Julien Levallois, Andrew L. Walter, Markus Ostler, Aaron Bostwick, Eli Rotenberg, Thomas Seyller, Dirk van der Marel and Alexey B. Kuzmenko. *Giant Faraday rotation in single- and multilayer graphene*. Nat Phys, vol. advance online publication, November 2010. 84, 90

[Deacon 2007] R.S. Deacon, K.-C. Chuang, R.J. Nicholas, K.S. Novoselov and A.K. Geim. *Cyclotron resonance study of the electron and hole velocity in graphene monolayer*. Phys. Rev. B, vol. 76, page 081406(R), 2007. 86, 102

[Doi 1986] M. Doi and S.F. Edwards. The theory of polymer dynamics. Oxford University Press, 1986. 65, 66

[Dresselhaus 1974] G. Dresselhaus. *Graphite Landau Levels in the presence of trigonal Warping*. Phys. Rev. B, vol. 10, no. 8, page 3602, 1974. 28

[Dresselhaus 1994] M.S. Dresselhaus, R.A. Jishi, G. Dresselhaus, K. Inomata, K. Nakao and R. Saito. Molecular Materials, vol. 4, pages 27–40, 1994. 14

[Dresselhaus 2002] M. S. Dresselhaus and G. Dresselhaus. *Intercalation compounds of graphite*. Advances in Physics, vol. 51, pages 1–186, 2002. 20

[Duggal 2006] R. Duggal and M. Pasquali. *Dynamics of individual single-walled carbon nanotubes in water by real-time visualization*. Phys. Rev. Lett., vol. 96, no. 24, page 246104, 2006. 70

[Edwards 2000] B.C. Edwards. *Design and deployment of a space elevator*. Acta Astronautica, vol. 47, no. 10, pages 735 – 744, 2000. 43

[Fagan 2006] J. A. Fagan, B. J. Landi, I. Mandelbaum, J. R. Simpson, V. Bajpai, B. J. Bauer, K. Migler, A. R. Hight Walker, R. Raffaelle and E. K. Hobbie. *Comparative Measures of Single-Wall Carbon Nanotube Dispersion*. The Journal of Physical Chemistry B, vol. 110, no. 47, pages 23801–23805, 2006. 59

[Fagan 2007] J. A. Fagan, J. R. Simpson, B. J. Landi, L. J. Richter, I. Mandelbaum, V. Bajpai, D. L. Ho, R. Raffaelle, A. R. Hight Walker, B. J. Bauer and E. K. Hobbie. *Dielectric Response of Aligned Semiconducting Single-Wall Nanotubes.* Phys. Rev. Lett., vol. 98, no. 14, page 147402, Apr 2007. 50

[Faugeras 2008] C. Faugeras, A. Nerrière, M. Potemski, A. Mahmood, E. Dujardin, C. Berger and W.A. de Heer. *Few-layer graphene on SiC, pyrolitic graphite, and graphene: A Raman scattering study.* Appl. Phys. Lett., vol. 92, page 011914, 2008. 78

[Fraden 1993] Seth Fraden, Georg Maret and D. L. D. Caspar. *Angular correlations and the isotropic-nematic phase transition in suspensions of tobacco mosaic virus.* Phys. Rev. E, vol. 48, no. 4, pages 2816–2837, Oct 1993. 72

[Frings 2008] P. Frings, J. Billette, J. Béard, O. Portugall, F. Lecouturier and G.L.J.A. Rikken. *New Developments at the National Pulsed Field Laboratory in Toulouse.* IEEE T. Appl. Supercon., vol. 18, no. 2, page 592, 2008. 36

[Galt 1956] J. K. Galt, W. A. Yager and H. W. Dail. *Cyclotron Resonance Effects in Graphite.* Phys. Rev., vol. 103, no. 5, pages 1586–1587, Sep 1956. 3, 29

[Geim 2007a] A. K. Geim and K. S. Novoselov. *The rise of graphene.* Nat. Mater., vol. 6, no. 3, pages 183–191, March 2007. 9, 22, 77

[Geim 2007b] Andrey K. Geim and Allan H. MacDonald. *Graphene: Exploring Carbon Flatland.* Physics Today, vol. 60, no. 8, pages 35–41, 2007. 24

[Greenwood 1958] D.A. Greenwood. *The Boltzmann equation in the theory of electrical conduction in metals.* Proc. Phys. Soc., vol. 71, no. 4, page 585, 1958. 86

[Grüneis 2003] A. Grüneis, R. Saito, Ge. G. Samsonidze, T. Kimura, M. A. Pimenta, A. Jorio, A. G. Souza Filho, G. Dresselhaus and M. S. Dresselhaus. *Inhomogeneous optical absorption around the K point in graphite and carbon nanotubes.* Phys. Rev. B, vol. 67, no. 16, page 165402, Apr 2003. 16

[Gusynin 2006] V. P. Gusynin and S. G. Sharapov. *Transport of Dirac quasiparticles in graphene: Hall and optical conductivities.* Phys. Rev. B, vol. 73, no. 24, page 245411, Jun 2006. 86

[Hass 2006] J. Hass, R. Feng, T. Li, X. Li, Z. Zong, W. A. de Heer, P. N. First, E. H. Conrad, C. A. Jeffrey and C. Berger. *Highly ordered graphene for two dimensional electronics.* Appl. Phys. Lett., vol. 89, no. 14, page 143106, 2006. 78

[Helfrich 1970] W. Helfrich. *Effect of Electric Fields on the Temperature of Phase Transitions of Liquid Crystals.* Phys. Rev. Lett., vol. 24, no. 5, pages 201–203, Feb 1970. 72

[Henriksen 2008] E.A. Henriksen, Z. Jiang, L.-C. Tung, M.E Schwartz, M. Takita, P. Wang Y.J.and Kim and H.L. Stormer. Phys. Rev. Lett., vol. 100, page 087403, 2008. 29, 96

[Henriksen 2010] E. A. Henriksen, P. Cadden-Zimansky, Z. Jiang, Z. Q. Li, L.-C. Tung, M. E. Schwartz, M. Takita, Y.-J. Wang, P. Kim and H. L. Stormer. *Interaction-Induced Shift of the Cyclotron Resonance of Graphene Using Infrared Spectroscopy.* Phys. Rev. Lett., vol. 104, no. 6, page 067404, Feb 2010. 24

[Iijima 1991] S. Iijima. *Helical microtubules of graphitic carbon.* Nature, vol. 354, no. 6348, pages 56–58, November 1991. 43

[Jeong 2007] Seok Ho Jeong, Ki Kang Kim, Seok Jin Jeong, Kay Hyeok An, Seung Hee Lee and Young Hee Lee. *Optical absorption spectroscopy for determining carbon nanotube concentration in solution.* Synth. Met., vol. 157, no. 13-15, pages 570 – 574, 2007. 70

[Jiang 2004] J. Jiang, R. Saito, A. Grüneis, G. Dresselhaus and M.S. Dresselhaus. *Optical absorption matrix elements in single-wall carbon nanotubes.* Carbon, vol. 42, no. 15, pages 3169 – 3176, 2004. 16

[Jiang 2007] Z. Jiang, E. A. Henriksen, L. C. Tung, Y.-J. Wang, M. E. Schwartz, M. Y. Han, P. Kim and H. L. Stormer. *Infrared Spectroscopy of Landau Levels of Graphene.* Phys. Rev. Lett., vol. 98, no. 19, page 197403, May 2007. 82, 83, 84, 102

[Kataura 1999] H. Kataura, Y. Kumazawa, Y. Maniwa, I. Umezu, S. Suzuki, Y. Ohtsuka and Y. Achiba. *Optical properties of single-wall carbon nanotubes.* Synth. Met., vol. 103, no. 1-3, pages 2555 – 2558, 1999. International Conference on Science and Technology of Synthetic Metals. 16

[Kohn 1961] Walter Kohn. *Cyclotron Resonance and de Haas-van Alphen Oscillations of an Interacting Electron Gas.* Phys. Rev., vol. 123, no. 4, pages 1242–1244, Aug 1961. 82

[Koshino 2008] M. Koshino and T. Ando. *Magneto-optical properties of multilayer graphene.* Phys. Rev. B, vol. 77, page 115313, 2008. 29

[Koshino 2009] M. Koshino and T. Ando. *Electronic structures and optical absorption of multilayer graphenes.* Solid State Commun., vol. 149, no. 27-28, pages 1123 – 1127, 2009. Recent Progress in Graphene Studies. 28

[Kubo 1957] R. Kubo. *Statistical-mechanical theory of irreversible processes: I. General theory and simple applications to magnetic and conduction problems.* J. Phys. Soc. Japan, vol. 12, no. 6, page 570, 1957. 86

[Leezenberg 1996] Pieter B. Leezenberg, A. H. Marcus, Curtis W. Frank and M. D. Fayer. *Rotational Dynamics of Naphthalene-Labeled Cross-link Junctions in Poly(dimethylsiloxane) Elastomers.* The Journal of Physical Chemistry, vol. 100, no. 18, pages 7646–7655, 1996. 74

[Lefebvre 2006] Jacques Lefebvre, David G. Austing, Jeffery Bond and Paul Finnie. *Photoluminescence Imaging of Suspended Single-Walled Carbon Nanotubes.* Nano Lett., vol. 6, no. 8, pages 1603–1608, 2006. 16

[Lelidis 1993] I. Lelidis and G. Durand. *Electric-field-induced isotropic-nematic phase transition.* Phys. Rev. E, vol. 48, no. 5, pages 3822–3824, Nov 1993. 72

[Li 2006] Z. Q. Li, S.-W. Tsai, W. J. Padilla, S. V. Dordevic, K. S. Burch, Y. J. Wang and D. N. Basov. *Infrared probe of the anomalous magnetotransport of highly oriented pyrolytic graphite in the extreme quantum limit.* Phys. Rev. B, vol. 74, no. 19, page 195404, Nov 2006. 29

[Lu 1995] J. Lu. *Novel magnetic properties of carbon nanotubes.* Phys. Rev. Lett., vol. 74, page 7, 1995. 28

[Maret 1985] G. Maret and K. Dransfeld. *Biomolecules and Polymers in High Steady Magnetic Fields.* In Fritz Herlach, editeur, Strong and Ultrastrong Magnetic Fields and Their Applications, volume 57 of *Topics in Applied Physics*, pages 143–204. Springer Berlin / Heidelberg, 1985. 2

[Matsunaga 2008] Ryusuke Matsunaga, Kazunari Matsuda and Yoshihiko Kanemitsu. *Evidence for Dark Excitons in a Single Carbon Nanotube due to the Aharonov-Bohm Effect.* Phys. Rev. Lett., vol. 101, no. 14, page 147404, Oct 2008. 54, 101

[Maultzsch 2005] J. Maultzsch, R. Pomraenke, S. Reich, E. Chang, D. Prezzi, A. Ruini, E. Molinari, M. S. Strano, C. Thomsen and C. Lienau. *Exciton binding energies in carbon nanotubes from two-photon photoluminescence.* Phys. Rev. B, vol. 72, no. 24, page 241402, Dec 2005. 16, 17

[McCann 2006a] E. McCann and V. Fal'ko. *Landau-Level Degeneracy and Quantum Hall Effect in a Graphite Bilayer.* Phys. Rev. Lett., vol. 96, no. 8, page 086805, Mar 2006. 22

[McCann 2006b] Edward McCann. *Asymmetry gap in the electronic band structure of bilayer graphene.* Phys. Rev. B, vol. 74, no. 16, page 161403, Oct 2006. 24

[McClure 1956] J. W. McClure. *Diamagnetism of Graphite.* Phys. Rev., vol. 104, no. 3, pages 666–671, Nov 1956. 17

[Meeten 1974] G.H. Meeten. Polymer, vol. 15, page 187, 1974. 2

[Mintmire 1998] J. W. Mintmire and C. T. White. *Universal Density of States for Carbon Nanotubes.* Phys. Rev. Lett., vol. 81, no. 12, pages 2506–2509, Sep 1998. 15, 46

[Miura 2008] Noburu Miura. Physics of semiconductors in high magnetic fields. Oxford Science Publications, 2008. 23

[Miyauchi 2006] Y. Miyauchi, M. Oba and S. Maruyama. *Cross-polarized optical absorption of single-walled nanotubes by polarized photoluminescence excitation spectroscopy.* Phys. Rev. B, vol. 74, no. 20, page 205440, Nov 2006. 16

[Monthioux 2006] Marc Monthioux and Vladimir L. Kuznetsov. *Who should be given the credit for the discovery of carbon nanotubes?* Carbon, vol. 44, no. 9, pages 1621 – 1623, 2006. 43

[Mortimer 2007a] I.B. Mortimer, L.-J. Li, R.A. Taylor, G.L.J.A. Rikken, O. Portugall and R.J. Nicholas. *Magneto-optical studies of single-wall carbon nanotubes*. Phys. Rev. B, vol. 76, page 085404, 2007. 50, 52

[Mortimer 2007b] I.B. Mortimer and R.J. Nicholas. *Role of bright and dark excitons in the temperature-dependent photoluminescence of carbon nanotubes*. Phys. Rev. Lett., vol. 98, page 27404, 2007. 52

[Moseley 1978] L.L. Moseley and T. Lukes. *A simplified derivation of the Kubo-Greenwood formula*. Am. J. Phys., vol. 46, no. 6, page 676, 1978. 86

[Motokawa 2004] M. Motokawa. *Physics in high magnetic fields*. Reports on Progress in Physics, vol. 67, no. 11, page 1995, 2004. 1

[Nair 2008] R. R. Nair, P. Blake, A. N. Grigorenko, K. S. Novoselov, T. J. Booth, T. Stauber, N. M. R. Peres and A. K. Geim. *Fine Structure Constant Defines Visual Transparency of Graphene*. Science, vol. 320, no. 5881, page 1308, jun 2008. 2

[Nakao 1976] K. Nakao. *Landau Level Structure and Magnetic Breakthrough in Graphite*. J. Phys. Soc. Jpn., vol. 40, no. 3, pages 761–768, 1976. 20, 28, 99

[Nish 2008] A. Nish, R. J. Nicholas, C. Faugeras, Z. Bao and M. Potemski. *High-field magnetooptical behavior of polymer-embedded single-walled carbon nanotubes*. Phys. Rev. B, vol. 78, no. 24, page 245413, Dec 2008. 54, 101

[Novoselov 2004a] K. S. Novoselov, A.K. Geim, S.V. Morozov, D. Jiang, Y. Zhang, S.V. Dubonos, I.V. Grigorieva and A.A. Firsov. *Electric Field Effect in Atomically Thin Carbon Films*. Science, vol. 306, no. 5696, pages 666–669, October 2004. 1

[Novoselov 2004b] K.S. Novoselov, A.K. Geim, S.V. Morozov, D. Jiang, Katselon M.I., I.V. Grigorieva, S.V. Dubonos and A.A. Firsov. Science, vol. 306, page 666, 2004. 77

[O'Connell 2002] M.J. O'Connell, S.M. Bachilo, C.B. Huffman, V.C. Moore, M.S. Strano, E.H. Haroz, K.L. Rialon, P.J. Boul, W. Noon, C. Kittrell, J. Ma, R. Hauge, B. Weisman and R.E. Smalley. *Band Gap Fluorescence from Individual Single-Walled Carbon Nanotubes*. Science, vol. 297, no. 5581, pages 593–596, July 2002. 2, 45

[Onsager 1949] L. Onsager. *The effects of shape on the interaction of colloidal particles*. Annals of the New York Academy of Sciences, vol. 51, no. 4, pages 627–659, 1949. 72

[Orlita 2008a] M. Orlita, C. Faugeras, G. Martinez, D.K. Maude, M.L. Sadowski and M. Potemski. *Dirac Fermions at the H Point of Graphite: Magnetotransmission Studies*. Phys. Rev. Lett., vol. 100, page 136403, 2008. 29

[Orlita 2008b] M. Orlita, C. Faugeras, P. Plochocka, P. Neugebauer, G. Martinez, D.K. Maude, A.L. Barra, M. Sprinkle, C. Berger, W.A. De Heer and M. Potemski. *Approaching the Dirac Point in High-Mobility Multilayer Epitaxial Graphene*. Phys. Rev. Lett., vol. 101, page 267601, 2008. 78, 84, 86, 92

[Orlita 2009a] M. Orlita, C. Faugeras, G. Martinez, D.K. Maude, J.M. Schneider, M. Sprinkle, C. Berger, W.A. De Heer and M. Potemski. *Magneto-transmission of multi-layer epitaxial graphene and bulk graphite: A comparison.* Solid State Commun., vol. 149, pages 1128–1131, 2009. 29

[Orlita 2009b] M. Orlita, C. Faugeras, G. Schneider J.M. nd Martinez, D.K. Maude and M. Potemski. *Graphite from the Viewpoint of Landau Level Spectroscopy: An effective Graphene Bilayer and Monolayer.* Phys. Rev. Lett., vol. 102, page 166401, 2009. 22, 29, 96

[Orlita 2010] M. Orlita and M. Potemski. *Dirac electronic states in graphene systems: optical spectroscopy studies.* Semicond. Sci. Technol., vol. 25, no. 6, page 063001, 2010. 20

[Ostapenko 2008] T. Ostapenko, D. B. Wiant, S. N. Sprunt, A. Jákli and J. T. Gleeson. *Magnetic-Field Induced Isotropic to Nematic Liquid Crystal Phase Transition.* Phys. Rev. Lett., vol. 101, no. 24, page 247801, Dec 2008. 72

[Ouano 1980] A. C. Ouano and R. Pecora. *Rotational Relaxation of Chlorobenzene in Poly(methyl methacrylate). 2. Theoretical Interpretation.* Macromolecules, vol. 13, no. 5, pages 1173–1177, 1980. 74

[Palser 1999] Adam H. R. Palser. *Interlayer interactions in graphite and carbon nanotubes.* Phys. Chem. Chem. Phys., vol. 1, no. 18, pages 4459–4464, 1999. 18

[Parra-Vasquez 2007] A.N.G. Parra-Vasquez, I. Stepanek, V. Davis, V. Moore, E. Haroz, J. Shaver, R. Hauge, R. Smalley and M. Pasquali. *Simple Length Determination of Single-Walled Carbon Nanotubes by Viscosity Measurements in Dilute Suspensions.* Macromolecules, vol. 40, pages 4043–4047, 2007. 59, 66, 69

[Parra-Vasquez 2009] N. Parra-Vasquez. PhD thesis, Rice University, 2009. 66

[Patrick 1970] Lyle Patrick and W. J. Choyke. *Static Dielectric Constant of SiC.* Phys. Rev. B, vol. 2, no. 6, pages 2255–2256, Sep 1970. 84

[Pecora 1985] R. Pecora. *Dynamics of rodlike macromolecules in semidilute solutions.* J. Polym. Sci., vol. 73, page 85, 1985. 71

[Pedersen 2003] T.G. Pedersen. *Variational approach to excitons in carbon nanotubes.* Phys. Rev. B, vol. 67, no. 7, page 073401, Feb 2003. 2

[Perebeinos 2004] V. Perebeinos, J. Tersoff and P. Avouris. Phys. Rev. Lett., vol. 92, page 257402, 2004. 2, 46

[Perebeinos 2005] V. Perebeinos, J. Tersoff and P. Avouris. *Radiative Lifetime of Excitons in Carbon Nanotubes.* Nano Lett., vol. 5, no. 12, pages 2495–2499, 2005. 17, 46, 49

[Plochocka 2008] P. Plochocka, C. Faugeras, M. Orlita, M.L. Sadowski, G. Martinez and M. Potemski. *High-Energy Limit of Massless Dirac Fermions in Multilayer Graphene using Magneto-Optical Transmission Spectroscopy.* Phys. Rev. Lett., vol. 100, page 87401, 2008. 79, 80, 81, 82, 86, 97, 102, 114

[Rodger 1997] A Rodger and B. Norden. Circular dichroism & linear dichroism. Oxford University Press, 1997. 55, 58

[Sadowski 2006] M. L. Sadowski, G. Martinez, M. Potemski, C. Berger and W. A. de Heer. *Landau Level Spectroscopy of Ultrathin Graphite Layers*. Phys. Rev. Lett., vol. 97, no. 26, page 266405, Dec 2006. 25, 78, 86

[Sadowski 2007] M.L. Sadowski, G. Martinez, M. Potemski, C. Berger and W.A. de Heer. *Magnetospectroscopy of epitaxial few-layer graphene*. Solid State Commun., vol. 143, no. 1-2, pages 123 – 125, 2007. Exploring graphene - Recent research advances. 23, 79, 80, 114

[Saito 1998] R. Saito, G. Dresselhaus and M. Dresselhaus. Physical properties of carbon nanotubes. Imperial College Press, 1998. 9, 10

[Shaver 2007a] J. Shaver and J. Kono. *Magnetic field and temperature dependent photoluminescence from carbon nanotube excitons*. Laser & Photonics Reviews, vol. 1, no. 4, pages 260–274, 2007. 46, 47, 48

[Shaver 2007b] J. Shaver, J. Kono, O. Portugall, V Krstic, G.L.J.A. Rikken, Y. Miyauchi, S. Maruyama and Vasili Perebenios. *Magnetic brightening of Carbon Nanotube Photoluminescence through Symmetry Breaking*. Nano Lett., vol. 7, page 1851, 2007. 48, 52

[Shaver 2008a] J. Shaver, S. A. Crooker, J. A. Fagan, E. K. Hobbie, N. Ubrig, O. Portugall, V. Perebeinos, Ph. Avouris and J. Kono. *Magneto-optical spectroscopy of highly aligned carbon nanotubes: Identifying the role of threading magnetic flux*. Phys. Rev. B, vol. 78, no. 8, page 081402, Aug 2008. 48, 50, 54

[Shaver 2008b] Jonah Shaver. *High Field Magneto-optical Spectroscopy of Semiconducting Single-walled Carbon Nanotubes*. PhD thesis, Rice University, 2008. 50, 53, 54, 66

[Shaver 2009] J. Shaver, A.N.G. Parra-Vasquez, S. Hansel, O. Portugall, C. Mielke, M. Von Ortenberg, R. Hauge, M. Pasquali and J. Kono. *Alignment Dynamics of Single-Walled Carbon Nanotubes in Pulsed Ultrahigh Magnetic Fields*. ACS Nano, vol. 3, no. 1, pages 131–138, 2009. 58, 60, 66, 72

[Shears 1973] Michael F Shears and Graham Williams. *Molecular dynamics of the supercooled liquid state. Low frequency dielectric relaxation of benzophenone, cyclohexanone and fenchone in o-terphenyl*. J. Chem. Soc., Faraday Trans. 2, vol. 69, pages 1050–1059, 1973. 74, 102

[Shizuya 2010] K. Shizuya. *Many-body corrections to cyclotron resonance in monolayer and bilayer graphene*. Phys. Rev. B, vol. 81, no. 7, page 075407, Feb 2010. 82, 83

[Sivarajan 2004] R. Sivarajan. http://www.carbonwall.com/. 2004. 103

[Slonczewski 1958] J.C. Slonczewski and P.R. Weiss. *Band Structure of Graphite*. Phys. Rev., vol. 109, no. 2, page 272, 1958. 17

[Smith 1976] D. Y. Smith. *Superconvergence and sum rules for the optical constants: Natural and magneto-optical activity.* Phys. Rev. B, vol. 13, no. 12, pages 5303–5315, Jun 1976. 84

[Soule 1964] D. E. Soule, J. W. McClure and L. B. Smith. *Study of the Shubnikov-de Haas Effect. Determination of the Fermi Surfaces in Graphite.* Phys. Rev., vol. 134, no. 2A, pages A453–A470, Apr 1964. 3

[Spataru 2005] Catalin D. Spataru, Sohrab Ismail-Beigi, Rodrigo B. Capaz and Steven G. Louie. *Theory and Ab Initio Calculation of Radiative Lifetime of Excitons in Semiconducting Carbon Nanotubes.* Phys. Rev. Lett., vol. 95, no. 24, page 247402, Dec 2005. 17, 45, 47

[Sprinkle 2009] M. Sprinkle, D. Siegel, Y. Hu, J. Hicks, A. Tejeda, A. Taleb-Ibrahimi, P. Le Fèvre, F. Bertran, S. Vizzini, H. Enriquez, S. Chiang, P. Soukiassian, C. Berger, W. A. de Heer, A. Lanzara and E. H. Conrad. *First Direct Observation of a Nearly Ideal Graphene Band Structure.* Phys. Rev. Lett., vol. 103, no. 22, page 226803, Nov 2009. 86

[Srivastava 2008] Ajit Srivastava, Han Htoon, Victor I. Klimov and Junichiro Kono. *Direct Observation of Dark Excitons in Individual Carbon Nanotubes: Inhomogeneity in the Exchange Splitting.* Phys. Rev. Lett., vol. 101, no. 8, page 087402, Aug 2008. 54, 101

[Suematsu 1972] H. Suematsu and S-I. Tanuma. *Cyclotron Resonances in Graphite by Using Circularly Polarized Radiation.* J. Phys. Soc. Jpn., vol. 33, no. 6, pages 1619–1628, 1972. 29, 31

[Toy 1977] W. W. Toy, M. S. Dresselhaus and G. Dresselhaus. *Minority carriers in graphite and the H-point magnetoreflection spectra.* Phys. Rev. B, vol. 15, no. 8, pages 4077–4090, Apr 1977. 29

[Ubrig 2010] Nicolas Ubrig, Jonah Shaver, A. Parra-Vasquez, Matteo Pasquali, Junichiro Kono, J. Fagan and Oliver Portugall. *Dynamic Alignment of Single-Walled Carbon Nanotubes inăPulsed Magnetic Fields.* Journal of Low Temperature Physics, vol. 159, pages 262–266, 2010. 10.1007/s10909-009-0112-8. 61

[Varchon 2007] F. Varchon, R. Feng, J. Hass, X. Li, B. Ngoc Nguyen, C. Naud, P. Mallet, J.-Y. Veuillen, C. Berger, E. H. Conrad and L. Magaud. *Electronic Structure of Epitaxial Graphene Layers on SiC: Effect of the Substrate.* Phys. Rev. Lett., vol. 99, no. 12, page 126805, Sep 2007. 78

[Wallace 1947] P. R. Wallace. *The Band Theory of Graphite.* Phys. Rev., vol. 71, no. 9, pages 622–634, May 1947. 1, 6, 9, 18

[Walters 2001] D. A. Walters, M. J. Casavant, X. C. Qin, C. B. Huffman, P. J. Boul, L. M. Ericson, E. H. Haroz, M. J. O'Connell, K. Smith, D. T. Colbert and R. E. Smalley. *In-plane-aligned membranes of carbon nanotubes.* Chem. Phys. Lett., vol. 338, no. 1, pages 14 – 20, 2001. 58

[Wang 2004] Feng Wang, Gordana Dukovic, Louis E. Brus and Tony F. Heinz. *Time-Resolved Fluorescence of Carbon Nanotubes and Its Implication for Radiative Lifetimes*. Phys. Rev. Lett., vol. 92, no. 17, page 177401, Apr 2004. 2, 16

[Wang 2005] F. Wang, G. Dukovic, L.E. Brus and T.F. Heinz. *The Optical Resonances in Carbon Nanotubes Arise from Excitons*. Science, vol. 308, no. 5723, pages 838–841, May 2005. 2, 17

[Wang 2007] Feng Wang, David J. Cho, Brian Kessler, Jack Deslippe, P. James Schuck, Steven G. Louie, Alex Zettl, Tony F. Heinz and Y. Ron Shen. *Observation of Excitons in One-Dimensional Metallic Single-Walled Carbon Nanotubes*. Phys. Rev. Lett., vol. 99, no. 22, page 227401, Nov 2007. 13

[Warchol 1978] Mark P. Warchol and Worth E. Vaughan. *Dielectric relaxation by restricted rotational diffusion*. Advances in Molecular Relaxation and Interaction Processes, vol. 13, no. 4, pages 317 – 330, 1978. 75, 102

[Wilder 1998] Jeroen W. G. Wilder, Liesbeth C. Venema, Andrew G. Rinzler, Richard E. Smalley and Cees Dekker. *Electronic structure of atomically resolved carbon nanotubes*. Nature, vol. 391, no. 6662, pages 59–62, January 1998. 14, 15

[Williamson 1965] S. J. Williamson, S. Foner and M. S. Dresselhaus. *de Haas-van Alphen Effect in Pyrolytic and Single-Crystal Graphite*. Phys. Rev., vol. 140, no. 4A, pages A1429–A1447, Nov 1965. 3

[Yaguchi 2009] Hiroshi Yaguchi and John Singleton. *A high-magnetic-field-induced density-wave state in graphite*. J. Phys.: Condens. Matter, vol. 21, no. 34, page 344207, 2009. 3

[Zaric 2004a] S. Zaric, G.N. Ostojic, J. Kono, J. Shaver, V.C. Moore, M.S. Strano, R.H. Hauge, R.E. Smalley and X. Wei. *Optical Signature of the Aharonov-Bohm Phase in Single-Walled Carbon Nanotubes*. Science, vol. 304, page 1129, 2004. 45

[Zaric 2004b] S. Zaric, O.N. Ostojic, J. Kono, J. Shaver, V. Moore, R. Hauge, R. Smalley and X. Wei. *Estimation of Magnetic Susceptibility Anisotropy of Carbon Nanotubes Using Magnetophotoluminescence*. Nano Lett., vol. 4, no. 11, page 2219, 2004. 16, 28

[Zaric 2006] S. Zaric, G. N. Ostojic, J. Shaver, J. Kono, O. Portugall, P. H. Frings, G. L. J. A. Rikken, M. Furis, S. A. Crooker, X. Wei, V. C. Moore, R. H. Hauge and R. E. Smalley. *Excitons in Carbon Nanotubes with Broken Time-Reversal Symmetry*. Phys. Rev. Lett., vol. 96, no. 1, page 016406, Jan 2006. 48

[Zhang 2006] Y. Zhang, Z. Jiang, J. P. Small, M. S. Purewal, Y.-W. Tan, M. Fazlollahi, J. D. Chudow, J. A. Jaszczak, H. L. Stormer and P. Kim. *Landau-Level Splitting in Graphene in High Magnetic Fields*. Phys. Rev. Lett., vol. 96, no. 13, page 136806, Apr 2006. 24

[Zheng 2003] M. Zheng, A. Jagota, E.D. Semke, B.A. Diner, R.S. Mclean, S.R. Lustig, R.E Richardson and N.G. Tassi. *DNA-assisted dispersion and separation of carbon nanotubes*. Nat. Mater., vol. 2, no. 5, pages 338–342, May 2003. 62

[Zhu 2010] Zengwei Zhu, Huan Yang, Benoit Fauque, Yakov Kopelevich and Kamran Behnia. *Nernst effect and dimensionality in the quantum limit.* Nat Phys, vol. 6, no. 1, pages 26–29, January 2010. 3

Author: Nicolas UBRIG
Title: Optical properties of carbon based materials in high magnetic fields
Supervisors: Geert RIKKEN and Oliver PORTUGALL

Laboratory: Laboratoire National des Champs Magnétiques Intenses (LNCMI), CNRS-UPR 3228, 143 Avenue de Rangueil, 31400 Toulouse

Abstract:

Carbon nanotubes are unique nano-objects with highly anisotropic electrical, magnetic and optical properties. In the past years the physics of carbon nanotubes made important steps toward the comprehension of its various complex physical properties. The optical response of nanotubes is driven by excitons. Of the sixteen possible exciton states only one decays radiatively. However a magnetic field can brighten one of the dark states. The aim of the first part of this thesis investigates the issue of the brightening of dark excitons.
In the second part we use the magnetic properties of single walled carbon nanotubes to investigate their dynamic alignment in a pulsed magnetic field. Semiconducting tubes are diamagnetic both along and perpendicular to their long axis but the magnitude of the perpendicular susceptibility is higher. Metallic tubes are paramagnetic along their long axis and diamagnetic perpendicular to it. This constrains SWNT to align parallel to a magnetic field. Our data will be analysed with the aid of a theoretical model based on rotational diffusion of rigid rods.
In the third part we study the magneto-optical properties of epitaxially grown multi-layer graphene. The Landau levels of graphene are different from standard two dimensional electron gases. They show a $\sqrt{B}$-dependence due to the relativistic nature of their charge carriers. We measure the system at high fields and high energies to probe the limit of massless Dirac fermions.
The discovery of massless relativistic particles in graphene, a mono-layer of graphite, has completely renewed the interest in graphite. As a matter of fact graphite the optical properties of graphite are best described by bi-layer graphene. We show that the magneto-transmission experiments on thin graphite are in very good agreement with an effective bi-layer model. In addition we observe a non-predicted double structure in the graphene-like transitions which is not reported before.

Auteur: Nicolas UBRIG
Titre: Propriétés optiques des matériaux à base de carbone sous champ magnétique intense
Directeurs de thèse: Geert RIKKEN et Oliver PORTUGALL
Spécialité: Physique

Lieu et date de la soutenance: Salle de séminaire du LNCMI, 18 Mars 2011
Laboratoire: Laboratoire National des Champs Magnétiques Intenses (LNCMI), CNRS-UPR 3228, 143 Avenue de Rangueil, 31400 Toulouse

Résumé:

La découverte des nanotubes de carbone, il y a maintenant une vingtaine d'années, a été un des moteurs de la recherche des nanotechnologies. Ces particules illustrent l'amalgame entre le monde macroscopique et le monde appelé *nano*. Cette discipline a également relancée la recherche sur le graphite et le carbone en général, qui atteint un nouveau sommet avec la découverte du graphène, une monocouche de graphite. Rapidement la physique des nanotubes et du graphène ont suscité l'intérêt d'être étudié sous champ magnétique avec la découverte de l'effet Aharonov-Bohm dans les nanotubes ou l'effet hall quantique dans le graphène.
Cette thèse a pour but d'approfondir la connaissance des propriétés optiques des nanotubes, du graphène et du graphite sous champ magnétique intense. Pour cela nous nous interesserons dans un premier temps à la problématique des excitons sombres. Nous étudierons ensuite les propriétés magnétiques et dynamiques des tubes. La famille métallique est paramagnétique le long de son axe et diamagnétique perpendiculaire à celui-ci. La famille semiconductrice est diamagnétique par rapport à ces deux orientations mais la valeur perpendiculaire est plus élevée. De ce fait tous les nanotubes vont s'aligner parallèlement à un champ magnétique appliqué. Nous utiliserons des méthodes de spectroscopie optique pour étudier ce phénomène.
La deuxième partie de la thèse consistera à examiner les propriétés optiques du graphène et du graphite et plus précisément les transitions entre niveaux de Landau sous champs intenses. La particularité du graphène est que ses porteurs de charge se comportent comme des particules relativistes avec une masse nulle. Les niveaux de Landau se trouvent modifiés avec une dépendance en racine du champ magnétique, par rapport aux systèmes deux dimensionels classiques, où l'on retrouve une dépendance linéaire comme pour l'électron libre par exemple. Ceci nous entrainera également à reéxaminer les propriétés du graphite et d'approfondir les connaissances, notamment à champ très élevé, sur ce matériau à priori bien connu et étudié dans le passé.
Mots-clés: Graphène, Nanotubes de carbone, Spectroscopie optique, Champ magnétique intense, Magnetoscience